



Technische Universität Wien
Institut für angewandte Physik - Biophysik

Dissertation

zur Erlangung des Grades
Doctor rerum naturalium (Dr. rer. nat.)

Preparation of substrates for in vivo nanopatterning of membrane proteins for super-resolution microscopy

unter der Leitung von
Univ.Prof. Dipl.-Ing. Dr. Gerhard J. Schütz
Univ.Ass. Dipl.-Ing. Dr. Eva Sevcsik

vorgelegt von
Marco Lindner
Matrikelnummer 01456131
geboren am 24.03.1986
in Pegnitz (Deutschland)

am
9. September 2019



Die approbierte gedruckte Originalversion dieser Dissertation ist an der TU Wien Bibliothek verfügbar.
The approved original version of this doctoral thesis is available in print at TU Wien Bibliothek.

Eidesstattliche Erklärung

Ich erkläre an Eides statt, dass ich die vorliegende Arbeit selbstständig verfasst, andere als die angegebenen Quellen / Hilfsmittel nicht benutzt, und die den benutzten Quellen wörtlich und inhaltlich entnommenen Stellen als solche kenntlich gemacht habe. Das in TISS der TU Wien hochgeladene Textdokument ist mit der vorliegenden Dissertation identisch.

Datum

Unterschrift

Abstract

Membrane proteins are the interface of cell communication and the target of more than 60 % of all medical drugs. However, their quantitative analysis remains challenging, as the highly complex local environment, including other proteins, is critical to their functionality. In 2008, our group presented a method that allows to track the interaction of membrane proteins in space and time. For this purpose, the cells are placed on micropatterned substrates, which fix the membrane proteins *in vivo* on periodic areas. The lateral distribution of a fluorescently labeled target protein is monitored in the living cell by total internal reflection fluorescence microscopy (TIRFM). In case of interaction, the spatial distribution of the target protein will be that of the fixed membrane protein, while otherwise a more even distribution across the available space will be present.

The basis of this method is the substrate, which structures the arrangement of the membrane proteins. For this purpose, a two-dimensional pattern of anchor and block proteins is applied to a TIRFM-suitable substrate. The lateral resolution of the method for interaction detection is primarily defined by the periodicity of this protein pattern. Analysis of spatial heterogeneities in the protein-protein interaction requires the interrogation of contrast values at a spatial frequency which is higher than the desired resolution of the pattern. To improve the lateral resolution down to length-scales of one micrometer, a period of less than 500 nm is necessary due to the Nyquist theorem. In this work a simple method to produce such substrates with protein patterns that can reach a period well below the optical resolution limit of 200 nm is presented. For this purpose, nanocontact printing (nCP) is performed with a silicone that was originally developed in 2009 for a variation of nanoimprint lithography (NIL) and, to our knowledge, has not yet been used for contact printing.

First, masters were produced by phase transition mastering (PTM) and silicone stamps were molded from them. Two types of silicones with high Young's modulus were used and the structural shape, diameter and period were varied to the technical limits of PTM. From this it could be deduced which degree of hardness of the silicone is required for which geometry. An equally important part of nCP is substrate preparation and coating, and several variants have been reviewed. A coating material that has not yet been used for μ CP or nCP has been shown to give the best results. The functionality of the produced protein patterns was checked by TIRFM and super-resolution microscopy. Subsequently, a master was acquired that had a period of 140 nm and nanopatterns were successfully created. At these length scales, the choice of the protein turned out to be crucial for success. These protein patterns were examined with atomic force microscopy (AFM) and stimulated emission depletion (STED) microscopy. With these nanopatterns, it will be possible to decrease the resolution of the protein interaction assay to below 300 nm.

Zusammenfassung

Membranproteine sind die Schnittstelle der Zellkommunikation und das Ziel von mehr als 60 % aller Medikamente. Ihre quantitative Analyse ist jedoch nach wie vor herausfordernd, da die hochkomplexe, lokale Umgebung bestehend unter anderem aus weiteren Proteinen entscheidend für ihre Funktionalität ist. Unsere Gruppe stellte 2008 eine Methode vor, die es erlaubt, die Interaktion von Membranproteinen in Raum und Zeit zu verfolgen. Hierfür werden die Zellen auf mikrostrukturierte Substrate gebracht, die die Membranproteine *in vivo* auf periodische Bereiche fixieren. Die laterale Verteilung von markierten Zielproteinen wird dabei in der lebenden Zelle mittels total internal reflection fluorescence microscopy (TIRFM) verfolgt. Bei Interaktion wird die räumliche Verteilung der Zielproteine der der fixierten Membranproteine entsprechen, während anderenfalls eine eher gleichmäßige Verteilung über den verfügbaren Raum vorliegt.

Die Grundlage dieser Methode stellt das Substrat dar, welches die Anordnung der Membranproteine strukturiert. Hierfür wird ein zweidimensionales Muster von Fang- und Blockproteinen auf einer TIRFM-geeigneten Oberfläche aufgebracht. Die laterale Auflösung der Methode zur Interaktionsdetektion ist dabei vorrangig über die Periodizität dieses Proteinmusters definiert. Die Analyse räumlicher Heterogenitäten in der Protein-Protein-Wechselwirkung erfordert die Abfrage von Kontrastwerten bei einer räumlichen Frequenz, die höher ist als die Auflösung des Proteinmusters. Um die laterale Auflösung in den Größenbereich von einem Mikrometer zu bringen, ist aufgrund des Nyquist-Theorems eine Periode von weniger als 500 nm erforderlich. In dieser Arbeit wird eine einfache Methode vorgestellt, um mittels nanocontact printing (nCP) Substrate mit Proteinmustern herzustellen, die eine Periode deutlich unter der optischen Auflösungsgrenze von 200 nm erreichen können. Hierfür wird nCP mit einem Silikon durchgeführt, welches 2009 ursprünglich für eine Variation von nanoimprint lithography (NIL) entwickelt und noch nicht für nCP verwendet wurde.

Zuerst wurden mit phase transition mastering (PTM) Master hergestellt und davon Silikonstempel abgeformt. Es wurden hierfür zwei Arten von Silikonen mit hohem Elastizitätsmodul verwendet und die Strukturform, -durchmesser und -periode bis an die technischen Grenzen von PTM variiert. Daraus konnte gefolgert werden, welcher Härtegrad des Silikons für welche Geometrie benötigt wird. Ein ebenso wichtiger Bestandteil bei nCP ist die Substratvorbereitung und -beschichtung und auch hier wurden mehrere Varianten überprüft, wobei sich eine Methode, die bislang noch nicht für μ CP oder nCP verwendet wurde, als die Beste erwies. Die Funktionalität der hergestellten Proteinmuster wurde mittels TIRFM und hochauflösender Mikroskopie überprüft. Anschließend wurde ein Master angefertigt, der eine Periode von 140 nm aufwies und damit erfolgreich Protein-Nanomuster erstellt, wobei sich allerdings gezeigt hat, dass in dieser Größenordnung die Wahl des Proteins entscheidend ist. Diese Proteinmuster wurden mit atomic force microscopy (AFM) und Stimulated Emission Depletion (STED) microscopy untersucht. Mit diesen Nanomustern ist es möglich, die Auflösung der Interaktionsdetektion auf unter 300 nm zu verringern.

Contents

| | |
|---|-----------|
| I. Introduction | 1 |
| 1. Motivation | 2 |
| 2. Objective and overview | 4 |
| 3. Abbreviations | 5 |
| 4. Interaction assay based on protein patterns | 6 |
| 5. Lithography | 8 |
| 5.1. Phase Transition Mastering | 8 |
| 5.2. Nanoimprint lithography | 10 |
| 5.3. High-modulus silicone stamps | 13 |
| 6. Protein patterning | 16 |
| 6.1. Proteins and membrane proteins | 16 |
| 6.2. Patterning of proteins | 19 |
| 6.3. Protein adhesion promoter | 20 |
| 7. Microscopy | 23 |
| 7.1. Atomic force microscopy | 23 |
| 7.2. Fluorescence microscopy | 25 |
| 7.3. Direct stochastic reconstruction microscopy | 29 |
| 7.4. Stimulated emission depletion microscopy | 29 |
| II. Nanocontact printing with high-modulus silicones | 33 |
| 8. Introduction | 34 |
| 9. Materials and Methods | 36 |
| 10. Nanocontact printing with PTM-fabricated masters | 40 |
| 10.1. Phase-transition mastering of multi-pattern masters | 40 |
| 10.2. Development of composite stamps of high-modulus silicones | 42 |
| 10.3. Characterization of nCP prints of proteins by AFM | 47 |

| | |
|---|------------|
| 10.4. Substrate preparation and comparing options for coating | 48 |
| 10.5. Geometrical limits of stamps with three different Young's moduli | 51 |
| 10.6. Influence of protein concentration for nCP | 55 |
| 10.7. Washing, reusability and large area prints | 58 |
| 10.8. Incubation of SAV on FNT pattern | 59 |
| 10.9. Qualitative assessment with TIRFM and super-resolution microscopy | 60 |
| 10.10 Discussion | 64 |
| 11. Nanocontact printing with a period of 140 nm | 66 |
| 11.1. Master design and preparation of composite stamps | 66 |
| 11.2. Nanocontact printing of FNT with 80 nm wide wells | 68 |
| 11.3. Nanocontact printing of BSA with 80 nm wide wells | 69 |
| 11.4. Shelf-life of nanopatterned BSA | 72 |
| 11.5. Imaging of antibody nanopatterns with STED | 72 |
| 11.6. Discussion | 73 |
| 12. Conclusion | 75 |
| III. Alternative approaches to nanopatterning of proteins | 79 |
| 13. Nanocontact printing with hard POSS stamps | 80 |
| 13.1. Introduction | 80 |
| 13.2. Materials and Methods | 80 |
| 13.3. Experiments | 82 |
| 13.4. Discussion | 82 |
| 14. Nanopatterning of proteins with a water soluble resist | 84 |
| 14.1. Introduction | 84 |
| 14.2. Materials and Methods | 85 |
| 14.3. Nanoimprint lithography of NAM | 88 |
| 14.4. Modifying water solubility of polymerized NAM | 95 |
| 14.5. Discussion | 101 |
| IV. Appendix | 105 |
| List of Figures | 106 |
| Bibliography | 108 |
| Contributions and Publications | 124 |
| Acknowledgment | 125 |



Die approbierte gedruckte Originalversion dieser Dissertation ist an der TU Wien Bibliothek verfügbar.
The approved original version of this doctoral thesis is available in print at TU Wien Bibliothek.

Part I.

Introduction

1. Motivation

Membrane proteins are the interface for the interaction between a cell and its environment [1]. They are therefore of academic value, but also the target of 60 % of all medical drugs [2], which makes them a necessary research target from a medical point of view. However, in order to understand which partners interact at the molecular level, it is necessary to know the protein interaction patterns in space and time.

Most approaches to the analysis of protein interactions rely on cell lysates using techniques such as immunoprecipitation, affinity purification, or chemical crosslinking [3, 4]. However, these screening platforms are rather artificial systems rendering the results problematic to confer on the *in vivo* situation. In live cells, assays are challenging, laborious, suffer from detection of false positives or negatives, do not allow for easy quantification, and/or are not readily accessible for many labs (e.g., bimolecular fluorescence complementation [5], yeast two-hybrid screen [6], Förster resonance energy transfer [7], or single-molecule methods [8]). The quantitative analysis of membrane-protein interactions in living cells is still very challenging because the plasma membrane is both highly complex and highly dynamic [9].

Our group has developed a method that allows to make statistical statements about the interaction of membrane proteins and other interaction partners within a living cell [24]. The basis for this method are substrates with patterned anchor proteins. This method was applied with a pattern of 3 μm disks and 3 μm spaces with total internal reflection fluorescence microscopy (TIRFM). However, in order to resolve micrometer-sized clusters of membrane proteins, structures having a period smaller than half the typical feature size are necessary. The resolution achievable with this method is therefore limited by two major factors: the microscopy technique and the periodicity of the anchor proteins on the substrate. In this work, existing super-resolution microscopy devices were used, the focus was on the simple production of high-quality substrates with patterns of anchor proteins down to a periodicity of less than 200 nm.

A state-of-the-art laboratory technique for creating 2D patterns of proteins is microcontact printing (μCP), which is fast, inexpensive, and simple, requiring neither cleanroom instruments nor absolutely flat surfaces [10]. Poly (dimethylsiloxane) (PDMS) has been the material of choice for μCP since its introduction in the early 1990s [11, 12]. Unfortunately, PDMS is not suitable for nanopatterns. Disadvantages of PDMS such as sagging and pairing are particularly pronounced in the sub-micrometer range, so that the invention of alternative techniques and materials for the nanoscale has become nec-

essary. Alternatives include conventional photolithography to form a base template for protein adsorption, but this is limited by diffraction [13]. Below the diffraction limit, dip-pen lithography [14, 15] and e-beam patterning [16] play a major role, but these are relatively delicate processes. Finally, nanoimprint lithography (NIL) applications are independent of the deflection limit and offer an alternative method for nanostructuring of proteins, even with metal-based reusable templates [17]. However, NIL-based processes are also very complex and often require hazardous resists and expensive systems.

Here, a nanocontact printing approach to fabricate highly condensed 2D-nanopatterns of proteins is presented that has all the advantages of silicone-based printing while avoiding its drawbacks. This is made possible by utilizing the novel stamp material X-PDMS in a 2-layer stamp architecture which has been, to our knowledge, so far only been applied for substrate conformal imprint lithography (SCIL) [18, 19]. The Young's modulus of X-PDMS can be adjusted by the curing temperature and time up to 80 MPa which is suitable for SCIL with nanofeatures down to several tens of nanometer. Thus, the stamp combines the advantages of two worlds: allowing features and a periodicity down to the nanometer range and having a long lifetime while still ensuring conformal contact between non-perfect surfaces over large areas and being easy to fabricate. Using X-PDMS for nCP was exemplified by creating a nanostructured antibody surface with feature sizes of 80 nm and a periodicity of 140 nm.

2. Objective and overview

The main goal of this work was the development of a technique for the reproducible production of substrates with nanostructures. The protocol should be suitable for laboratory use. Specifically, it has been defined that the array of disks of anchor molecules surrounded by a suitable blocker should have a period of less than 200 nm. The patterns should be very dense and homogeneous, which means that there are no blocking proteins in the anchoring area and vice versa. In addition, the distance between cell and substrate between the two layers (anchor and blocker) should not vary significantly, as this can lead to misinterpretations, especially in TIRF-based techniques. Finally, strong binding to the glass substrate was also important as the adherent cells would pull on the protein patterns and remove low bound proteins. However, this coating must not increase the autofluorescence compared to glass.

The next chapters of the introduction explain the scientific basics and methods required for the experiments. This includes a summary of the application and the relevant lithography and microscopy techniques.

In the second part of this work the technique is presented, with which the goals of this work could be achieved. The nanostructuring of proteins by nanocontact printing using high modulus silicone stamps is described here. In detail, the influence of the various parameters on the quality of the print is examined. These include the structure size and the Young's modulus of the stamp, various substrate coatings and also the choice of the protein to be printed and its concentration. Experiments are first performed with a period greater than 600 nm before concluding how to achieve a printing with the constraints described above. This was implemented by the production of nanopatterns with 140 nm period. The protein structures were investigated by atomic force microscopy (AFM), their functionality quantified by Total Internal Reflection Fluorescence Microscopy (TIRFM), Stochastic Optical Reconstruction Microscopy (STORM) and Stimulated Emission Depletion (STED) Microscopy.

The third part describes two experimental approaches for the production of surfaces featuring nanostructured proteins. These methods could not fulfill the set conditions for different reasons. Nevertheless, they may be of interest for other applications or through appropriate advancements. The first method describes nanocontact printing by means of hard, functionalized stamps. Second, an attempt to achieve the goal by nanoimprint lithography of a water-soluble resist is described.

3. Abbreviations

| | |
|-----------|---|
| AFM | atomic force microscopy |
| BSA | bovine serum albumin |
| DIW | deionized water |
| FNT | fibronectin |
| FWHM | full width at half maximum |
| μCP / nCP | micro/nanocontact printing |
| NIL | nanoimprint lithography |
| PBS | phosphate-buffered saline |
| PDMS | poly(dimethylsiloxane) |
| PFOCTS | 1H, 1H, 2H, 2H-Perfluorooctyl-trichlorosilane |
| (P)NAM | (polymerized) N-acryloyl morpholine |
| PTM | phase transition mastering |
| RICM | reflection interference contrast microscopy |
| RT | room temperature |
| SAV | streptavidin |
| SCIL | substrate conformal imprint lithography |
| SDS | natriumdodecylsulfat |
| STED | stimulated emission depletion |
| STORM | stochastic optical reconstruction microscopy |
| TIRFM | total internal reflection fluorescence microscopy |

4. Interaction assay based on protein patterns

The interaction between membrane proteins and proteins within the cell can be quantitatively analyzed by a robust, simple and straightforward technique [20, 21, 22, 23]. In short, membrane proteins (baits) of a living cell are limited by an external influence on periodic areas. As a cell attaches to the substrate, the baits diffuse within the membrane until they become attached to the anchor molecules and ideally have the same periodic and well-defined pattern that has been produced and presented on the substrate. The lateral distribution of a fluorescently labeled interaction partners (prey) within the cell is monitored by fluorescence microscopy. When bait-prey interactions occur, the tagged prey molecules represent the pattern of the bait molecules, while a homogeneous distribution of the prey proteins indicate the missing interaction (Figure 4.1A, B). Among other things, this method was used to investigate the interaction of captured CD4 (membrane protein, bait) and LCK (protein involved in intracellular signaling pathways, prey) on a pattern with disks with a minimum size of $3\mu\text{m}$ and interstices of the same size [21, 22, 23] (Figure 4.1C).

The external influence that is intended to fix the membrane proteins is generated by a substrate with anchor proteins (streptavidin proteins and antibodies), these anchors being localized in a periodic and well-defined 2D pattern. The lateral resolution is defined by the protein pattern of the bait, which is achieved by anchor proteins on the prepared substrate. According to the Nyquist theorem, the established microstructuring method with a period of $6\mu\text{m}$ is sufficient for a resolution of $12\mu\text{m}$. To resolve biologically relevant protein clusters such as the immunological synapse of the T cell activation with a length scale of $1\mu\text{m}$, periods of significantly less than 500nm must be used. This, in turn, indicates feature sizes below 250nm that require high-resolution microscopy and fabrication techniques that are not limited by the diffraction barrier.

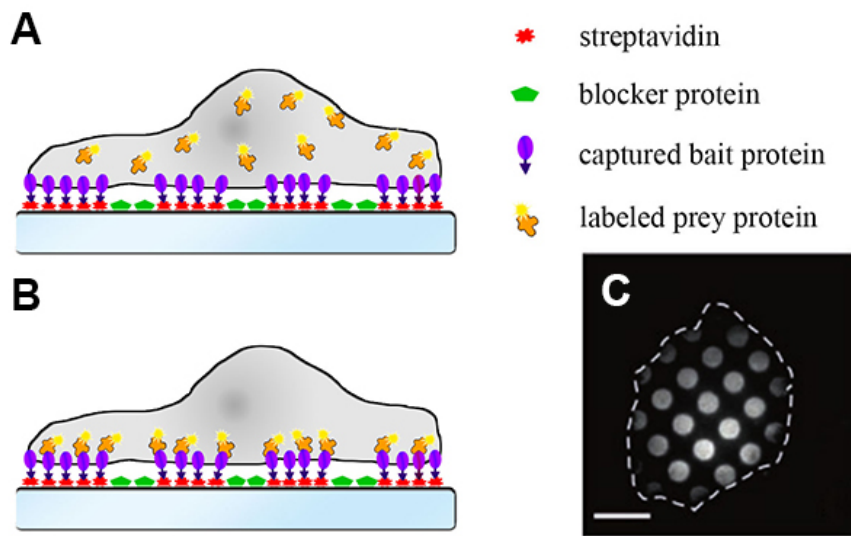


Figure 4.1.: Sketch of the assay to study the interaction of membrane proteins. Chosen membrane proteins (bait) get captured by a protein pattern on a substrate. The target (prey) gets labeled with a fluorescing dye. **(A)** If there is no interaction of bait and prey, the fluorescently labeled prey is distributed homogeneously. **(B)** If interaction between bait and prey appear in vivo, the monitored prey will represent the pattern of the bait. **(C)** TIRFM image of a living cells on a substrate with $3\ \mu\text{m}$ sized disks and $3\ \mu\text{m}$ interspaces. The cell outline is indicated by a dashed white contour line. Scale bar $7\ \mu\text{m}$. Modified from [24]

5. Lithography

5.1. Phase Transition Mastering

The two processes that are the focus of this work are nanoimprint lithography (NIL) and nanocontact printing (nCP). For both, a master is required for the development of stamps. Depending on the conditions attached to a master, different approaches to the preparation of the same are appropriate [25]. In short, for masters having structures several microns wide and non-regular patterns, masked photolithography may be the technique of choice. An example of this would be microfluidics, which can be transferred very well by photolithography. With periodic patterns up to a structure size of several hundred nanometers, the interference lithography allows the creation of small structures on a large area. A flexible technique for structures less than 100 nm wide is electron beam lithography, which on the other hand is expensive and slow. The direct use of biological samples to model bionic structures can be innovative [26]. However, the possible freedom of development is low and one relies on existing and suitable biological samples.

One technique that, to our knowledge, has not yet been applied to nCP mastering is Phase Transition Mastering (PTM). PTM was invented by Sony DADC for the development of templates for the 2003 Blu-ray injection molding process [27, 28]. By 2009, 94% of the Blu-ray masters manufactured by Sony DADC were created with their PTM device PTR-3000 BD Mastering System [29]. One of the strengths of this device is the relatively fast creation of concentric structures that are less than 100 nm deep. Adjustments to the PTM by the Sony DADC BioSciences GmbH made it possible to write patterns that go beyond the concentric Blu-ray Disc patterns, which made the creation of masters for this project possible.

PTM is divided into four steps: sputtering, writing, developing and plating (figure 5.1). The process begins with the sputtering of three layers on an eight-inch silicon wafer. The first layer is an etch stop OPT layer of about 10 nm. The second layer, amorphous silicon, is about 100 nm high. This layer is an essential component of the temperature absorption and can also be used if deeper structures are desired to be generated by deep reactive ion etching (DRIE). The uppermost layer forms an inorganic resist called the phase transition material (PTM layer), typically less than 30 nm. It consists of imperfect oxides of tungsten and molybdenum [30]. A blue laser beam with a Gaussian profile is focused on the uppermost layer of the constantly rotating wafer. Upon laser irradiation ($\lambda = 405$ nm), the phase transition material changes from amorphous to polycrystalline

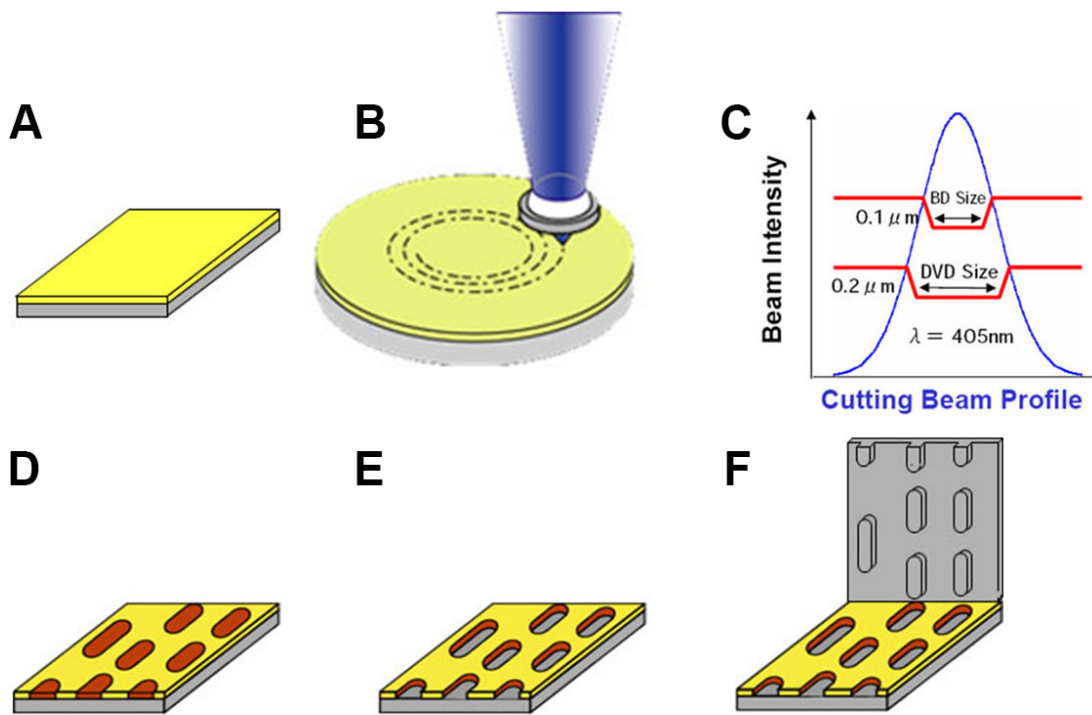


Figure 5.1.: (A) An eight inch silicon wafer gets sputtered with three layers: etch-stop OPT-layer, amorphous silicon, and the inorganic PTM-layer. (B) A laser beam ($\lambda = 405 \text{ nm}$) focuses on the spinning wafer writing the pattern. (C) The inorganic resist requires a certain energy threshold for its heatchemical reaction. The size of these features are much smaller than for DVDs which uses organic resists and a photochemical reaction. (D) The heated parts crystallize and swell and (E) can be dissolved in a development bath exposing the amorphous silicon below the inorganic resist. (F) Plating the PTM-master with nickel results in the final nickel master which will be further processed.

5. Lithography

by thermal absorption. With tetramethylammonium hydroxide (TMAH) wet chemistry, the master can be developed, that is, the crystalline areas are removed to the amorphous Si layer.

Since the phase transition of the PTM layer is a non-linear process and a certain temperature threshold is required to induce the transition, the diameter of the effective spot can be set to a width of about 100 nm which is below the diffraction limit. The excess heat is transferred to the underlying amorphous Si layer. If the PTM layer is significantly higher than 100 nm, either the temperature threshold in the PTM layer can not be uniformly achieved or the heat dissipates too slow, which broadens the width of the written structure.

The PTM wafer released by the PTR-3000 is electrically conductive, allowing nickel to be galvanized directly with a thickness of 0.5 μm . The peeled nickel disk shows the inverse of the written PTM master and serves as the actual master for silicone imprints in this work. Nickel has the great advantage that it forms an inert nickel-oxide layer and silicone can be molded without adhesion problems. It is also possible to produce several nickel masters from one PTM wafer or even to further modify the PTM wafer. The sputtering of a conductive layer onto the PTM wafer before plating reduces the width of wells and widespread pillars, which was used in this work to create 80 nm width silicone pillars.

5.2. Nanoimprint lithography

In 1995, Steven Y. Chou's group introduced a technology for producing nanoscale topological patterns and named them Nanoimprint Lithography (NIL) [31]. In NIL, a stamp with relief structures is pressed into a resist so that the cavities of the stamp are filled with it. The resist gets cured either by temperature or UV-light so that the polymer shows the negative of the stamp.

Chou et al. embossed 25 nm diameter pillars using heat and pressure in PMMA (thermal NIL, T-NIL). Shortly thereafter, Haisma et al. (1996) and Ruchhoeft et al. (1999) presented a method for curing with UV light (UV-NIL) [32, 33]. In this variant, a transparent stamp is pressed at room temperature at a significantly lower pressure in a viscous pre-polymer, which can be cured by UV light before demolding. UV-NIL has the great advantage that both the required pressure and the curing time are greatly reduced. Both T-NIL and UV-NIL have shown replication of 5 – 10 nm structures and imprinted areas up to 200 mm in diameter [34, 25, 35].

Compared to many other lithographic methods, NIL has the advantage that the structure transfer relies on direct contact, so its resolution is not limited to the limitations of light deflection or beam scattering factors.

In addition to these two basic processes, a large number of process variants have been developed on their basis over the last 25 years [36]. One major difference between the variants is the geometry of stamp and substrate: plate-to-plate (P2P), roll-to-plate (R2P) and roll-to-roll (R2R) NIL (fig. 5.3). In P2P, a flat stamp is used to print on a flat substrate which is coated by a suitable resist. This variant is the simplest NIL setup, but technically has some disadvantages. For example, the contact surface in a roll process is theoretically a line, so at P2P a much higher force is needed to get the same pressure (= force per area). In this work we have only used P2P, the term NIL is used synonymous with P2P-NIL.

A fundamental problem of NIL is the difficulty in achieving conformal contact between a rigid stamp and a hard substrate such as glass (fig. 5.2). To address this problem, Whitesides et al. introduced the use of poly(dimethylsiloxanes) (PDMS) for embossing lithography and the term "soft lithography" [12]. PDMS is a polymer with an inorganic siloxane backbone and organic methyl groups [37]. The great advantages of this material are that silicone stamps can easily establish a conformal contact over a large area, they are less susceptible to particle or stamp detachment and can be produced more cost-effectively from a master. In addition, its gas permeability prevents defects caused by trapped bubbles in the resist layer [38]. However, common PDMS as used by Whitesides has a low Young's modulus and is therefore not stable enough for stamps with features in the nanoscale.

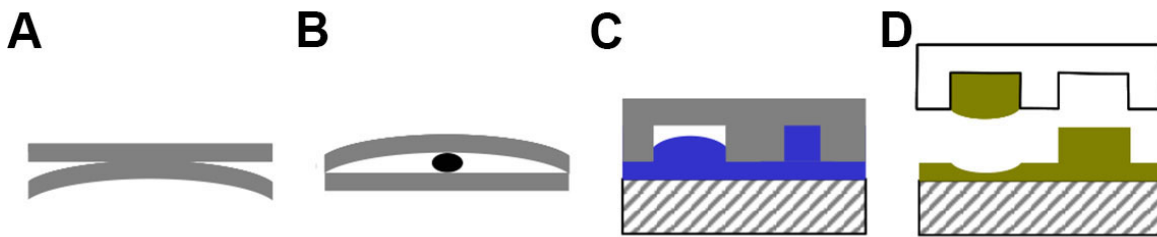


Figure 5.2.: Schematic representation of defects which can occur in NIL or NIL-like processes. **(A)** Partial contact of the stamp with the wafer due to a skew. **(B)** A particle prevents contact between stamp and substrate over an area many times the particle size. **(C)** Incomplete filling of features. **(D)** Breaking of an imprinted resist feature which remains attached to the stamp. Modified from [38]

5. Lithography

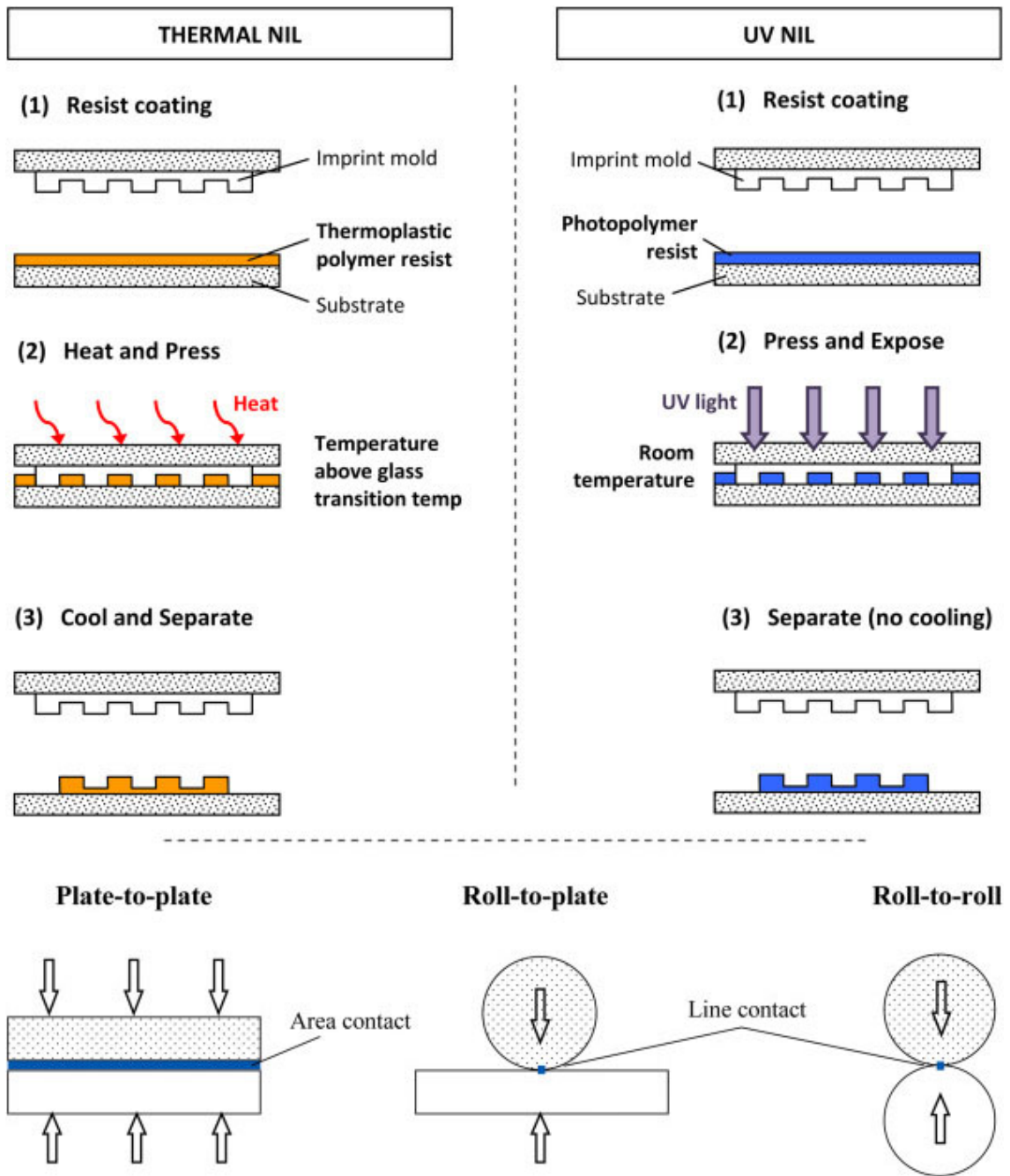


Figure 5.3.: Comparing NIL principles. **(top)** Differences in the way of curing the monomer solution. **(bottom)** Differences in geometry of stamp and substrate. Modified from [36]

5.3. High-modulus silicone stamps

Poly(dimethylsiloxane) PDMS is a polymer of linear linked dimethylsiloxane molecules. If the prepolymer and curing agent are purchased commercially, the PDMS production is very simple: Thorough mixing of the two components, degassing and pouring of the master. The polymerization already starts with the mixing of the components and can be accelerated by raising the temperature. The hardness of the material resulting from the polymerization can be described by the Young's modulus. It is a material constant which represents the ratio of stress and strain of a solid body with linear-elastic behavior:

$$E = \frac{\sigma}{\epsilon} = \text{constant} \quad (5.1)$$

with the mechanical stress σ and the strain ϵ which is defined as the change in length divided by original length.

At near-zero stress, most materials have a linear region and the deformation is reversible. With a higher modulus, more stress is needed to effect the same change in length. The Young's modulus for PDMS varies with the cure time and temperature between $E_S = 1.3 - 3.0$ MPa (commercial Sylgard 184 PDMS) [39, 38]. It is therefore typically smaller than natural rubber $E < 50$ MPa [40] and much smaller than for example Polypropylen $E = 1.3 - 1.8$ GPa [41], glass $E = 40 - 90$ GPa [40] or graphene $E = 1000$ GPa [40] (all at 20 °C).

Its great popularity in the academic field is due to PDMS's additional attractive features [37, 38, 42, 43, 39]:

- (relatively) inexpensive
- easy to fabricate
- conformal contact
- chemical inert
- transparent near-UV and visible light
- temperature stable up to 200 °C
- low interfacial free energy (21.6 dyn/cm)
- gas permeable
- water impermeable

Soft PDMS stamps are well established for both μ CP and NIL. Due to the low modulus of elasticity, a PDMS stamp can easily form a conformal contact over a large area, is less sensitive to particle or stamp releases, and several stamps can be inexpensively produced by a master [38]. In addition, its permeability prevents problems caused by entrapped air bubbles in the resist layer when printed at ambient pressure.

Of course, there are disadvantages associated with the benefits. The soft material is

5. Lithography

susceptible to three major deformations: sagging, deformation and pairing. Sagging describes the collapse of cavities, deformation occurs on contact under pressure. When individual features stick together, it is called pairing. These instabilities are mainly dependent on the low Young's modulus and the low surface energy and have been studied extensively, as they often represent the limiting factor for the spatial resolution of soft lithography approaches. For example, if the elastic energy stored in deformed features is less than the energy gained from the reduction in surface energy at the interface between two features, the patterns are permanently paired [38].

High-modulus silicone derivatives Although a low Young's modulus is required to make conformal contact over larger areas, increasing the modulus would improve the mechanical stability of the silicone. To increase the elastic modulus of PDMS, a modified PDMS type called H-PDMS was developed. The H-PDMS rubber has a Young's modulus $E_H = 8 - 12$ MPa, which is approximately four times the modulus of soft PDMS. However, calculations have shown that this Young's modulus is still insufficient to obtain stable patterns below 100 nm [38]. Therefore, a new silicone derivative called X-PDMS was developed and patented specifically for substrate conformal imprint lithography (SCIL), a variant of P2P-NIL [18].

X-PDMS is a modified PDMS with 20- to 40-fold increased elastic modulus. While normal PDMS and H-PDMS are two-component systems of linear dimethylsiloxane molecules, branched systems (Q-siloxanes) were introduced for X-PDMS (fig. 5.4). By adding branched precursors to a linear PDMS network, multi-directional links were created to form a 3D network. The chain length of the prepolymers and the amount of reactive groups in each precursor were adjusted to maximize the crosslink density. A Young's modulus of $E_X = 80$ MPa could be achieved in this way [38]. Due to the stronger cross-linking, the material also loses some of its advantages, among others it gets very brittle. It is therefore not used as a pure stamp material, but as the top layer of a composite stamp.

The SCIL stamps consist of an layer of X-PDMS (300 μm), a flexible layer of PDMS (0.5 – 2 mm) and thin intermediate layer for adhesion of the both silicones. A glass can be added on top of the soft PDMS to support stabilization. This stack ensures that the stamp best combines the advantages of low-modulus silicones and high-modulus silicones. The soft backplane allows conformal contact across the entire stamp surface, while the stiffer X-PDMS layer minimizes stamp deformation and printing distortion.

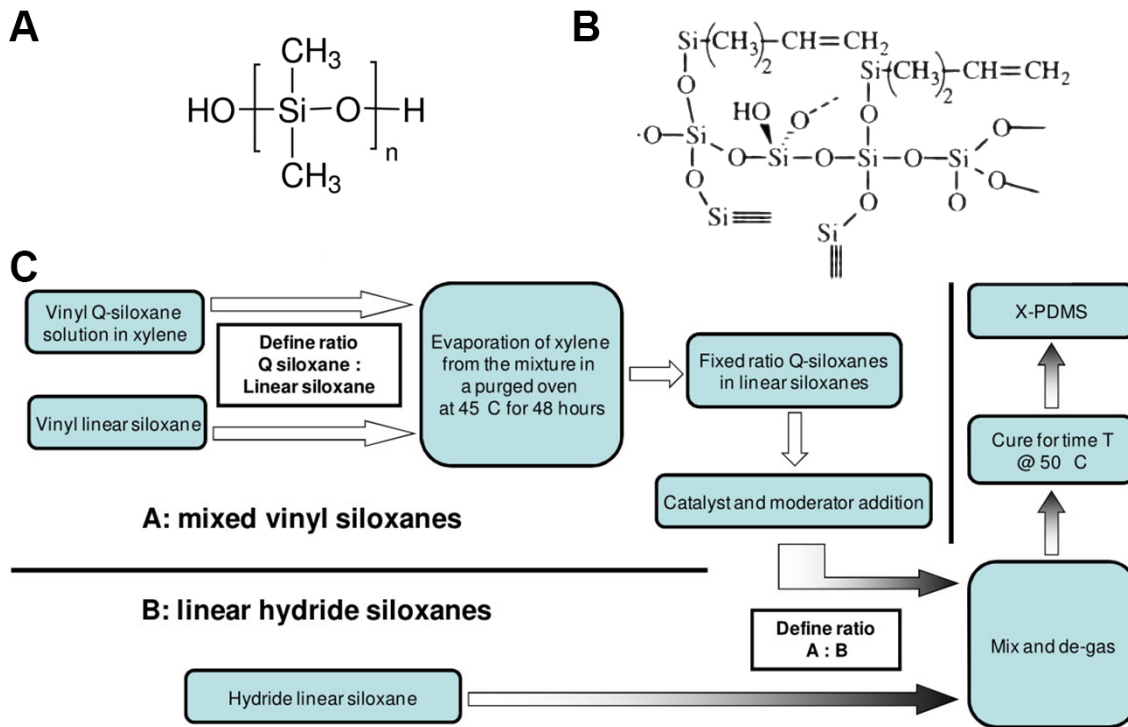


Figure 5.4.: Chemical representation of **(A)** the linear polymer Poly(dimethylsiloxane) (PDMS) and **(B)** the Q-branched siloxane precursor. **(C)** The latter plays an important part of the synthesis of X-PDMS and increases the Young's modulus by 3D-crosslinks. Modified from [18, 38]

6. Protein patterning

6.1. Proteins and membrane proteins

Proteins in general Proteins are linear polymers consisting of amino acids linked by a special type of covalent bond. In eukaryotes, only 20 amino acids are known to be part of proteins, while at least 300 amino acids are found in cells and also have important functions [44]. However, the complexity and functionality of proteins is rarely defined by their sequence (primary structure) but by the folding of the biopolymer. Particularly stable arrangements which form recurrent structural patterns are referred to as secondary structures. The tertiary structure describes a three-dimensional folded polypeptide. If at least two polypeptides form a unit, this is called the quaternary structure [44]. For example, the streptavidin monomer consists of 159 amino acids and in its folded form has a high affinity for vitamin biotin. In its original form it is a homotetramer, the quaternary structure consists of four identical units.

There are several ways to describe proteins. In this work, this pathway was chosen because it will be important that the proteins change their size upon adsorption and that this is related to their polymer structure. But first the term "size" has to be defined and for this the Stokes radius R is often used. This is the radius of a hypothetical solid sphere that has the same diffusion coefficient in solution as the object itself. Thus, the Stokes radius is not the pure extension of the molecule, but often includes entrained molecules of the solution.

$$R = \frac{k_b T}{6\pi\eta D} \quad (6.1)$$

with the Boltzmann constant k_B , the temperature T , the viscosity of the medium η , and the diffusion coefficient D .

For proteins, the Stokes radius is typically in the range of 3 – 10 nm. In this work, the height of the proteins on the substrate are measured and compared with published values of their Stokes radius.

Membrane proteins When looking at membrane proteins for the assay described here, not their polymer structure is in the foreground, but the embedding and diffusion in a cell membrane. The central architectural feature of biological membranes is a double lipid layer. The major components depend on the cell type, but consist of approximately 1/3 proteins, 1/3 phospholipids, and 1/5 sterols (by weight) [44]. The mobility of membrane proteins within the membrane is crucial for the ability to pattern membrane proteins in a living cell by external anchors and can be described by the fluid mosaic model [45]: membrane proteins are embedded in the lipid bilayer and can diffuse in the lipid environment as in a 2D fluid (Figure 6.1A). Although this model was developed more than 40 years ago and has been continuously improved [46], the simple model still meets the requirements to understand the application in this thesis, even though a modern understanding of the membrane shows that it is much more complex (Figure 6.1B).

If the diffusion of the membrane proteins to be examined were restricted or very slow, it would not be possible to use this assay. Diffusion in a 2D fluid was theoretically described in the Saffman-Delbrück model in 1975 [47] and has been steadily improved [48, 49]. The diffusion coefficient D is described by the mean square displacement $\langle x^2 \rangle$ in the time t . It could be shown that for 2D diffusion the Navier-Stokes equation can not be simplified to the Stokes equation without the need for correction terms. In the case of 2D fluids, the ratio of the viscosity of the membrane μ_m to the viscosity of the surrounding fluid μ_f and the ratio of the membrane thickness h to the radius a of the simplified protein (a cylindrical inclusion) play a not insignificant role:

$$D = \frac{\langle x^2 \rangle}{2t} = \frac{k_B T}{4\pi\mu_m h} \left[\ln \left(\frac{h\mu_m}{a\mu_f} \right) - \gamma \right] \quad (6.2)$$

with the Boltzmann's constant k_B , the temperature T and the Euler-Mascheroni constant $\gamma \approx 0.577$.

For lipids, the diffusion coefficient is approximately $1 \mu\text{m}^2\text{s}^{-1}$. The mobility of membrane proteins depends on their function and are typically lower than the coefficient for lipids. At the lower end of the spectrum is fibronectin, which is anchored to actin filaments on the intracellular side by integrins and has a coefficient D of less than $10^{-4} \mu\text{m}^2\text{s}^{-1}$ [50]. Theoretically, it would therefore take about 6 days for a fibronectin in the cell membrane to cover the distance of $10 \mu\text{m}$ by diffusion, whereas for a lipid it would take less than 1 min.

Proteins of interest On coated glass substrates, three types of proteins are indirectly and directly structured in this work: streptavidin, fibronectin, and bovine serum albumin (Figure 6.2).

Streptavidin (SAV) is a 52.8 to 66 kDa protein homotetramer. Due to its high biotin activity with a dissociation constant of about 10-14 mol/L, it is widely used in

6. Protein patterning

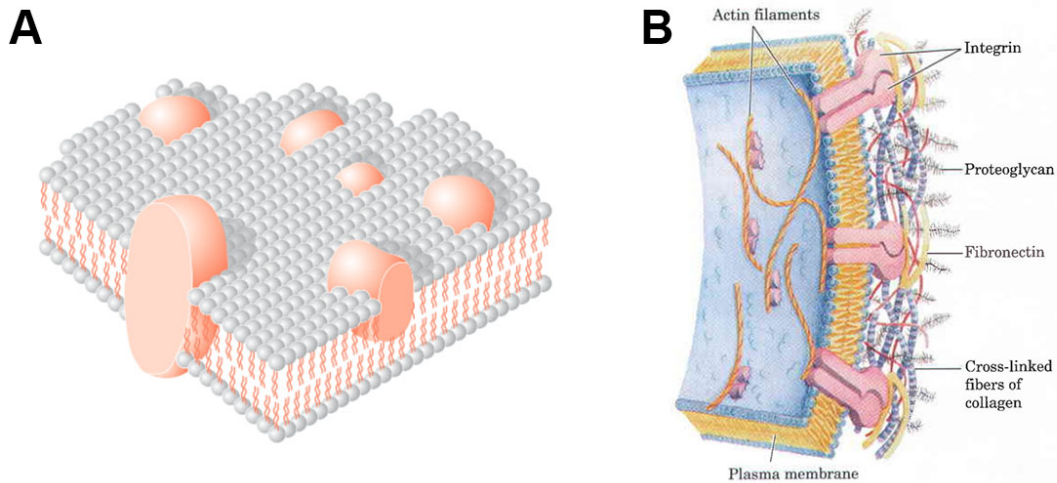


Figure 6.1.: (A) This early model described proteins diffusing in a 2D-liquid of lipids. (B) A more modern approach expects a more crowded membrane which influences the diffusion of the proteins to a great amount. In this sketch, the asymmetry of the membrane is shown by the exposed fibronectin with binding sites for both integrin and the proteoglycan. Both modified from [44].

biotechnology. It is the strongest noncovalent interaction known in nature and usually disturbed only by conditions that result in irreversible denaturation of the complex [51]. Since many macromolecules can be biotinylated, it is often used as a biological adhesive for research methods and biotechnological techniques [17, 52, 53]. In addition, due to the stability of the streptavidin-biotin complex to organic solvents, denaturants (eg, guanidinium chloride), detergents (eg, SDS, Triton), proteolytic enzymes, and extreme temperatures and pHs, it became widely used in molecular biology and bionanotechnology [54, 17]. However, the protein tends to aggregate in solution when rehydrated after lyophilization at a neutral or acidic pH [55]. It has a Stokes radius of about 4 nm [56].

Fibronectin (FNT) is a high molecular weight (440 kDa) extracellular matrix glycoprotein. FNT is widely used to mimic the native extracellular matrix and promote cell adhesion to solid substrates [57, 58, 59]. Its size in solution varies in length from 160 nm [60] to 8.7 nm [61]. While SAV can represent the anchor regions, FNT functions as a blocker, but in addition with cell adhesion. Due to the importance of the equidistant contact for TIRFM, fibronectin can ensure the anchoring of the cell even in the blocking areas.

An alternative blocking protein is bovine serum albumin (BSA) of about 67 kDa, comparable in size to SAV. Since it is a relatively small, stable, poorly reactive protein, it is often used as a blocker in various applications. It has a Stokes radius of 3.48 nm [62]. Cells do typically not adhere to BSA.

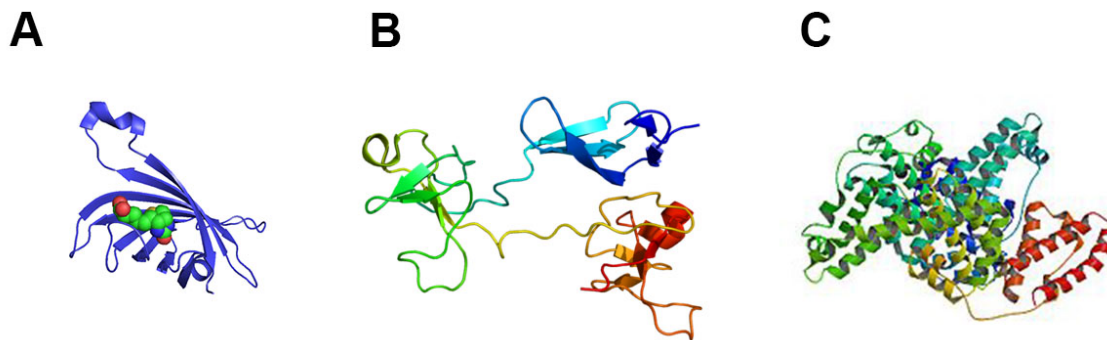


Figure 6.2.: Ribbon diagrams of the proteins applied in this thesis. (A) Streptavidin monomer with captured biotin. (B) Fibronectin. (C) Bovine serum albumin. From [63, 64, 65]

6.2. Patterning of proteins

Micropatterning In recent years, surfaces featuring micropatterns of biomolecules, particularly proteins, have seen a surge of interest. They have found multiple applications in biomedical research such as stem cell differentiation [66, 67], microarrays [68, 69, 70], proteomics [71, 72], and biomimetic sensors [73]. Furthermore, micropatterned surfaces have been applied to influence the protein distribution in living cells to address several cell biological questions [74, 75, 76, 77, 78, 79, 21]. Different techniques have been developed for fabricating patterned surfaces which cater to the demands of the respective applications.

One family of techniques is based on indirect deposition of proteins; the most prominent of these are photolithography [80, 81] and laser microablation [82], where the minimum feature sizes are set by the diffraction limit of light. Methods based on direct deposition of proteins include maskless projection lithography [83], microfluidic patterning [84, 85], and contact-based printing. The latter itself expands to a wide range of methods where microcontact printing (μ CP) stands out as a convenient, cost-efficient, and straightforward method [86, 11]. Therefore, μ CP with poly(dimethylsiloxane) (PDMS) has found its way into many laboratory applications for micropatterning of proteins.

Nanopatterning While several convenient methods exist today to create microstructured surfaces, the fabrication of patterns with a feature size below $1\ \mu\text{m}$ is still challenging and often requires trade-offs between speed, biocompatibility, cost, versatility and experimental complexity. However, to enable the development of a new generation of high-performance nano-biointerfaces for proteomics and cell research, the miniaturization of protein patterns down to the nanoscale is necessary: nanostructured surfaces would not only match typical length scales of cellular plasma membrane structures, they

6. Protein patterning

further fit capabilities of state-of-the-art super-resolution microscopy readout technologies [87]. For this purpose, dip pen nanolithography [88, 89], electron beam lithography [90] or STED lithography [91, 92] have the advantage of a high resolution and full freedom of choice regarding the created protein patterns, but are typically slow and require complex procedures and equipment. Other techniques for nanopatterning which overcome the restriction of the diffraction limit are colloidal lithography [93], di-block copolymer micelle nanolithography [94, 95], di-block copolymer self-assembly [96], or the indirect deposition employed by electropolymerization to functionalize gold micro- and nanoelectrodes with proteins [97].

On the other hand, μ CP has seen widespread adoption due to its simplicity and good performance. However, printing with PDMS stamps typically results in sagging of the interspaces or pairing for features significantly below 1 μm [10, 98, 38]. Therefore, many creative methods were developed to circumvent the limitations of PDMS as a stamp material for nanocontact printing. One successful approach to create features below 100 nm by contact printing made use of silicone stamps with pyramidal features [99, 100]. A drawback of this stamp architecture is that only periodicities in the micrometer range can be realized. A different strategy to improve resolution is to increase the Young's modulus of the stamp material. This, however, can entail changes of the material properties compared to PDMS with respect to surface energy, as well as the necessity for complex procedures in stamp production. Thus, the fundamental advantages of silicone such as ease-of-use, compliant contact, and low surface energy, are often abrogated. For instance, polyolefin plastomers foils can yield imprints of superior quality in the sub-micrometer range compared to PDMS, however, the stamp development requires hot embossing [101]. Therefore, global flatness is hard to achieve after demolding and requires equipment with a high cost of ownership especially for larger stamps [102]. Furthermore, the material is not gas permeable which increases the appearance of trapped air bubbles, particularly in a manual printing procedure. Another example is the use of a PDMS derivative with increased Young's modulus of up to 9 MPa for printing proteins with a periodicity down to 210 nm [103]. The density of proteins that could be achieved with stamps featuring 100 nm pillars, however, was very low and imprints exhibited a number of defects. The quality of these patterns would not be sufficient for the protein-interaction-assay.

6.3. Protein adhesion promoter

Epoxide Epoxy coating is a very common adhesion promoter on glass and polymer substrates for proteins or nucleotides in both research and industrial production. Epoxide is a cyclic ether with a three-atom ring, which is strained and thus highly reactive. The opening of the epoxide ring is a strong electrophilic reaction, and alcohols, water and amines can serve as nucleophiles. An epoxide-silane bonded to a glass surface presents its epoxide ring and is called an epoxy coating. Upon contact with the amino group of

a protein, a nucleophilic attack occurs and the protein covalently couples to the surface (fig. 6.3A).

Epoxy coating has several great advantages. It is very strong (covalent) and can be produced evenly with a CVD process (Chemical Vapor Deposition). This allows monolayers of epoxide groups at industrial production level and is correspondingly low in manufacturing costs. The disadvantages, however, may limit its application. It reacts with water in a hydrolysis reaction, resulting in no longer functional, opened epoxide rings. In addition, the reactions of epoxides are non-specific, resulting in random covalent bonding and possibly decreasing the functionality of the protein ensemble.

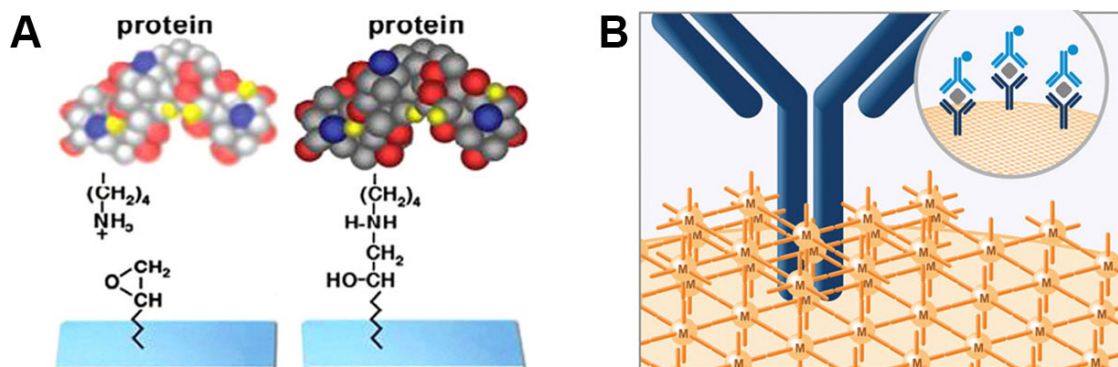


Figure 6.3.: Two coating strategies for protein adhesion promotion. (A) The epoxide ring covalently links to the presented aminogroup of a sample protein. (B) Anteo's Biosensor reagent forming a cluster of metal ions on the substrate holding an antibody. Modified from [104, 105].

Polymeric metal ion coating Polymer metal ion coatings are a relatively new option for use as adhesion promoters, but have already found several applications, particularly in the development of immunosensors [106, 107, 108, 109]. The coatings can be based on various metals, including cationic Cr (III) in polymeric form ($<5,000$ D) (fig. 6.3). This can form a coating about 1 nm thick and links by chelate chemistry with a suitable substrate such as glass or thermoplastics such as cycloolefin (co)polymer (COC / COP) [106]. A single interaction between a metal ion and the biomolecule would be neither strong enough to hold it in position, nor irreversible. Only with a multitude of weak compounds does the ion cluster produce a strong adhesion effect through avidity-binding interactions (Figure 6.3B). The bonding strength is comparable to the connection of streptavidin and biotin [105].

Experiments with captured streptavidin and biotinylated fluorophores have shown that this type leads to higher intensity bonding than, for example, an epoxy coating [105]. This could be explained by the fact that this coating does not generate a nonspecific covalent bond, but an immobilization that allows a rotation of the biomolecule. That would increase the likelihood of successful association with the antibody. In addition,

6. Protein patterning

the risk of irreversible chemical or structural modification that reduces the functionality of the biomolecule is reduced. The choice of a biomolecule is limited in this case such that the coating can only be used if the reagent has an electron donor potential.

Compared to the epoxy coating, the biosensor coating does not react with water. However, buffers with strong chelating potentials such as PBS should be avoided since they could passivate the surface. To the best of our knowledge, a polymer metal ion coating has not been used for contact lithography.

7. Microscopy

7.1. Atomic force microscopy

Atomic Force Microscopy (AFM) is a non-optical microscopy technique developed by IBM in 1982 for nanoscale surface measurements [110]. The core of an AFM consists of a cantilever with a fine nanoscale tip (Figure 7.1B,C). The cantilever is positioned near a surface so that the tip can interact with the surface molecules. A laser is reflected from the back of the cantilever to a position detector, and a feedback loop processes the information from the detector and responds via a control unit (Figure 7.1A). The AFM scans arrays point by point and creates a 2D image with the topology on the third axis. Software algorithms help to get an interpretable image from the recording through leveling and other functions.

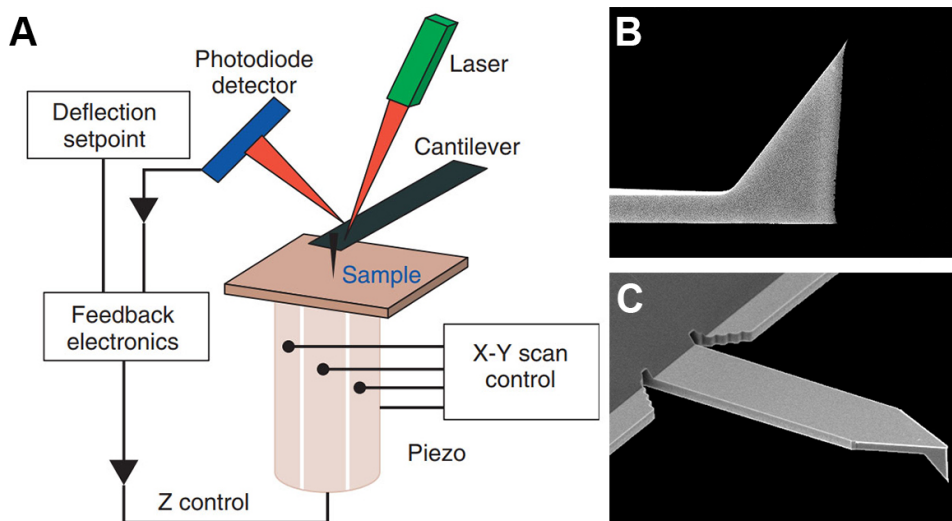


Figure 7.1.: (A) The principle setup of an AFM. A cantilever interacts with forces on the sample surface while the laser reflection is measured. A feedback loop controls the cantilever’s height measured by the position change of the reflected laser. The voltages applied to raise or lower the cantilever to keep the position where the laser strikes the detector constant serve as the height input for the image [118]. (B,C) SEM-images of OTESPA-R3 cantilevers with a tip radius of 7 – 10 nm. Modified from [118, 119].

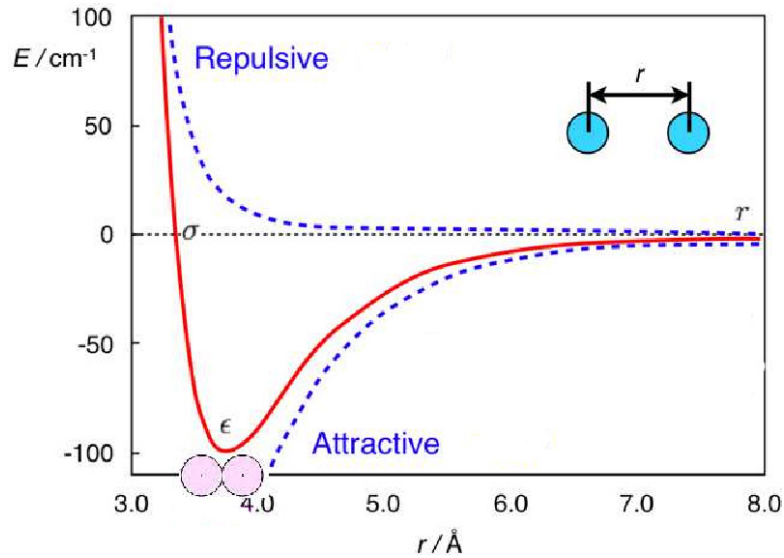


Figure 7.2.: The Lennard-Jones potential is a simple model that describes the interaction between two neutral atoms depending on their distance r . It is composed of two terms. In the far field, the attractive term dominates with r^{-6} , which can be made up of van-der-Waals interaction effect or permanent dipole-dipole interactions. As soon as the orbitals overlap, the repulsive term dominates with r^{-12} . Modified from [111].

The first developed mode for AFM was the contact mode. The tip of the cantilever touches the measured surface while maintaining the height of the cantilever to the surface or the applied force constant (constant height / force mode). Since this happens at the atomic level, touch means that the distance is smaller than the minimum of the Lennard-Jones potential and the tip is strongly repelled by interelectron effects (Figure 7.2). The shape of a particle measured in this way is calculated from a convolution of the shapes of the cantilever tip and the particle itself. For soft materials such as proteins, this is of particular importance since the tip usually becomes dirty within a few measurements. The attached proteins increase the tip radius of the cantilever and the AFM image may lead to wrong conclusions.

A second mode is the non-contact mode. The cantilever vibrates near its resonance frequency without touching the surface. In this mode, forces such as Van der Waals, dipole-dipole interaction, electrostatics, etc. play an influential and often attractive role. The forces cause the amplitude of the cantilever oscillation to change (normally decrease) as the surface-to-peak distance decreases, while the feedback loop adjusts the height to keep the amplitude constant. Alternatively, a change of the resonance frequency could also be used as feedback in case of altitude changes.

Through continuous improvement of AFM technologies, it is now possible to measure other physical parameters such as mechanical, electrical, or magnetic properties [112]. The speed of the measurement also increased dramatically and allowed the direct imaging

of the thermal motion of membrane proteins with high-speed AFM [113, 114]. In this work, only the tapping mode (also called intermittent contact mode, dynamic contact mode or AC mode) was used to measure layers of proteins on a rigid surface. The cantilever vibrates as in non-contact mode, but the tip touches the surface as in contact mode. The tapping mode is gentle enough to scan even lipid bilayers and single molecular motors [115, 116, 117]. In addition to the topology, this mode contains information about the phase of the cantilever oscillation, which allows conclusions to be drawn about the stiffness of the surface. Both information was used to determine the quality of protein patterns.

7.2. Fluorescence microscopy

Jablonski diagram There are molecules that can absorb light and thereby turn into an excited state. This can be explained graphically with the Jablonski diagram, which abstractly describes the energy states of a molecule and the transitions between them (fig 7.3A). Absorption of a photon in this model represents the transition from the ground state S_0 to a higher level. Absorption can take place only if the transition energy corresponds to the energy of the photon:

$$E = h \frac{c}{\lambda} \quad (7.1)$$

with the Planck constant h , the speed of light c and the wavelength λ .

Typically, there is no direct transition from S_0 to S_1 , but a vibrational or rotational state of S_1 is reached. After absorption, non-radiative relaxations in less than $10^{-14} - 10^{-11}$ s seconds equalize the molecule to the lowest vibrational level of the excited state [122].

For thermodynamic reasons, a system wants to reach the lowest energy state, thus the excited state is not stable. The energy difference to the ground state can now be released in several ways: by thermal processes, radiation emission, photochemical reactions or a radiation-free energy transfer to another molecule. If the transition from an excited singlet state to the ground state takes place by emission of radiation, this radiation is called fluorescence or phosphorescence. Between excitation and emission are about 0.5 – 20 ns in fluorescence. Changing from a triplet state to the ground state can take much longer and is called phosphorescence [122]. A system that fluoresces is called a fluorophore.

For the construction of a microscope, an effect, which can also be illustrated with the Jablonski diagram, is of importance. If, as described, the excitation takes place between S_0 and a vibration level of S_1 , then relaxation leads to less energy being available for an emission. This is called Stokes shift or redshift, since the emitted wavelength in

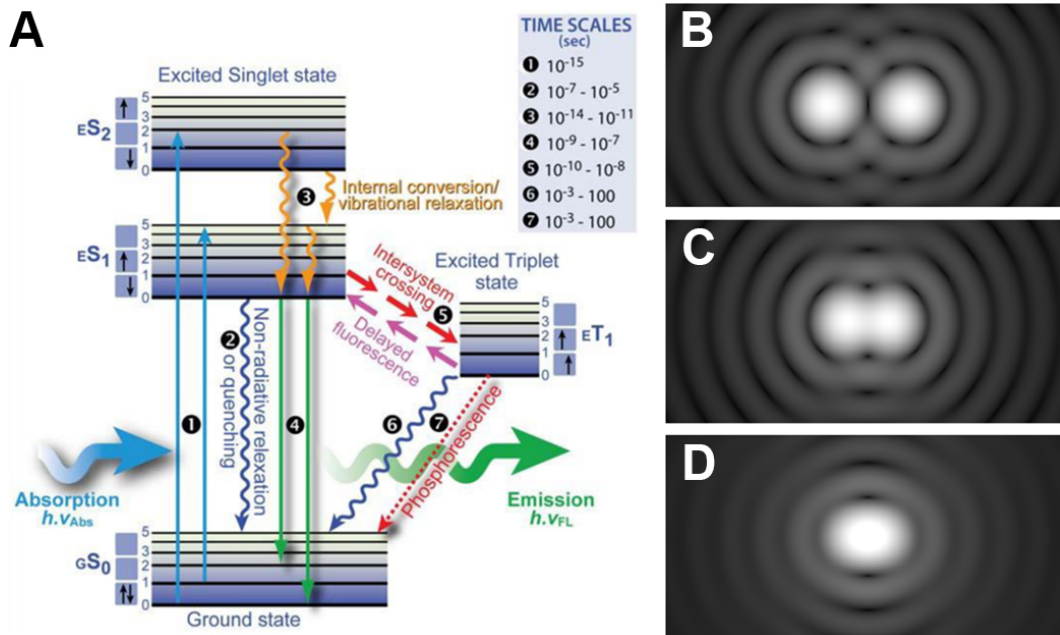


Figure 7.3.: (A) Jablonski diagram explaining the Stokes shift: the energy of the emitted beam is smaller than the absorbed one due to non-radiative transition which typically have a timescale several orders below the fluorescence. (B-D) Airy disks of fluorophores in three lateral distances: (B) clearly resolvable, (C) limit, and (D) not resolvable anymore after Rayleigh criteria. Modified from [120, 121]

comparison to the excitation light is greater. This makes it possible to protect the detector with a beam splitter and filter from the much stronger excitation intensity and ideally to record only the fluorescence.

Excitation In fluorescence microscopy, the excitation light is typically blocked and the red-shifted emission light is detected. But if a sample is illuminated directly, fluorophores outside the focal plane would also be excited and contribute to the background noise. Therefore, several methods have been developed that allow local excitation and therefore improve signal-to-noise ratio (SNR). Examples are the confocal microscopy, multiphoton microscopy, sheet-light microscopy, or total internal reflection fluorescence microscopy (TIRFM).

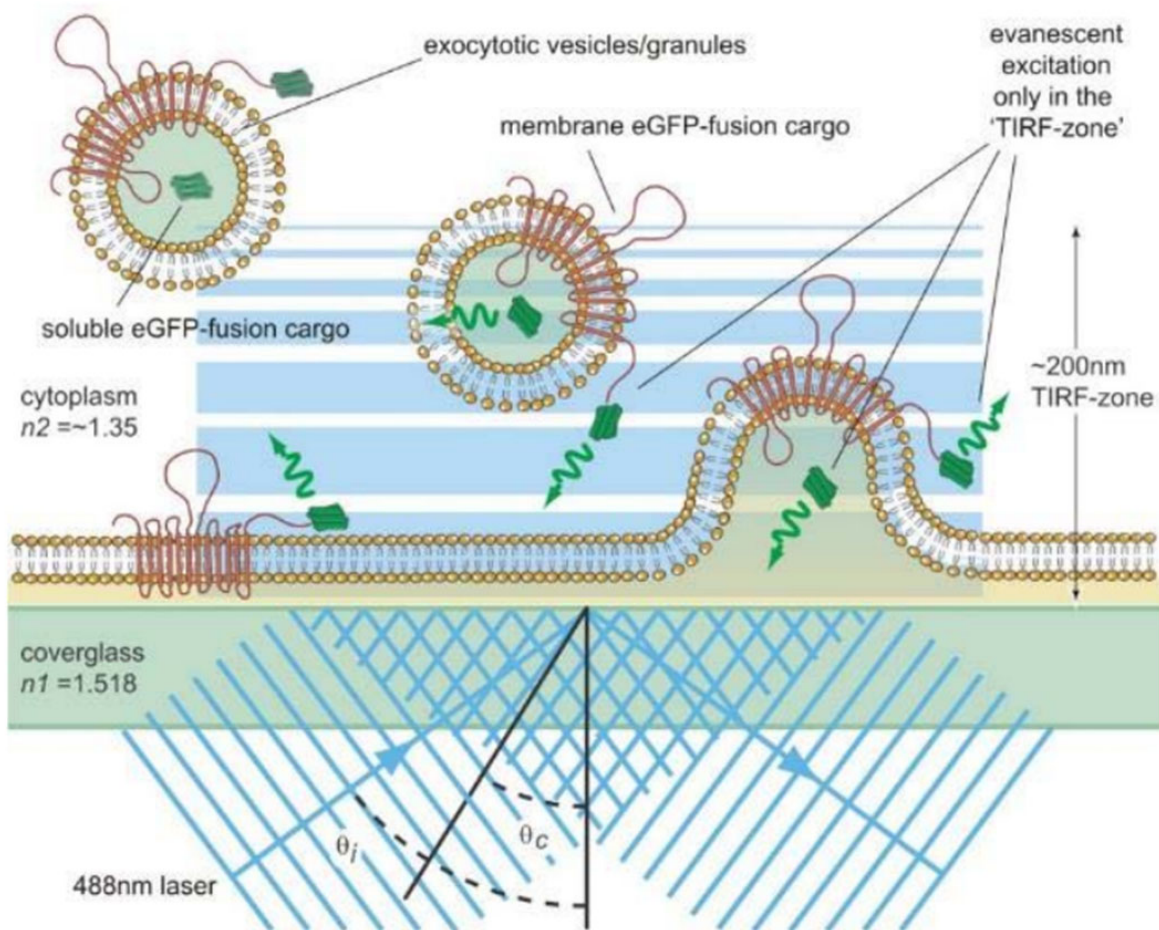


Figure 7.4.: Total internal reflection is the requirement for TIRFM and appears for transitions from the optical thicker medium to the thinner one. It produces an evanescent excitation only in the TIRF-zone which has a height of around 100 – 200 nm and depends among others on the laser angle. From [123]

7. Microscopy

In TIRFM, total reflection is used in the transition from medium 1 to medium 2. This means that according to the rules of linear optics no light propagates into the medium 2. This occurs when the transmitted beam is tangent to the interface and is thus only possible if the beam goes from the optical thicker to the thinner medium ($n_1 > n_2$) with the refractive index n).

With the laws of electrodynamics, light can be interpreted as a electromagnetic wave E with intensity $I \propto |E|^2$, which results in an evanescent wave with exponential damping in the direction perpendicular to the interface:

$$I = I_0 e^{-z/d} \quad \text{with } d = \frac{\lambda}{4\pi} \cdot (n_1^2 \sin^2 \alpha_1 - n_2^2)^{-1/2} \quad (7.2)$$

with the maximum intensity I_0 , the depth z , the wavelength λ , and the entrance angle α_1 .

In TIRFM, this evanescent wave is used to selectively excite fluorophores at a limited depth adjacent to the glass-water interface (Figure 7.4). For the media glass and water as well as violet light, the intensity drops in practice for $d \approx 100 - 200$ nm to e^{-1} of their initial value. This depth is typically sufficient to penetrate a protein layer (5-10 nm), anchored antibodies (10 – 20 nm), and the fluorescent proteins in the cell membrane (5 nm) without activating fluorophores within the cell. However, when the cell forms bulges, the excitation intensity decreases locally and low signals may be misinterpreted as areas with fewer fluorophores.

For our application TIRFM offers several advantages. It shows a low background noise and due to the lower light damage, the survival of the cells is significantly increased. Despite all advantages, TIRFM is still a diffraction-limited microscopy technique.

Resolution A point light source is imaged by a lens into a point spread function (PSF) due to diffraction effects. For a circular lens and aperture, the PSF in the far field has the shape of an Airy pattern. The distance d from peak to the first minimum depends on the wavelength λ :

$$d = \frac{1.22}{2} \frac{\lambda}{\text{NA}} = 0.61 \frac{\lambda}{n \sin \alpha_1} \approx \lambda/2 \quad (7.3)$$

with the numerical aperture NA of the lens which is defined as a product of the refractive index of the medium and the sine of the lens angle aperture.

Due to this diffraction effect, a fluorophore with a size below 10 nm is projected as a disk with a diameter of around 200 nm, independent of further magnification or detector.

Thus, so that two fluorophores can be distinguished from each other, their distance must meet a minimum. Here the Rayleigh criterion can be applied (Figure 7.3B-D): The minimum distance for resolving two point sources is reached, if the intensity maximum of one image coincides with the first minimum of the other [124, 125]. If the resolution is defined according to this criterion, it is identical to the location of the first minimum and equation 7.3 applies.

With a very good objective $NA = 1.44$ and the emission wavelength of a green fluorescent protein (Clover) at 515 nm, the resolution can be estimated at 180 nm. To visually resolve fluorophores that are closer together, super-resolution techniques must be used.

7.3. Direct stochastic reconstruction microscopy

Direct Stochastic Reconstruction Microscopy (dSTORM) is a single-molecule, high-resolution microscopy technique [126, 127, 128]. The idea is that the center of an Airy disk corresponds to the position of the fluorophore and can be localized when enough photons are collected. If it is ensured that the PSF is represented by only one molecule, its position can be detected with an accuracy below the diffraction limit, even if only a few pixels of the camera have been covered (Figure 7.5A-C). In this way, this method would still be bound to the Raleigh criterion, and fluorophores less than 200 nm apart could not be resolved if they emitted simultaneously.

By suitable fluorophores and an associated buffer medium, it is possible to ensure that the fluorophores are activated at different times. Specifically, at the beginning of the measurement, all fluorophores are transferred to a non-fluorescent state. Either spontaneously or induced (for example by a second laser), a subset of fluorophores is reactivated. In this case, the probability of activation must be sufficiently low that stochastically every active fluorophore has a distance of more than 200 nm to the next emitting fluorophore. This ensures at all times that the visible fluorophores can be dissolved and localized. Only the iteration of deactivation, activation and localization yields images of spatially unresolvable molecules. If a stack of images with the calculated PSF-centers is superimposed, a completely reconstructed image with a resolution of 10 – 50 nm is obtained (Figure 7.5 D).

7.4. Stimulated emission depletion microscopy

In stimulated emission depletion (STED) microscopy, the high resolution is achieved by a second laser. A typical STED setup has a pulsed excitation laser that illuminates the sample and excites the fluorophores to the first excited singlet state S_1 . A synchronized and redshifted second laser is also pulsed and centered exactly at the same position but

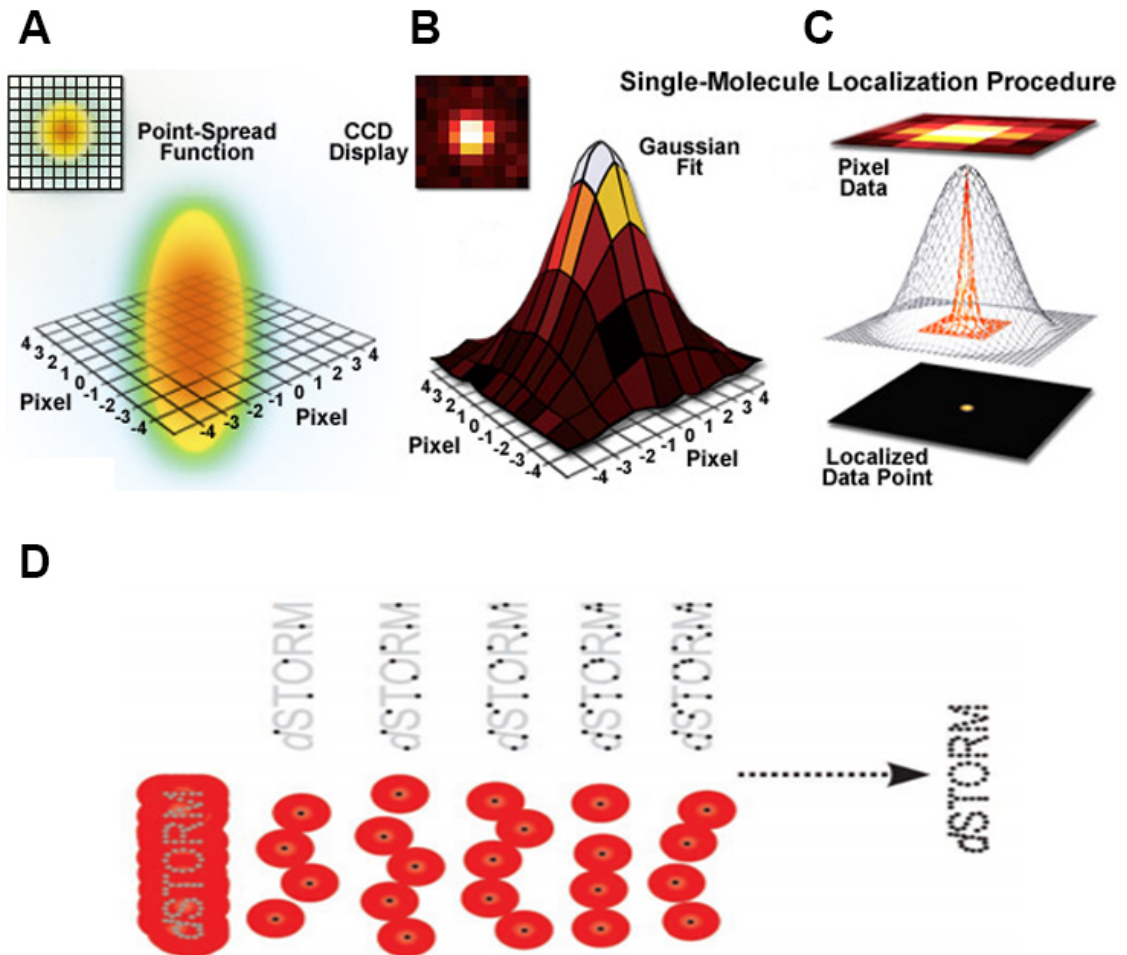


Figure 7.5.: dSTORM is based on the localization of single molecules. (A) If focused on the sensor, the PSF of a single molecule covers several pixel. (B) With a Gaussian fit, (C) the center of the PSF and such the position of the fluorescing molecule can be calculated. (D) Taking several images of localized molecules, the sample can be reconstructed with an effective resolution far below the diffraction limit. Modified from [126, 127]

with much higher intensity. This laser is called a depletion laser and goes through a 2π phase plate (Figure 7.6A) which gives the laser a donut-shaped intensity distribution. The center (node) of zero intensity is surrounded by an exponentially increasing intensity towards the periphery. The wavelengths and durations of both laser pulses must be carefully selected according to the photoswitchable fluorophores.

The depletion laser frees an area around the node by stimulated emission and transfers the fluorophores to the ground state S_0 . Although both laser beams remain diffraction-limited as they pass through the optical system, only fluorophores in the center of the depletion donut now contribute to the image (Figure 7.6B). The extent of the node can be well below the diffraction limit and is strongly defined by the power of the depletion laser. Although higher intensity could reduce the size of the node to a few nanometers, photobleaching and destruction of the probe may occur. Especially if the probe has to be scanned with the depletion laser to get a complete image. A realistic resolution that can be achieved with an unmodified STED is 20 nm [126, 129].

One of the advantages of STED is that the image can be obtained without further processing. Its speed and resolution depend greatly on the configuration and the laser power. The choice of photoswitchable fluorophores also plays a major role in STED.

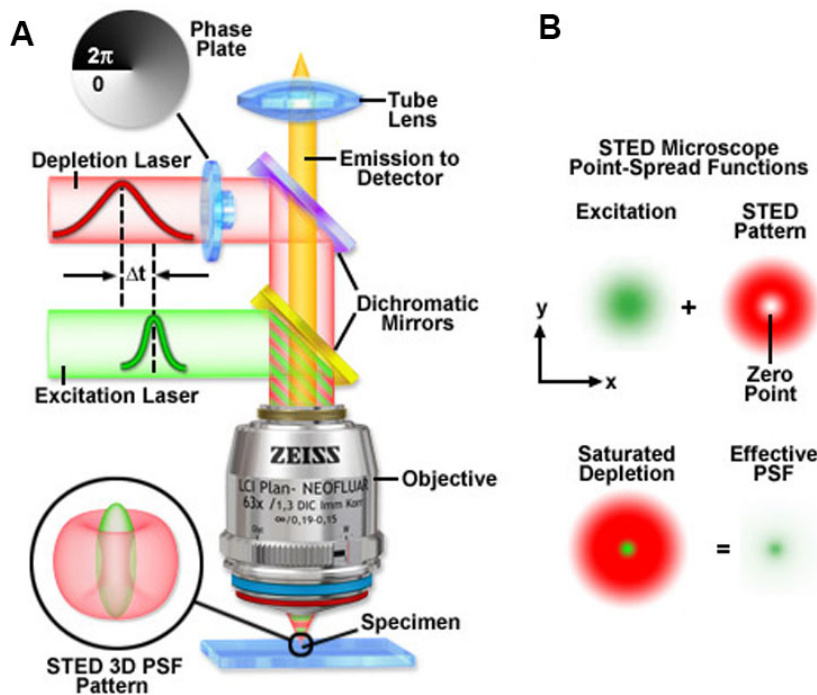


Figure 7.6.: (A) A minimalistic setup for STED. (B) The PSF of the depletion laser has a zero-intensity center. Combined with the excitation laser, an effective PSF with dimensions below the diffraction barrier can be achieved. From [126]



Die approbierte gedruckte Originalversion dieser Dissertation ist an der TU Wien Bibliothek verfügbar.
The approved original version of this doctoral thesis is available in print at TU Wien Bibliothek.

Part II.

Nanocontact printing with high-modulus silicones

8. Introduction

Microcontact printing (μ CP) is a very simple technique for creating two-dimensional patterns of proteins on a substrate. For μ CP, stamping material plays an important role in the printing process, and this also applies to nanocontact printing (nCP) (Figure 8.1). The hydrophobic, low surface energy of PDMS makes it an ideal stamp material for protein prints when presenting a high-energy substrate. In addition, its reusability and low modulus of elasticity make it highly accessible to laboratories because the required conformal contact can be ensured without a clean room or expensive equipment. For nCP, however, a material is needed whose advantages are comparable to those of PDMS, but which has a higher modulus.

The aim of this work was to increase the resolution of the interaction assays by structures with a periodicity of less than 200 nm. For this purpose, masters were initially produced by means of phase transition mastering and nickel plating, which, however, were limited to a period greater than 600 nm. However, the patterns produced were suitable for studying the influence of geometries and Young's modulus on the print result. Further investigations included the influence of substrate coating, the adsorption of proteins on the stamp and the stability of protein patterns. The samples were tested for their functionality with labeled membrane proteins *in vivo* using TIRFM. For patterns below the diffraction limit, STORM was used.

From the results it was deduced which combination of stamp material, adhesion promoter and process could yield protein patterns with a period below 200 nm. For this purpose, a master with the suitable geometry and a structure period of 140 nm was produced externally. It has already been shown in AFM images that, in addition to the factors mentioned above, the size of the nanoscale proteins also makes a decisive contribution to quality. In addition, there were difficulties in resolving this high density of fluorophores using STORM. Using STED, the nanostructures could finally be detected by optical methods.

Aspects of this part were open-access published in Lindner, Marco et al. "A Fast and Simple Contact Printing Approach to Generate 2D Protein Nanopatterns" *Frontiers in chemistry* vol. 6 655. 24 Jan. 2019, doi:10.3389/fchem.2018.00655

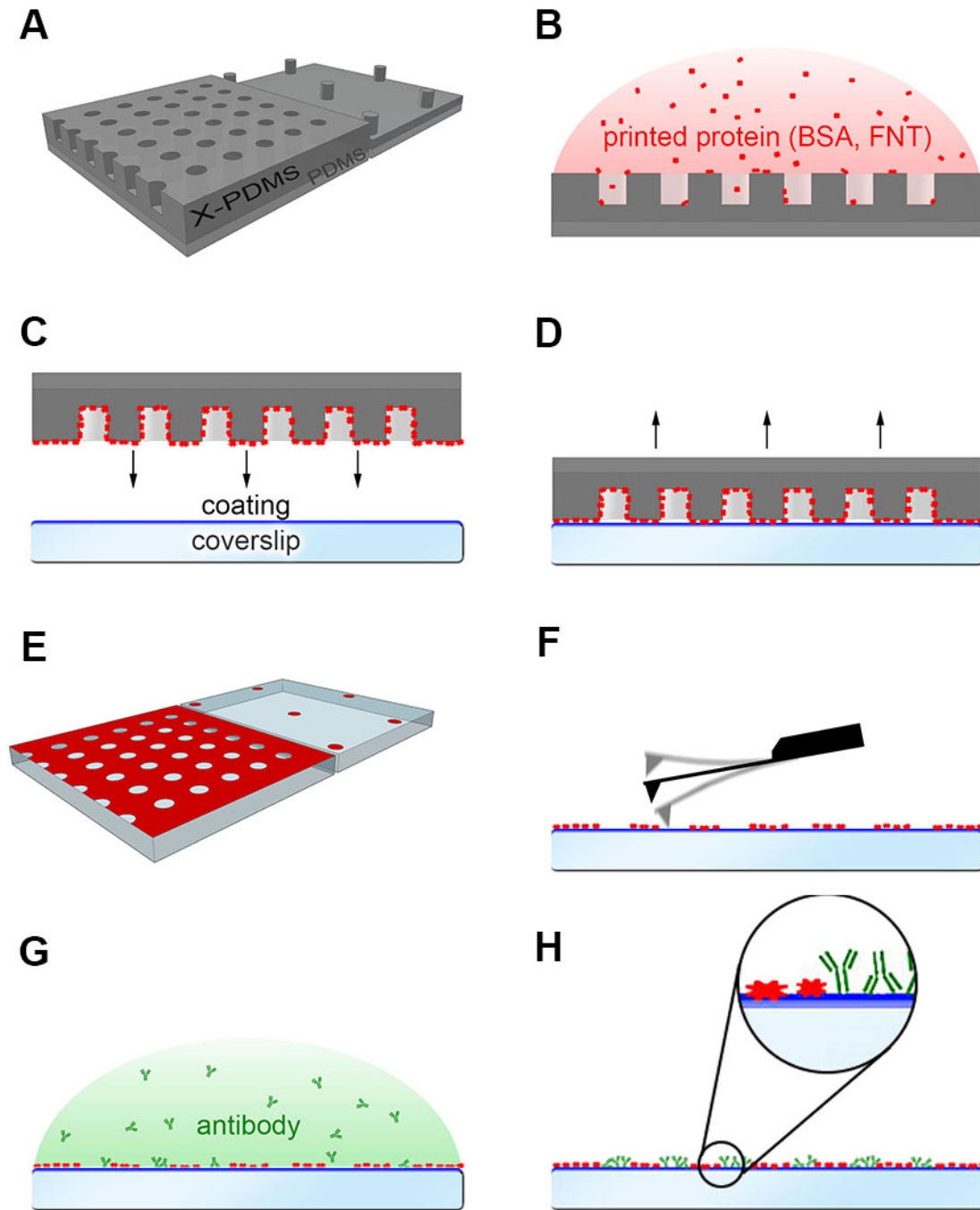


Figure 8.1.: Illustration of nanocontact printing of proteins. (A) Sketch of a stamp featuring a well (left) or pillar (right) layout. (B) The protein solution is incubated on the X-PDMS/PDMS stamp. (C–E) After washing and drying, the stamp is brought into contact with a coverslip coated with an adhesion promoter. The stamp is pressed onto the coverslip, incubated and removed, leaving the protein pattern on the coverslip. (F) The quality of the imprint is determined by AFM imaging. (G,H) After washing, the anchor proteins (antibodies or SAV if blocker BSA or FNT were printed or vice versa) are added to fill the interspaces, incubated and rinsed with water to remove unbound proteins.

9. Materials and Methods

Mastering A PTR-3000 acquired by Sony DADC AG, Austria, and modified by Sony DADC BioSciences GmbH, Austria, was applied for phase transition mastering of several PTM-masters. The diameter of the effective laser spot where the energy is above the threshold to crystallize the inorganic resist was around 100 nm. The designs in this thesis always represent the center of the laser spots, therefore, a 100 nm designed disc will result in 200 nm well diameter size. The developed PTM wafer was plated with nickel by Sony DADC, resulting in a eight inch inverse of the PTM wafer. The eight inch nickel masters were cut by a self-made tool to six inch disks for further processing.

Stamp development X-PDMS and intermediate layer pre-polymers were acquired by SCIL nanoimprint solutions, Philips (Netherlands). MED-6019 was acquired by NuSil™ Technology LLC (USA). All used silicones consist of two components which were carefully measured with an error less than 1 % in weight, thoroughly mixed with a polymer stick for at least 3 min and degassed in a centrifuge at 2000 rpm for 2 min. The master was spincoated with 3 g X-PDMS-pre-polymer on a WS-650MZ-23NPP by Laurell Technologies Corporation (USA) in two steps. First, just a small amount of the mixture was spincoated with 2000 rpm (4000 rpm for MED-6019) for 20 s to cover the whole wafer in a thin layer, then the rest of the pre-polymer was added and spincoated at 1000 rpm for 10 s. X-PDMS was cured incompletely for 10 min at 50 °C on a SKF Bearing heater (Sweden) and rested at RT for around 15 min. If the material was just slightly sticky anymore, the wafer was put back on the spincoater and the intermediate layer applied. The wafer was spincoated at 2000 rpm for 1 min. The unavoidable edge bead was ignored at this stage and cut away of the final stamp. The silicones was cured to a reach a specific Young's modulus as mentioned in the experiment. Finally, a compliant layer of Sylgard 184 by Sigma-Aldrich (USA) of around 0.5 – 2 mm was added and cured. If a thin backplane was applied, a glass cover slip provided stabilization. MED-6019 was cured for 2 h at 70 °C before the soft backplane was added directly. The durometer type A of the materials were measured with a RX-DD-A Shore A Digital Durometer with a OS-1 Durometer Test Stand by Eletromatic Equip't Co. Inc. (USA).

Substrate preparation Glass coverslips (#1.5, 24 × 60 mm; Menzel™, Fisher Scientific, USA) with a thickness of 150 μm were washed with acetone and DIW and dried in a stream of nitrogen. Around 50 – 100 μL of Mix& Go Biosensor wet coating by anteo technologies (Australia) was pipetted on the slide, protected from dust and rested for

at least 45 min and a maximum of 90 min. Then it was pipetted for reusage, washed with DIW and again dried with nitrogen. Although Biosensor coated samples could be stored for several weeks, they were typically used in less than 24 h. For the plasma treated slides, a diener electronics (Germany) ATTO plasma system (13.56 MHz) was used with oxygen for 30 s with a vacuum of 0.3 mbar and 50 W. The epoxy coated glass substrate were purchased by SCHOTT NEXTERION® (Germany).

Incubation Proteins were soluted in Millipore filtered DIW, the concentration were typically around $100 - 1000 \frac{\mu\text{g}}{\text{mL}}$. For protein incubation and washing tests of PNAM, SecureSeal™ Hybridization Chambers by GRACE Bio-labs, USA, were placed on top of the patterns.

For STED microscopy, goat anti-rabbit IgG antibody conjugated with STAR RED (Abberior, Germany) was diluted 1:50 in PBS to a final concentration of $20 \frac{\mu\text{g}}{\text{mL}}$. Again a Secure-Seal™ hybridization chamber was placed and filled with 50 μL of the antibody solution, incubated for 15 minutes and washed with 1 ml of PBS to remove unbound antibody.

AFM Atomic force microscope measurements were performed with a Bruker Dimension V, Digital Instrument, France. Cantilevers were (if not otherwise stated) Bruker OTESPA-R3 with a tip radius of 7 – 10 nm, a resonance frequency at around 300 kHz, and a spring constant of $k = 26 \text{ N/m}$. The experiments were executed in tapping mode with a typical scan rate of 0.5 Hz. Both proportional and integral gain were adapted for each measurement but were in the order of 0.5 and 2, respectively.

For analysis, Gwyddion version 2.49 was used. The correction algorithms "remove polynomial background", "align rows using various methods", "correct horizontal scars (strokes)", "shift minimum data value to zero", and "stretch color range to part of data" were typically applied in this order. For the roughness analysis, "statistical analysis" was performed, for the profile it was "extract profile", for the height distribution it was "calculate 1D statistical functions".

SEM For SEM images, a Hitachi S-4000 (Japan) with EMI compensation system MK3 by Integrated Dynamics Engineering (Germany) was used. Before the samples were put into the vacuum chamber of the SEM, they were sputtered with a gold layer of approximately 30 nm. Only the secondary electron detection was used of the scanning electron microscope.

TIRFM Total internal reflection fluorescence microscopy (TIRFM) experiments were performed on a home-built system including a modified inverted microscope (Zeiss Axiovert 200) equipped with a 100x oil-immersion objective (Zeiss Apochromat NA1.46).

9. Materials and Methods

For excitation of the secondary antibody (goat-antimouse IgG-AlexaFluorophore 647) a 640 nm diode laser (coherent) was used. For excitation of hemagglutinin-mGFP (HA-mGFP) a 488 nm diode laser (Toptica, ibeam-smart) was applied. Emission light was filtered using appropriate filter sets (Chroma) and recorded on an IXON DU 897-DV EM-CCD camera (Andor). TIRF-illumination was achieved by shifting the excitation beam in parallel to the optical axis with a mirror mounted on a motorized movable table. All measurements with cells were performed in HBSS solution supplemented with 2% FCS at 23 °C. In order to check protein patterns of HA-mGFP, series of movies were recorded at an illumination time of 3 ms and a frame rate of 100 ms in the blue channel. Samples were also recorded without using cells, simply recording the signal from secondary antibody bound to antibody patterns. Under these conditions movies were recorded with 3 ms illumination and overall 100 ms frame rate in the red channel.

RICM A modified TIRFM-setup as described above was applied for RICM. A Zeiss HBO 100 mercury short-arc lamp with a spatial filter provided a parallel beam with a Gaussian profile which was included to the laser beam path for TIRFM. Typical exposure times were 50-100 ms.

dSTORM For dSTORM measurements, switching buffer conditions optimized for AF647 were used: PBS (pH 7.4) was supplemented with 10% glucose, 500 $\frac{\mu\text{g}}{\text{mL}}$ glucose oxidase, 40 $\frac{\mu\text{g}}{\text{mL}}$ catalase and 50 mM cysteamine. In dSTORM experiments with AF647, the majority of fluorophores was first transferred into a nonfluorescent dark state using high-power 640 nm laser illumination. Then, single molecules were imaged at 640 nm excitation at lower power, keeping the 405 nm laser continuously on in order to switch molecules back to a fluorescent state. Images were recorded as stacks of 10,000 frames at 100 Hz. Stroboscopic illumination protocols were applied with 3 ms illumination time and 7 ms delay between consecutive images. Single-molecule signal localization and image reconstruction was carried out with the open-source ImageJ plugin ThunderSTORM24. Stringent postprocessing parameters were chosen to discard signals with low localization precision. On average, localization errors of $\sigma = 20$ nm for AF647 were obtained. Merging of localizations was performed with a grouping radius adjusted to the average localization precision of the respective fluorophores. If not specified otherwise, 50 frames off-time was used. No drift correction was applied.

STED STED microscopy was performed on an inverted commercial STED microscope (Abberior Instruments, Germany) with pulsed excitation and STED lasers. A 640 nm laser was used for excitation and a 775 nm laser for stimulated emission. An oil immersion objective with numerical aperture 1.4 (UPLSAPO 100XO, Olympus, Japan) was used for imaging. The fluorescence signal was collected in a confocal arrangement with a single photon counting avalanche photodiode using a 685/70 nm bandpass filter. The pulse repetition rate was 40 MHz and fluorescence detection was time-gated. For

both STED and confocal images, a pixel size of 20 nm, a pinhole of 1.0 airy units and 3 line accumulations were used. The power values refer to the power at the back aperture of the objective lens. The imaging parameters used for acquiring STED images of W80 patterns were 40 μs dwell time, 41 μW excitation laser power and 80 mW STED laser power. The corresponding confocal images were recorded with 50 μs dwell time and 2 μW excitation laser power. For both STED and confocal images, a pixel size of 10 nm, a pinhole of 0.9 airy units and 3 line accumulations were used. The imaging parameters for acquisition of the STED images of W300 patterns were 40 μs dwell time, 84 μW excitation laser power and 94 mW STED laser power. The corresponding confocal images were recorded with 50 μs dwell time and 12 μW excitation laser power.

10. Nanocontact printing with PTM-fabricated masters

10.1. Phase-transition mastering of multi-pattern masters

With constant rotational speed ω the scalar velocity v of a point on the disk depends on the radius r : $v = \omega \cdot r$. A design with a period of 600 nm was placed on three radii: near the center, in the middle of the 8 inch wafer, and at the border of the wafer. The developed PTM-master showed the influence of the radii. From the inside to the outside, the measured radii were the following: 0.6 μm , 0.8 μm , 1.8 μm .

Therefore it was recommended to design the smallest features in close proximity to the center of the wafer. To understand the limitations of high-modulus silicones for nCP, a PTM master with eight different patterns was designed, beginning with A1 and A2 (smallest features and periods) near the center to D1 and D2 furthest away (Figure 10.1). The technical limits of PTM regarding diameter and period were reached with the A patterns. A1 was designed as wells with a diameter of 100 nm and A2 as wells with 300 nm. The pattern of A2 was inverted, leading to pillars in the PTM wafer. And taking the size of the effective laserspot of around 100 nm into account, both A1 and A2 resulted theoretically in features with a diameter of around 200 nm. Patterns for A1 with just a single point instead of an area should in theory produce the smallest wells. However, for patterns with less than 100 nm in diameter no PTM-parameters could be found that the written features could still be developed.

B showed the same features as A but with increased period. C and D have the same period as B but the feature sizes increased even further. Table 10.1 lists the design for the PTM writing process, figure 10.1A visualize it.

Details to the PTM-writing and development parameters are company secrets. However, by carefully increasing the laser energy of the PTM and also increasing the development duration, the durometer of the pillars could be decreased to 80 nm but this also broadened the wells for this master. Therefore, two master variations based on the same design were developed. One was applied mainly for pillars, the other one for wells.

Due to the phase transition process, the lower areas of the PTM-master showed a higher

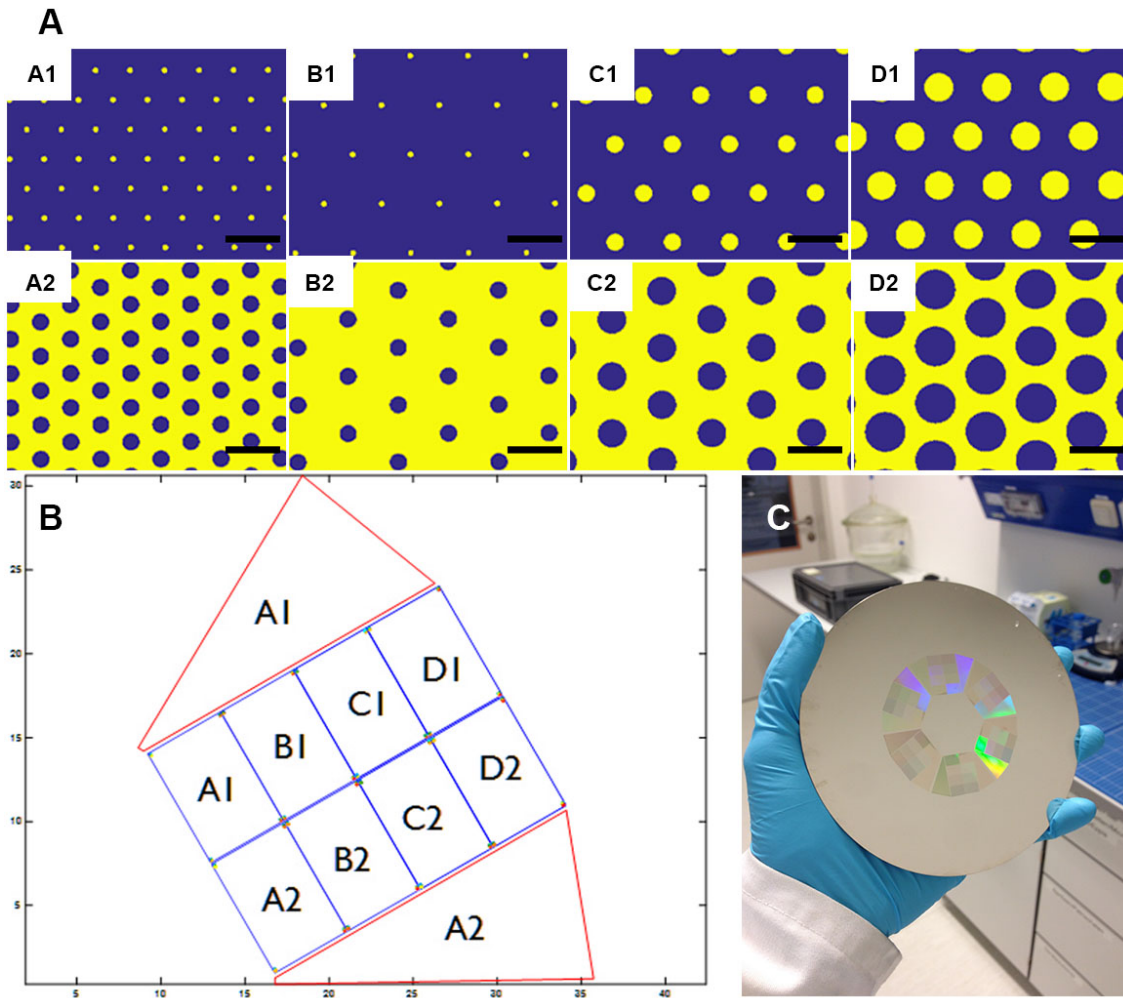


Figure 10.1.: (A) Overview of the design for the PTM-master. The yellow areas represent the center position of the laser beam for the writing process. The final size depends among others on the laser spot size and can be adjusted by its intensity and development duration. (B) Positioning of the patterns on the wafer. The smallest features A1 and A2 were also written into the triangles to test the PTM writing stability regarding the radius to the center and to increase the usable patterned area. The macroscopic pattern got circular repeated six times. (C) Plated with nickel and cut to 6 in, the final master showed interferences with visible light. All scale bars are 1 μm .

Table 10.1.: Design for PTM mastering. Inverted means, that the area outside of the small disks with the given diameter is written with the PTM-laser, resulting in pillars after development. From PTM master to silicone stamp, the features get copied two times, thus the listed forms also represent the patterns on the final stamp.

| Type | Diameter [nm] | Period [nm] | Inverted | Final Form |
|------|---------------|-------------|----------|------------|
| A1 | 100 | 600 | no | wells |
| B1 | 100 | 1000 | no | wells |
| C1 | 300 | 1000 | no | wells |
| D1 | 500 | 1000 | no | wells |
| A2 | 300 | 600 | yes | pillars |
| B2 | 300 | 1000 | yes | pillars |
| C2 | 500 | 1000 | yes | pillars |
| D2 | 700 | 1000 | yes | pillars |

roughness and more defects than the top side of the sputtered PTM layer. One plating step and imprinting this inverse with silicone had the advantage that the smooth top side of the wafer represented the contact area of the final silicone stamp. In addition, nickel forms an inert oxide layer if exposed to an oxidizing environment [130]. Nickel is in fact one of the model metals for oxidation studies since it forms only one type of molecules, NiO, under a wide range of conditions. It starts at nucleation spots and coalesce, forming a NiO film with a thickness of several monolayers which inerts the surface [131]. To ensure a complete isolation, a resting phase of one week at RT was kept for the nickel masters. No further coating or polishing was applied. The next step was the production of silicone stamps with these molds.

10.2. Development of composite stamps of high-modulus silicones

Two materials were chosen for silicone stamps: X-PDMS and MED-6019. The main application for MED-6019 from Nusil is the fabrication of medical devices. It is comparable to h-PDMS in Young's modulus and tensile strength [132] and therefore very likely linearly polymerized. However, only sparse information was available. X-PDMS on the other hand uses branched polymerization, its modulus was extensively optimized [38].

The durometer type A of the materials was measured for several temperature and duration combinations. X-PDMS cured for 2 h at 50 °C reached a modulus $E = (5.0 \pm 0.7)$ MPa while for long-term cured X-PDMS (10 days) at 70 °C a modulus $E = (80 \pm 5)$ MPa was measured.

Table 10.2.: Comparing properties of applied silicones. The values for PDMS (Sylgard 184) can be found in literature [39], for X-PDMS by Philips [38, 19]. For MED-6019 the data was made available by NuSil [132], its durometer was measured. * calculated with the estimation 10.1. ** Mentioned here for comparison, not tested in this thesis.

| | PDMS | H-PDMS ** | MED-6019 | X-PDMS |
|-------------------------|-------------|-----------|-----------|-------------|
| Young's Modulus E / MPa | 1.3 - 3 | 9 | 7-9 * | 5 - 80 |
| Durometer Type A | 33 - 56 * | 80 * | 75 - 80 | 68 - 98 * |
| Tensile Strength / MPa | 3.5 - 7.6 | 10 - 15 | 9.0 | unknown |
| Typical curing time | 15 - 45 min | 2 - 8 h | 0.5 - 3 h | 2 - 10 days |
| Polymerization | linear | linear | unknown | branched |
| Main application | various | NIL/nCP | medical | SCIL |

For most experiments long-term cured X-PDMS stamps were used. However, the short-term cured X-PDMS was of special interest for the testing of the geometrical limits in correlation to the stamp modulus.

An overview of key data are summarized in table 10.2. Durometer and modulus are always measured in bulk. The wide range of the curing time is explained by its strong dependency on the curing temperature. If the Young's modulus E was given but not Durometer Type A or vice versa, it was calculated with the following approximation [133]:

$$E = \frac{0.0981(56 + 7.62336S)}{0.137505(254 - 2.54S)} \text{MPa} \quad S \text{ is Durometer type A} \quad (10.1)$$

This relation is only valid for $S > 40$ which applies to all tested high-modulus silicones. The durometer values for PDMS are partly below this limit and should be treated with care.

The two components of X-PDMS were carefully measured with an error less than 1 % in weight. This is critical since more than 3 % difference has already a measurable impact on the modulus [38] and thus would not allow reproducible experiments.

We tested X-PDMS without a backplane and different curing parameters but this resulted in a brittle stamp which could not be removed intact from the master, leaving residuals in the cavities. This also happened with MED-6019 for curing times higher than 3 h. Consequently, we decided to use composite stamps with at least two layers: a high-modulus feature layer and a softer backplane. The second layer of common PDMS stabilizes the more brittle high-modulus feature layer. In addition, since most printings were performed manually, it supports the conformal contact and cushions the natural shaking of the hand which allows printing in the nanoscale without sophisticated equip-

ment. For SCIL, typically a third layer of glass is added to stabilize the stamp. If this third layer was applied, it is mentioned in the experiment.

The stamps were fabricated as described in chapter 9 on page 36. Since X-PDMS was applied as a thin layer for SCIL, we could use the available data and experiences. On the other side, uncured MED-6019 has a higher viscosity than the X-PDMS pre-polymer and no information on the application of this silicone for nanofeatures was available. Therefore, we spincoated the mixed and degassed MED-6019 pre-polymer with both 2000 rpm and 4000 rpm for 20 s. The material was cured for 2 h on 70 °C and resulted in a thickness of 600 µm and 230 µm, respectively. For further experiments, only the parameters resulting in the thinner layer were applied since it was comparable to the thickness of the other high-modulus silicone derivate (150 – 200 µm).

Scanning electron microscopy (SEM) and AFM images were taken of the stamps (Figure 10.2). During SEM, an electron beam is focused on a surface in a high vacuum. The scattered electrons from the sample material, also called secondary electrons, are captured by a detector. Their intensity depends, among other things, on the topology, since not as many electrons reach the detector from deeper areas as from high features. An image is output in grayscale, with lighter regions typically describing more exposed areas. The surface must be conductive, otherwise it would be charged very quickly and the signal-to-noise ratio would decrease dramatically. Typically, a thin layer (10-30 nm) of gold is sputtered onto the surface for this purpose. This necessary conductive layer makes SEM a destructive quality control method in our case. In addition, the 30 – 50 nm gold layer is responsible for the rounding of pillars and wells, especially visible for the smallest features. However, SEM is ideal for checking the quality of larger areas and we could confirm that all features were copied very well, no defects were visible besides trapped dust. This was hardly avoidable since the SEM was not located in a clean-room. On the other hand, AFM only allows spot checks, but these can be performed on the untreated X-PDMS stamp. Thus, the geometrical parameter were measured only at the AFM images, the feature diameter was measured at the top of the profile since only the top area is in contact with the substrate at nCP. The listed parameter can be found in table 10.3.

We measured the roughness of the stamp surfaces. There are several options to define roughness and we chose arbitrarily the root mean square R_{rms} which is defined as

$$R_{rms} = \sqrt{(1/L) \int_0^L H(x)^2 dx} \quad (10.2)$$

with the profile height function $H(x)$ and the evaluation length L .

It was calculated by Gwyddion, the applied analysis software for AFM measurements. The top side was taken at well stamps while the bottom at pillar stamps since these provided larger areas. As a result of the mastering process, the bottom $R_{rms} = 2.3$ nm

10.2. Development of composite stamps of high-modulus silicones

had a significantly greater roughness than the top side of the stamps $R_{rms} = 0.4$ nm. However, the difference was not as high as expected. Also, taking the tip size of around 7 nm into account, this values should be interpreted qualitatively.

Table 10.3.: Listing the stamp parameter, all with a depth of 100 nm. The abbreviations will be used in the thesis to identify the applied patterns for nCP. The feature diameter was measured at the top of the X-PDMS stamp with AFM. The values \pm SD were measured at three stamps and six positions on each stamp.

| Form | Abbreviation | Layout | Diameter [nm] | Period [nm] | Master |
|---------|--------------|--------|---------------|-------------|--------|
| | W300/600 | hex | 315 ± 30 | 585 ± 5 | A1 |
| | W300/1000 | hex | 305 ± 25 | 970 ± 4 | B1 |
| | W500/1000 | hex | 495 ± 20 | 970 ± 3 | C1 |
| | W500/1000 | hex | 700 ± 10 | 965 ± 5 | D1 |
| pillars | P80/600 | hex | 83 ± 8 | 586 ± 4 | A2 |
| | P80/1000 | hex | 87 ± 10 | 967 ± 5 | B2 |
| | P300/1000 | hex | 315 ± 20 | 971 ± 6 | C2 |
| | P500/1000 | hex | 500 ± 10 | 970 ± 7 | D2 |

10. Nanocontact printing with PTM-fabricated masters

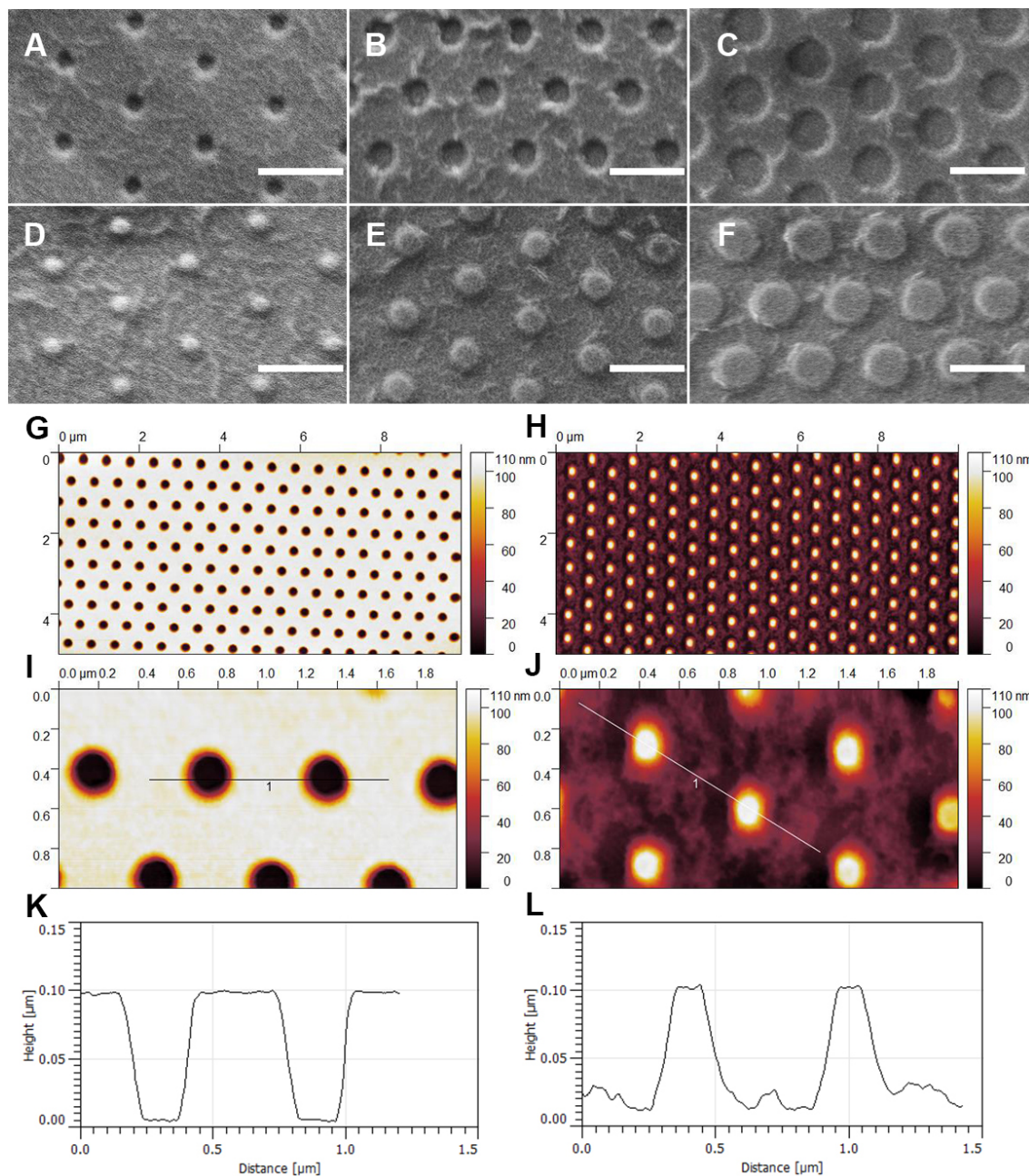


Figure 10.2.: SEM and AFM images of X-PDMS stamp. For SEM, the silicone had to be sputtered with around 20 nm of gold. This was unavoidable with our setup but slightly deforms especially the smallest features and was responsible for crack-like defects. (A) W300/1000, (B) W500/1000, (C) W500/1000, (D) P80/1000, (E) P300/1000, (F) P500/1000. (G,H) The smallest features which were achieved with our setup are shown for wells W300/600 and pillars P80/600, respectively. A detailed view (I,J) and the corresponding line profiles (K,L). Scale bars (A-F) 1 μm.

10.3. Characterization of nCP prints of proteins by AFM

Improvements in the nCP of proteins can only be achieved if the quality of the prints can be compared. For this purpose, two approaches were followed, both of which were based on AFM images. AFM in tapping mode is a gentle and non-destructive method that can provide detailed information on height and material stiffness.

Pattern quality by height histogram To quantify the periodicity and the pattern width, a line profile was used. For the height of protein patterns, their height histogram was used to obtain an average value. Ideally, it showed two distributions. One defines the height of the substrate, the other the top of the printed proteins. The distributions can be fit by a Gaussian curve and thereby their peak and their FWHM can be determined. The distances of the peaks of the two curves in the height histogram indicate an average protein level.

For the first approach of print quality characterization, two parameters were combined. The expected pattern is recognizable in different spots, and the height histogram. The results are summarized into three possible states: +, o, and -. + means two Gaussian curves in the height distributions can be fitted (f) and the expected pattern has to be recognizable by eye at several spots in AFM topological images (e): $f \wedge e$. - stands for no distinct distribution and no pattern at all: $\bar{f} \wedge \bar{e}$. o represents the remaining two options:

| | | |
|-----------|-----|-----------|
| Λ | e | \bar{e} |
| f | + | o |
| \bar{f} | o | - |

A success rate was defined as the ratio of numbers of + to number of prints n . The error bar was arbitrary defined as the inverse of the quantity of the experiments thus it decreases with number of experiments. The reason for this combination of partly subjective values was that there could be cases where f is positive but e is negative. This happened if the stamp showed defects, the patterns were only visible in certain areas or if partial sagging appeared. e positive but f negative would mean that the pattern could be recognized by eye but not be measured with the histogram as described above.

The full width at half maximum (FWHM) of Gaussian fits is also an indicator of print quality. A large FWHM indicates a topologically heterogeneous surface. The FWHM should therefore be as small as possible, especially for the glass surface.

Pattern quality by contrast The second approach of characterization is common in fluorescence microscopy. For this, AFM images were converted to 16 Bit greyscale images

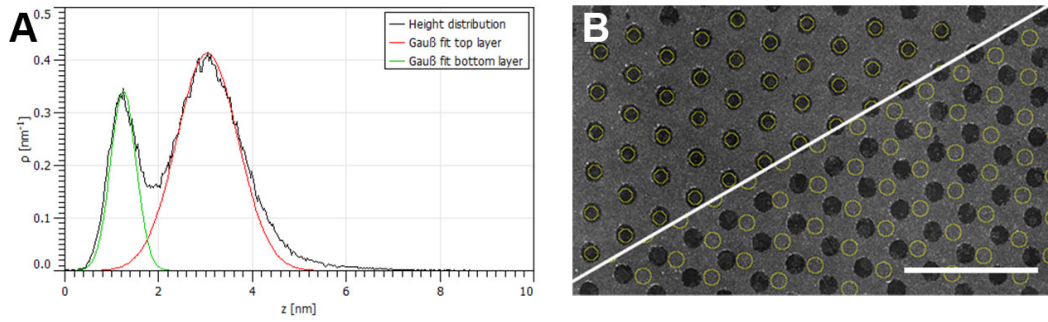


Figure 10.3.: Characterization of printed proteins. (A) Two Gauß functions were fitted to the height distribution, representing the bottom (glass substrate) and the protein top. In this example of printed BSA, the peaks are clearly distinguishable and have a distance of 1.8 nm. (B) “OFF” regions were selected by defining repetitive circular features in the pattern image (upper left). The size of the selected features was smaller than the actual well features to avoid edge effects. “ON” regions were selected in a similar fashion (bottom right). A W300 BSA pattern image is shown, scale bar is 2 μm .

and further analyzed in ImageJ. Regular arrays were selected within the printed patterns (Figure 10.3B) corresponding to either regions with (“ON”) or without (“OFF”) stamp-surface contact. The mean grey values per pixel for each region, I_{ON} and I_{OFF} , were used to calculate the contrast C :

$$C = \frac{I_{ON} - I_{OFF}}{I_{ON}} \quad (10.3)$$

Background subtraction was performed by taking the signal of the glass coverslip not covered by protein as a reference. In AFM image analysis, care was taken to perform the background subtraction the same way in all images to make contrast data comparable. Still, the definition of the OFF-state has an huge impact on the contrast and is partly subjective due to the measurement technique. Thus contrast values are only intended as a means of relative comparison between samples and are also no absolute indicator of pattern quality.

10.4. Substrate preparation and comparing options for coating

Blank slides Consistent starting materials are the basis for reproducible experiments. Consequently, the cleaning of the glass slides was tested the very first. We checked the

slides out of the box, washed thoroughly with DIW, ethanol, or acetone and compared rinsing to ultrasonic bathing. We scanned the surface with AFM with a tip diameter of around 7 nm. The root mean square of the deviation R_{rms} (eq. 10.2) of the AFM images are measured to compare the results.

Although the slides out of the box looked clean to the eye, AFM images showed a lot of particles with a lateral size of around $0.5 - 5 \mu\text{m}$. Their height was in the range of a few nanometers and thus comparable to the proteins of interest and would decrease the contrast of nCP significantly without being recognized as obvious influence. Intense water rinsing did not influence the surface ($R_{rms} = 0.9 - 1.3 \text{ nm}$ before and after rinsing) but with ethanol, isopropanol, or acetone the particles could be removed ($R_{rms} = 0.2 - 0.3 \text{ nm}$). Samples are shown in Figure 10.4.

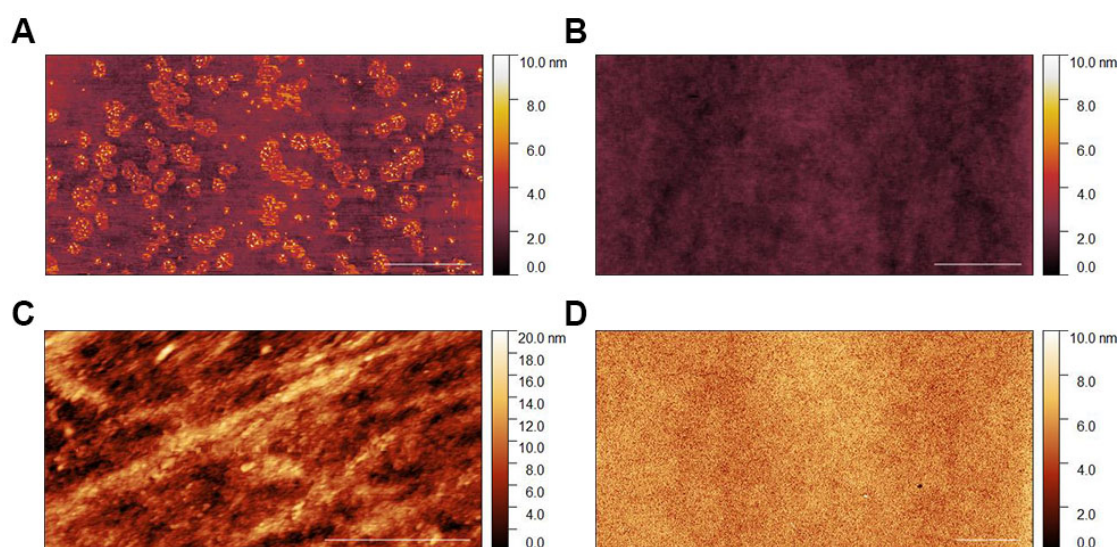


Figure 10.4.: (A) Glass slide out of the box with residues and a roughness of $R_{rms} = 1.1 \text{ nm}$. (B) Washing the slides thoroughly with ethanol or acetone removed this particles $R_{rms} = 0.3 \text{ nm}$. (C) Epoxy slides had the highest roughness $R_{rms} = 2.7 \text{ nm}$. (D) Biosensor coated slides had irregular holes with nanometer diameter but overall a good roughness of $R_{rms} = 0.9 \pm 0.1 \text{ nm}$. Scale bar is $3 \mu\text{m}$.

Protein adhesion promoter Different strategies for surface preparation for protein printing have been proposed: plasma cleaning [134, 135], epoxy functionalization [136], streptavidin-coating [137] as well as no further treatment of the glass substrate [74]. To achieve not only high imprint quality but also good long-term storability of the printed nanopatterns, we tested plasma activation, epoxide coating and functionalization of the glass coverslips with Anteos Biosensor coating, a polymer metal ion coating.

At least six nano contact prints were performed with W300/600 high-modulus X-PDMS stamps on the three chosen coating strategies on glass slides. The coated substrates were

10. Nanocontact printing with PTM-fabricated masters

measured with AFM and the qualities of the prints were analyzed as described in the previous chapter, normalized to the amount of experiments in Figure 10.5:

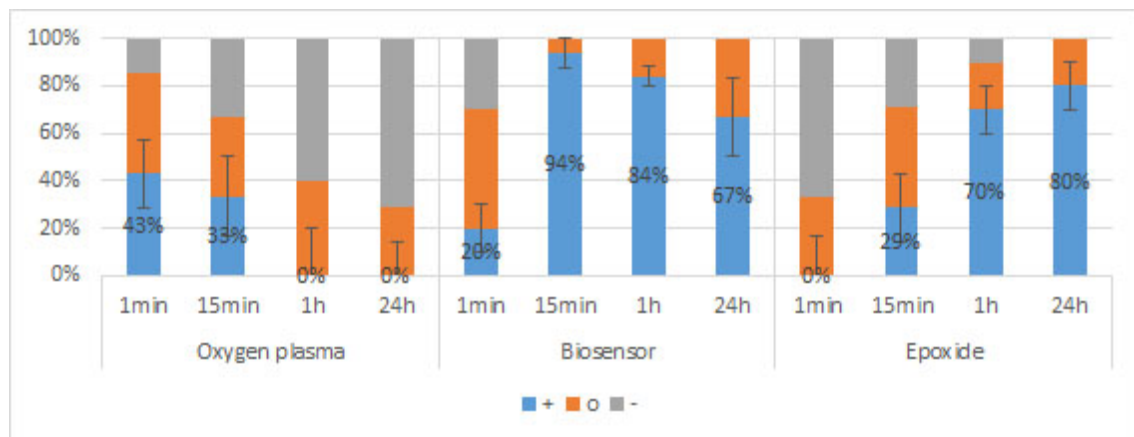


Figure 10.5.: Comparing X-PDMS print of FNT ($100 \frac{\mu\text{g}}{\text{mL}}$) with W300/600 on different coatings regarding the definition of chapter 10.3. At least six prints were performed for each coating. All experiments were performed at RT.

The roughness of the glass substrates was not influenced by the treatment with oxygen plasma, $R_{rms} = 0.2 - 0.3 \text{ nm}$. For short contact durations a good printing quality could be achieved, however, it was not reproducible and often not homogeneous. In addition, irreversible bonding between stamp and substrate occurred at the areas not covered by proteins if it was in contact for more than a few minutes and even stronger if the contact was hold for hours.

Epoxy coated slides had a roughness of $R_{rms} = 2.6 - 3.2 \text{ nm}$, much larger than a pure glass. Again, as with the above particles, this roughness affects the quality of the pressure when measured with AFM, since it inevitably affects the FWHM of the two curves in the height histogram. The best results, with a success rate of 80%, were only achieved after 24 h continuous contact.

Biosensor coated slides had a slightly increased roughness $R_{rms} = 0.4 - 0.5 \text{ nm}$. In addition, the best results could already be generated after 15 min. Unusually, the quality dropped again with increasing time. This was the case in most experiments, as more "OFF" regions were covered by proteins as contact duration increased.

Plasma-activated surfaces are functionalized with -OH groups and provide instant binding upon contact, but the silicone stamp can also covalently bond to the silicon dioxide surface. Biosensor coated surfaces are also charged, but without the option to bond to glass. Covalent attachment to epoxide requires opening of the epoxide ring, which can react in a slower time than direct adhesion to charged surfaces. The compliant contact was mandatory for all techniques and we expect it to be made after a few minutes when only light pressure was applied. Higher pressure caused the nano-functions of the stamp to sag or collapse, while at the time of contact, air bubbles prevented homogeneous

contact over the entire area.

An increase in autofluorescence could not be recorded in any of the promoters used.

Washing stability While the pattern is defined by the nCP, all further steps (backfilling, biotinylated antibodies, cell adhesion) are carried out in aqueous solution. Therefore, the adhesion of proteins to the substrate must be stable enough to withstand contact with water. To check this, the sample quality was checked with AFM and then an incubation chamber was applied. Since the time between substrate preparation and cell experiments can take several days, the samples were stored in the refrigerator (4 °C) for one week. Subsequently, the incubation chambers were rinsed three times with DIW, carefully removed and the sample gently dried with nitrogen.

On pure and plasma-treated slides, the proteins were almost completely removed, the printed protein pattern was no longer detectable in any sample (6 samples of both variants). In contrast, slides coated with epoxy and biosensor showed no measurable pattern deformation (5 and 7 samples, respectively).

10.5. Geometrical limits of stamps with three different Young's moduli

The Young's modulus of a stamp determines which change in length is induced at a given stress. Stamps with a high modulus have a higher probability that pillars remain stable, no sagging occurs and wells are not squeezed together. Nevertheless, the increased crosslinking of the silicone polymer also alters the surface energy, which in turn can lead to disadvantages in protein adsorption or transfer to the substrate. Therefore, the silicone stamps were made so that three different Young's moduli were achieved. The limits of these nanoscale stamps were statistically determined by a series of experiments under constant conditions.

Contact printing was performed with three stamp variations: low- and high-modulus X-PDMS and MED-6019. FNT 100 $\frac{\mu\text{g}}{\text{mL}}$ was applied both for wells and pillars, the substrate was thoroughly cleaned and coated with Biosensor reagent. The prints were evaluated according to chapter 10.3, results of the smallest achievable features both for pillars and wells are shown in fig. 10.7 and all results are listed in table 10.4.

High-modulus X-PDMS stamps had overall the most successful prints. In detail, for stamps from X-PDMS, the success rate for P300 patterns was similar to that for the W300. In P80, however, the mean contrast was significantly reduced. 5 out of 6 pressure tests on BSA produced very poor contrast ($C < 0.1$) with P80 patterns, but one print was of high quality ($C = 0.75$). Interestingly, despite the difference in size to BSA, printing of P80 fibronectin samples gave similar results: 2 out of 9 impressions were of

10. Nanocontact printing with PTM-fabricated masters

high quality ($C > 0.75$), while the remainder could not be successfully printed. This heterogeneity in the performance of the P80 stamps can probably be attributed to the manual printing process. Although the stamps did not show permanent damage after use, it is conceivable that excessive pressure during printing results in a reversible collapse of the rather soft pillars, resulting in a loss of contrast in the printed pattern. This could possibly be avoided by controlling the pressure with a suitable tool.

With MED-6019, the pressure of wells was of comparable quality, while no single successful pressure could be performed with 80nm diameter pillars. The largest Pillars P500 / 1000 achieved a success rate of 100 %.

In contrast, with the smallest modulus used ($E = 5\text{MPa}$), no single pressure with a pillar structure was successful and even the well structures had a much lower probability of success (33-72 %). This often came about because of the printing being successful only locally in certain areas. These areas had a ring-like shape, but with different radii between a few microns and a few millimeters. A faulty stamp production due to an incomplete imprint could be excluded by AFM and SEM images. Even with a used, cleaned stamp no quality change could be found which would explain the ring-shaped pattern.

To ensure that this reduction is actually related to the modulus of the stamp, the contact behavior of these stamps was investigated. For this purpose, a stamp without proteins was brought into contact with an uncoated slide while its adhesion was monitored by reflection interference contrast microscopy (RICM). RICM is an optical microscopy technique that uses polarized light to quantify the proximity of an object to a smooth surface, usually cells on glass. As the name implies, RICM is based on the contrast in the interference pattern of the reflected light. If the distance is on the order of the applied wavelength, the reflected rays interfere constructively or destructively depending on the distance. With monochromatic light, a higher signal intensity means a greater distance of the object from the substrate surface.

The wells were visible under light pressure, but the pillars appeared only in areas with gas bubbles or dirt (Figure 10.6). Lifting the stamp during filming showed that the pillars stood up again before losing contact with the substrate. The printing areas with a larger radius were therefore the marginal areas where the stamp lifted off of the substrate and so did not squeeze the pillars locally.

10.5. Geometrical limits of stamps with three different Young's moduli

Table 10.4.: List of experiments regarding the correlation of stamp material and feature limit size. All experiments were performed with $100 \frac{\mu\text{g}}{\text{mL}}$ FNT at RT on glass substrate coated with Biosensor. The characterization of the prints is defined in chapter 10.3. Success rate is the ratio of numbers of + to quantity. The Young's modulus of the materials is in brackets.

| Material | Master | Success Rate | Quantity | + | o | - |
|--------------------------------|-----------|--------------|----------|----|---|---|
| X-PDMS high-m. (~80 MPa) | W300/600 | 94 % | 16 | 15 | 1 | 0 |
| | W300/1000 | 100 % | 6 | 6 | 0 | 0 |
| | W500/1000 | 100 % | 6 | 6 | 0 | 0 |
| | W500/1000 | 83 % | 6 | 5 | 1 | 0 |
| | P80/600 | 21 % | 14 | 3 | 5 | 6 |
| | P80/1000 | 0 % | 8 | 0 | 3 | 5 |
| | P300/1000 | 88 % | 8 | 7 | 1 | 0 |
| | P500/1000 | 83 % | 6 | 5 | 0 | 1 |
| X-PDMS low-m. (~5 MPa) | W300/600 | 33 % | 9 | 3 | 3 | 3 |
| | W300/1000 | 67 % | 7 | 4 | 2 | 1 |
| | W500/1000 | 72 % | 7 | 5 | 2 | 0 |
| | W500/1000 | 72 % | 7 | 5 | 2 | 0 |
| | P80/600 | 0 % | 7 | 0 | 0 | 7 |
| | P80/1000 | 0 % | 7 | 0 | 0 | 7 |
| | P300/1000 | 0 % | 7 | 0 | 0 | 7 |
| | P500/1000 | 0 % | 7 | 0 | 0 | 7 |
| MED-6019 (~8 MPa) | W300/600 | 83 % | 6 | 5 | 1 | 0 |
| | W300/1000 | 100 % | 6 | 6 | 0 | 0 |
| | W500/1000 | 83 % | 6 | 5 | 1 | 0 |
| | W500/1000 | 83 % | 6 | 5 | 1 | 1 |
| | P80/600 | 0 % | 6 | 0 | 0 | 6 |
| | P80/1000 | 0 % | 6 | 0 | 0 | 6 |
| | P300/1000 | 67 % | 6 | 4 | 2 | 0 |
| | P500/1000 | 100 % | 6 | 6 | 0 | 0 |

10. Nanocontact printing with PTM-fabricated masters

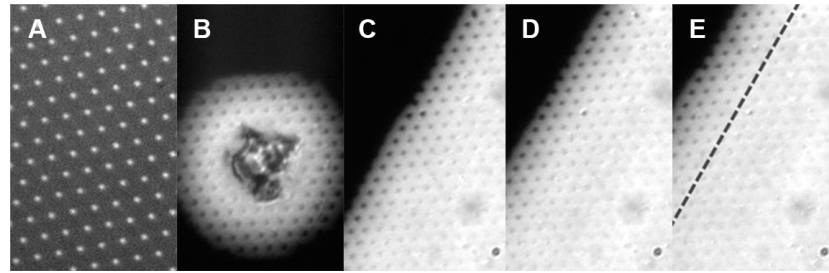


Figure 10.6.: RICM images of a stamp with a modulus $E \approx 5$ MPa in contact with an untreated glass slide. (A) Wells of all feature sizes were clearly visible but pillars showed mostly a full-faced contact. Pillars could only be found in areas around defects like trapped air or particles (B) or at the edge of the contact zone (C). (D-E) show the same position while manually lifting the stamp. The dashed line in (E) illustrates the position of the contact edge at (C).

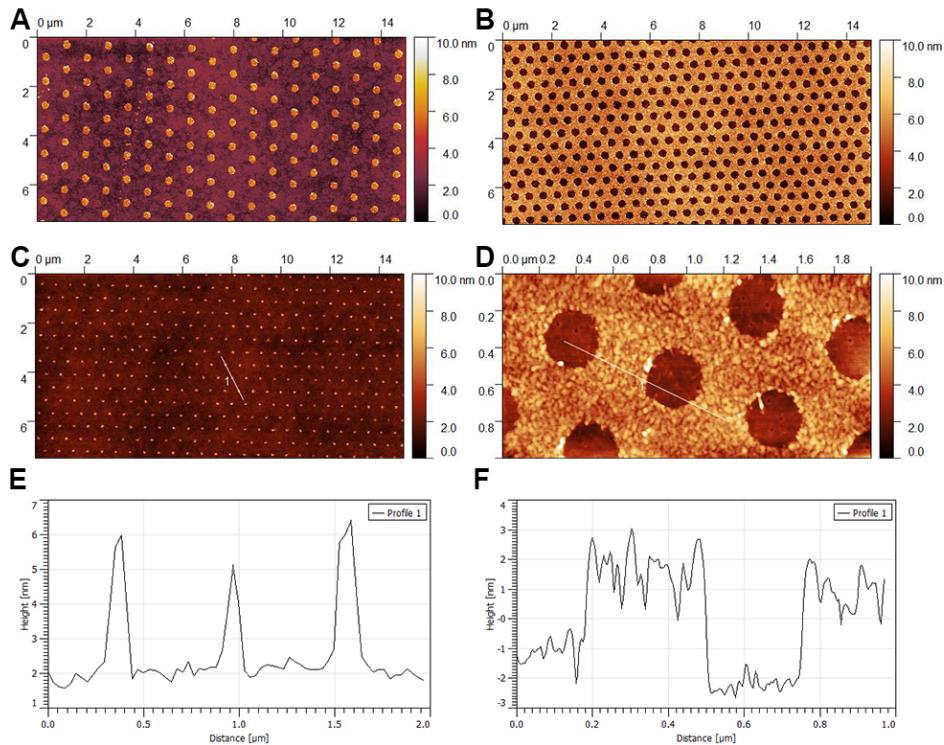


Figure 10.7.: AFM tapping mode topology images of minimal achieved geometries of the nickel masters. For MED-6019, the limit was reached with (A) P300/1000 and (B) W300/600. With high-modulus X-PDMS all features which were fabricated by PTM could be printed, although (C) P80/600 with a success rate of around 20 %, (D) W300/600 with 94 %. The line profiles (E,F) are for the images directly above.

10.6. Influence of protein concentration for nCP

The objective for this experiment was to optimize the parameter for the protein coating of the stamps. To get reasonable limits for concentration tests, the following estimation was proposed:

The number of proteins in bulk N gets reduced by the number of adsorbed proteins on the stamp n , the remaining proteins in the bulk are N' :

$$N' = N - n \qquad \frac{n}{N} = 1 - \frac{N'}{N} \qquad (10.4)$$

A ratio $n/N \rightarrow 0$ indicates that the amount of proteins in the bulk was not influenced by the adsorption. The ratio $n/N \rightarrow 1$ means that all proteins from the bulk were at the stamp surface. Now assuming a circular area with a radius R is fully covered by a monolayer of proteins while the protein solution forms a hemisphere. This is a lower estimate since untreated silicone stamps are hydrophobic, meaning more volume on less contact area. Both n and N can be calculated if the area a covered by one adsorbed protein, molecular mass m of one protein and the mass of all proteins in bulk M are available:

$$n = \frac{\pi R^2}{a} \qquad N = \frac{M}{m} = \frac{2}{3} \pi R^3 \frac{c}{m} \qquad (10.5)$$

With this, the ratio of adsorbed proteins to available proteins can be calculated, assuming the protein occupies a disk area with the radius r :

$$\frac{n}{N} = \frac{R^2}{r^2} \frac{m}{M} = \frac{3}{2\pi} \frac{m}{Rr^2c} \qquad (10.6)$$

Having the initial idea in mind we can now see the ratio is an hyperbola for the concentration and we can define a minimum concentration c_{min} :

$$\frac{n}{N} \propto c^{-1} \qquad \frac{n}{N} \rightarrow 1 \text{ at } c_{min} \qquad (10.7)$$

Proteins tend to spread if they adsorb on a surface, especially for low concentrations. For a rough estimate the Stokes radius can be applied although it includes a hydro-sphere and is therefore typically larger than the pure protein polymer. With a typical

10. Nanocontact printing with PTM-fabricated masters

drop radius of $R = 2\text{mm}$, for both BSA and SAV the minimum concentration is around $c_{min} \approx 0.1 \frac{\mu\text{g}}{\text{mL}}$, for FNT it is $c_{min} \approx 1 \frac{\mu\text{g}}{\text{mL}}$. Although it is a lower estimation, the complete transfer of the proteins in the solution to the stamp is very unlikely. The applied concentration should therefore be significantly higher than calculated values and we tested protein concentration of FNT in DIW between 1, 10, 100 and 1000 $\frac{\mu\text{g}}{\text{mL}}$.

X-PDMS stamps were covered with 50 μL of the protein solution and washed after 15 min with DIW. The substrates were prepared with Biosensor reagent, printing duration constant at 15 min. Prints were in principle possible for all concentrations, however, the height of proteins decreased dramatically while lowering the concentration. For higher concentrations, the coating was thicker and more homogeneous. A surface with a roughness below $R = 0.5\text{nm}$ was reached for 100 $\frac{\mu\text{g}}{\text{mL}}$, the protein curve had a FWHM of $2.1 \pm 0.2\text{nm}$. Cracks in the layer appeared for 10 $\frac{\mu\text{g}}{\text{mL}}$, the FWHM increased to $3.2 \pm 0.8\text{nm}$. For 1 $\frac{\mu\text{g}}{\text{mL}}$ the patterns was still visible for human eye but did not succeed according to the applied characterization methods. The distribution of the glass surface and for the protein merged into one curve with a FWHM of $1.4 \pm 0.2\text{nm}$. Representative AFM images and height distributions are shown in fig. 10.8. The average values of the heights are plotted in fig. 10.9.

The measured height of FNT was significantly smaller than the Stokes radius in literature [60, 138, 61]. For experiments with 1000 $\frac{\mu\text{g}}{\text{mL}}$, we measured a total height of $5.5 \pm 0.2\text{nm}$, while the Stokes radius should be around 8 nm. However, the definition of the hydrodynamic radius includes dragged molecules which impact the diffusion coefficient and get widely ignored by the tapping mode of AFM. In addition, the adsorption of the protein leads to stretching, limited mainly by intramolecular forces [139]. This also explains the variation of height of FNT depending on concentration. If more space is available only intramolecular forces hinder further expansion, resulting in cracks in the patterns of 1 and 10 $\frac{\mu\text{g}}{\text{mL}}$. These correlations also apply for the spherical proteins BSA and SAV but to a lesser degree.

According to the estimation, no height difference should be measurable if a typical protein solution were reused several times, since the ratio for BSA ($100 \frac{\mu\text{g}}{\text{mL}}$) $n/N \approx 2 \cdot 10^{-2}$. Several experiments were performed to test the practicality of this estimate. Several stamps were coated with BSA and after 15 min the protein solution was pipetted. The stamp was printed on biosensor reagent, then washed thoroughly with acetone, ethanol and DIW, and then the protein solution was reapplied directly from the pipette. Six iterations were performed and the protein level determined (Figure 10.9). The linear fit shows a small slope, but all data points lie within the error bars. Granted, this is of little relevance to standard BSA or FNT, but could become more important if expensive, modified proteins are used.

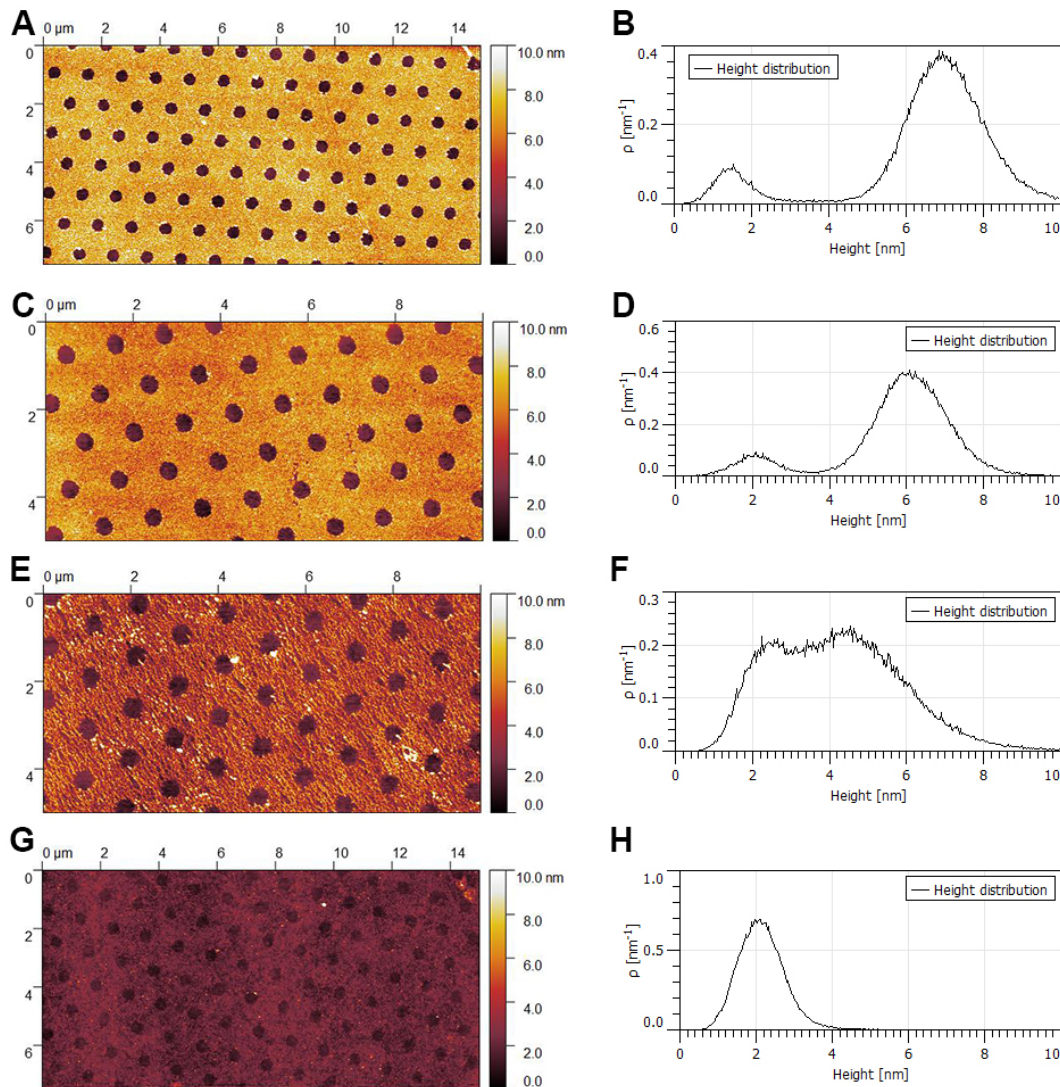


Figure 10.8.: Variations in protein concentration of FNT. (A,C,E,G) show AFM images, (B,D,F,H) their corresponding height distribution. Measuring the average height as described in the characterization chapter, (H) is not resolvable. (A,B) 1000 μ g/ml; 5.3 nm, (C,D) 100 μ g/ml 4.2 nm, (E,F) 10 μ g/ml 1.9 nm, (G,H) 1 μ g/ml, not resolvable.

10. Nanocontact printing with PTM-fabricated masters

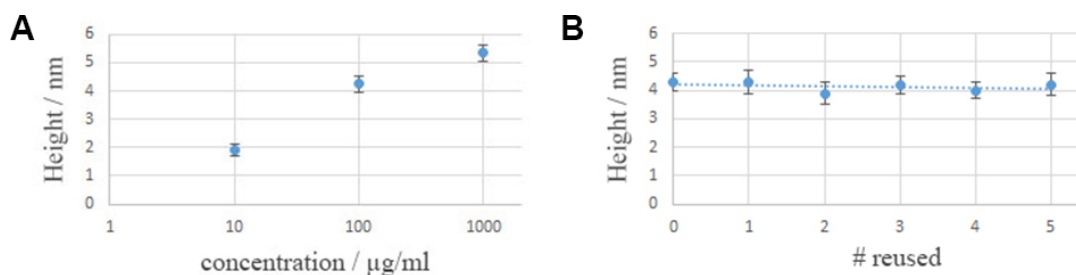


Figure 10.9.: (A) The height of adsorbed FNT proteins depends on the concentration of the solution while coating. (B) For at least five applications, the same protein solution can be applied without loss in height.

10.7. Washing, reusability and large area prints

Washing One of the benefits of PDMS stamps for mCP is that they can be reused many times before defects become visible. However, it was unclear whether this also applies to X-PDMS stamps with nanostructures, as these can be a lot more sensitive. Therefore, FNT ($100 \frac{\mu\text{g}}{\text{mL}}$, 15 min) with W300/600 stamp was printed on biosensor coated substrates. When a drop of DIW was applied to the stamps, it was found that the protein-coated portion was slightly hydrophilic while the silicone surface otherwise remained hydrophobic. When the stamp was pressed onto another coated slide without re-adsorption of proteins and a drop was applied again, no hydrophilic area was left. This led to the assumption that at least no cohesive protein layer covered the stamp surface anymore. Since a monolayer of the proteins was confirmed on the basis of the height measurements on the substrate, it can be assumed that a monolayer is also adsorbed on the X-PDMS and completely transferred during the pressure. Indeed, AFM samples of substrates printed with a used stamp did not show any transferred proteins. These substrate looked identical after printing to a fresh biosensor coated surface with $R_{rms} = 0.5 \text{ nm}$.

If conformal contact has been prevented, for example, by the inclusion of air bubbles or particles, it could happen that proteins stick to the stamp. As an experiment, a stamp was coated with FNT as above but then tried to wash off the proteins before the nCP. Neither acetone, isopropanol, ethanol nor DIW reliably removed all proteins, but dust particles could be removed from the silicone with the organic solutions. Only when the stamps were bathed in acetone and DIW with ultrasonic for 1 min, the proteins could be removed successfully.

To see if this cleaning option could have an impact on the stamp after repeated use, the stamps were bathed with ultrasonic for 5 min, 10 min and 15 min. Between each bath, nCPs were performed and checked with AFM. The pattern showed defects on the order of 50 – 200 nm after even 5 min. Prolonged application increased the number and size of nanodefects (Figure 10.10). Although these protein patterns were still well defined in terms of height distribution, they would fail the quality test because the pattern was

clearly not homogeneous to the eye. The contrast dropped to 0.42 ± 0.12 .

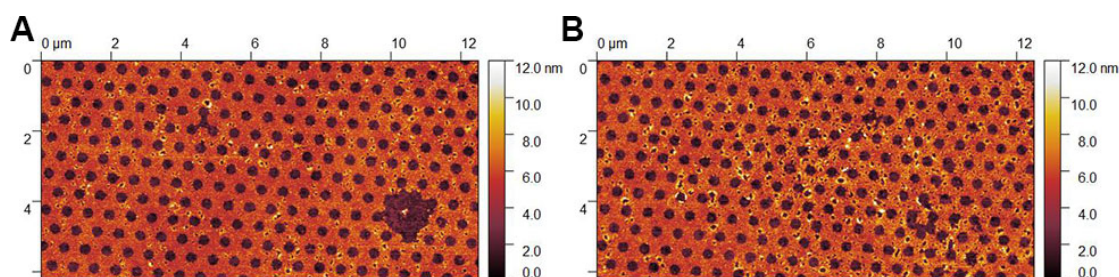


Figure 10.10.: Stamp defects by ultra-sonic bath. (A) Microdefects and some delaminations of X-PDMS from the softer backplane can be seen after 10 min. (B) After 15 min the amount of the nanodefected increased.

Reusability Finally, several stamps were applied with the same type of protein for around thirty times, two for even more than fifty times with the mentioned washing steps in between the printings. The nanopatterns showed no detectable defects, the contrast did not deteriorate. AFM images of the stamp also showed no defects such as accumulated proteins or nanodefecteds as occurred after ultrasonic baths.

Large area nCP In contact printing, protein deposition does not depend on the coherence of a light source or other long-range effects limiting the size of the patterned area. The size limit for a patterned area is thus set, in principle, by the size of the master. Even with stamps produced from 6inch masters, pattern quality was generally high over the whole printed area. Measured on several times in three different regions (near the center, near the edge and in between) the overall contrast was 0.79 ± 0.02 . However, in a manual printing process, a practical limitation is set by the dexterity of the experimenter, since the likelihood of trapping air bubbles between stamp and substrate increases with the stamp size.

10.8. Incubation of SAV on FNT pattern

After printing FNT wells, an incubation chamber was adhered to the printed pattern. Five samples were backfilled with a SAV solution $100 \frac{\mu\text{g}}{\text{mL}}$ for 15 min immediately, five after one week. In application experiments, the chamber would not be removed, but for further analysis the incubation chamber was rinsed with DIW to avoid salt crystals and then carefully removed with a razor blade. The substrate was dried in a stream of nitrogen and examined with AFM.

AFM images showed a homogeneous topology with small differences in height of less than 2 nm between SAV disks and the FNT grid. By the dependence of the protein level

10. Nanocontact printing with PTM-fabricated masters

on the concentration used, the difference between FNT and SAV could be adjusted so that either the SAV or the FNT protrude topologically (Figure 10.11).

Phase images also showed a clear difference between the two proteins, regardless of the topology. Substitution of FNT by SAV during incubation is thus not excluded but at least unlikely.

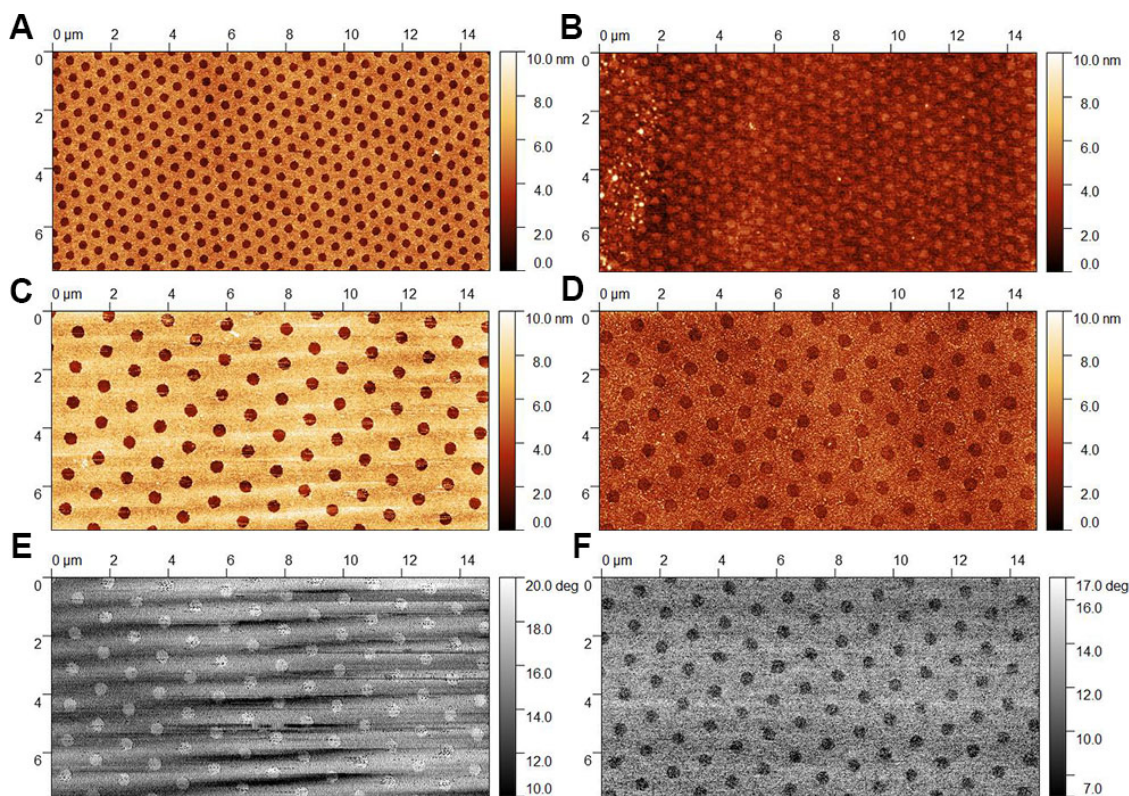


Figure 10.11.: AFM images of printed FNT on Biosensor coating, before and after incubation with SAV. (A) If the FNT layer has a height of around 3 nm, (B) the backfilled SAV proteins protrude. (C) If the FNT layer is around 4.5 nm, (D) SAV can match the height and can hardly be detected with topology images. However, looking at the phase images of pure FNT and after backfilling (E,F, respectively), the incubated SAV proteins can be clearly distinguished from the FNT pattern. Measurements for images (C-F) were performed with the same cantilever.

10.9. Qualitative assessment with TIRFM and super-resolution microscopy

TIRFM We prepared W300/1000 and W300/600 with FNT ($100 \frac{\mu\text{g}}{\text{mL}}$) on Biosensor coated slides and incubated in sequence with SAV and biotinylated anti-human-CD4

antibodies (30 min). After washing and incubation with HeLa-cd4-mclovers cells (1 h), the redistribution of the membrane protein CD4 according to the printed nanopattern was monitored. The HeLa cells were genetically modified to express CD4 which is an important membrane protein of T cells. Also, the fluorophore mclover was genetically attached to the membrane protein. This GFP-derivate is suitable for TIRFM and one of the strongest fluorophores of all GFP or RFP derivates [140].

HeLa HA-mGFP cells were used for testing measurements since they are adherent cells, opposite to T cells which are suspension cells. In addition, HeLa cell line is easy to use and culture because they are not prone to infections, the growth rate is relatively high, and the transfection of HeLa with recombinant DNA is feasible.

With epifluorescence microscopy and not focusing at the glass-cell-interface, a relatively homogeneous distribution of the labeled CD4 could be observed (fig. 10.12A). Moving the focus to the region of interest near the glass surface, we could see that the CD4 membrane proteins rearranged according the printed protein nanopattern on the substrate (fig. 10.12B). Although background noise was still present, it was decreased significantly with switching from epi-illumination to TIR (fig. 10.12C-D). We expect two major causes for background noise. If the pattern density was lower than the density of the fluorescing molecules the pattern would be saturated, leaving the remaining fluorophores in regions which should be blocked. The second major cause were activated fluorophores far away of the glass. By the application of TIRFM which illuminates around 200 nm near the glass surface, a cell thickness of at least several micrometers and fluorophores only attached to membrane proteins, this second cause was strongly reduced. However, the density ratios of capturing areas and fluorophores in the membrane needed to be carefully adjusted to avoid undersaturation with a weak signal intensity or oversaturation with higher noise. We expect that in our case more proteins were expressed than could be captured with the antibodies.

Once the cells were attached they did not move again in the timescale of at least 1 h. This indicates that neither the antibody-SAV binding nor the SAV fixed to the Biosensor coating could be detached by cell forces. At this stage, we cannot estimate the influence of the FNT-pattern which supposedly helped to stabilize and fix the cells and to keep the membrane attached to the glass surface.

We recognized that the fluorescing dots seemed larger than the width of the wells measured with AFM. This can be explained by the size of the point-spread-function which increases the diameter of the patterns to a size of 500 nm which corresponds quite well to the visible TIRFM pattern. Thereby the W300/600 pattern was hardly resolvable with TIRFM (fig. 10.12E,F), having an effective pitch of 100 nm.

dSTORM New samples of W300/600 FNT-patterns were studied with STORM. The preparation was identical as described for TIRFM but only fluorescing antibodies were incubated and no cells added. In contrast to TIRFM, with STORM the pattern were

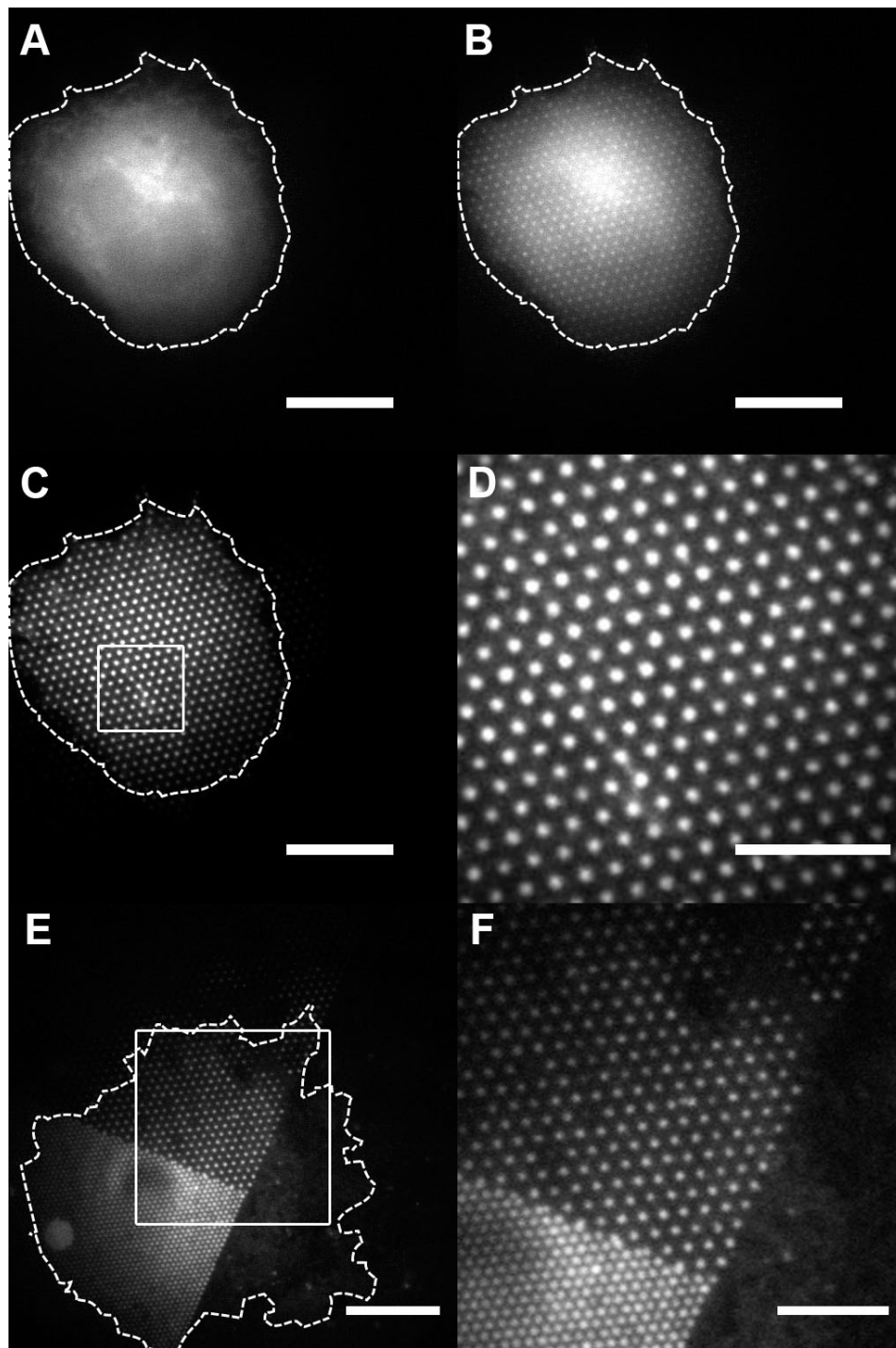


Figure 10.12.: TIRFM image of HeLa-cd4-mclover cells. **(A-D)** One is attached to W300/1000 patterns, **(E-F)** a second cell overlapped to W300/600. Epifluorescence microscopy images in the cell **(A)** and at the membrane **(B)** illustrate the huge advantage of TIRFM **(C)** for studying membrane proteins. **(D,F)** are the magnification of **(C,E)**, respectively. The dashed line outlines the HeLa cell, the straight rectangle the magnified region. Scale bar **(A-C,E)** 10 μm , **(D,F)** 5 μm .

clearly resolvable and had a better background to noise ratio than the images with cells (fig. 10.13). This supports the theory of oversaturation with fluorophores.

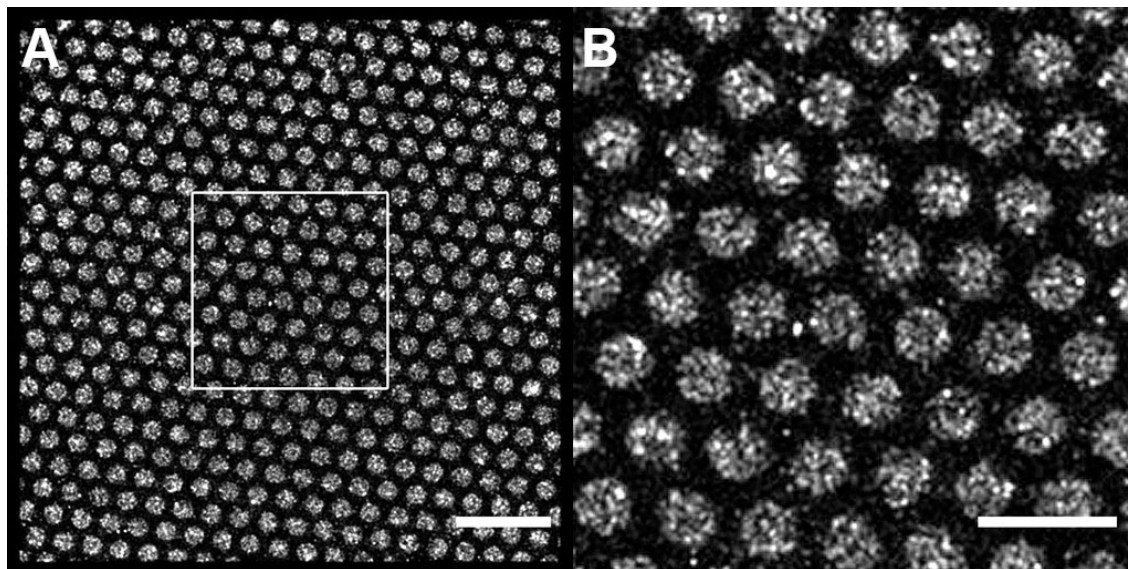


Figure 10.13.: STORM images of FNT W300/600 patterns, (A) overview and (B) zoomed-in. Opposite to TIRFM, with STORM the pattern was clearly resolvable. This image was measured with biotinylated, fluorescing antibodies without cells. Scale bar is (A) 2 μm , (B) 1 μm .

Compared to the very homogeneous looking AFM images, brightness heterogeneities in the wells could be detected with this super-resolution technique. Several causes can contribute to this result such as the size and binding kinetics of the antibodies, denaturated fluorophores, and detaching of SAV. Due to the timescale of STORM, stage-drift may also be taken into account. This misinterpretation can be partly eliminated by sophisticated algorithm but would require additional experiments and carefully adjustment of the STORM-parameters including the adaption of the redox-buffer. One of the intrinsic problems of STORM could not be ruled out. That is, that one fluorophore may be counted several times, each time with a position accuracy of 10 – 50 nm. Thus, the reconstructed final image may present higher local brightness which gets interpreted as several activated fluorophores but in fact came only from one molecule. However, the main reason may be that the sample had to be bleached heavily for the imaging, thereby destroying many fluorophores. This is especially true for high amounts of fluorophores which we have in the dense patterns. Thus, for the smallest feature sizes of this thesis another super-resolution technique was applied.

10.10. Discussion

The goal of the experiments with the PTM masters was to explore the limitations of nCP with high-modulus silicones and to find conditions that could enable a nCP with a period under 200 nm considering the set requirements. In principle, two different strategies can be used to prepare nanoscale biofunctional streptavidin discs: a) printing SAV with a pillar profile stamp, followed by filling with a protein for surface passivation, or b) printing a background protein and filling with SAV. By mastering with PTM, both variants could be examined for their applicability in the nanoscale.

It showed that the silicone with the highest modulus of $E = 80$ MPa had the highest success rate overall. At $E = 8$ MPa, well-structured printing was of nearly comparable quality, while at $E = 5$ MPa, only 33% of the smallest well-structure attempts were successful. The printings with pillar stamps were of lower success rate for all stamps. The high modulus X-PDMS stamp was the only one capable of printing with pillars of 80 nm in diameter, but only with a success rate of 21% and even then only up to a period of 600 nm. At 1000 nm period not a single successful print could be generated. Since these results were independent of the proteins used, this is probably not only a consequence of the modulus, but also of manual printing. No expensive equipment is needed either for the production of these stamps or for printing. Small impurities of the stamp have also no long-range influence, so this technique is well suited for laboratory use.

The protein concentration played a minor role in influencing print quality. A threshold value must be exceeded in the concentration, which can be estimated among other things by the protein size, then a dense and homogeneous protein layer was reproducibly possible. At least for large, flexible proteins such as fibronectin, there was also the option to adjust the thickness of the protein layer between 1.9 nm and 5.3 nm solely by the protein concentration.

The coating with Biosensor solution was superior to the alternatives. The surface was only slightly rougher ($R_{rms} < 0.5$) than cleaned or plasma-treated glass ($R_{rms} < 0.3$), while the epoxy coating already had structures with a height in the nanometer scale ($R_{rms} < 3.2$). However, only the patterns on Biosensor and epoxy coating survived the contact with water without a significant loss of quality. In comparison between these two reproducible good results could be achieved with Biosensor coating already with a contact duration of stamp and substrate of 15 min, with epoxy the best results were achieved after 24 h. Although transfer for the electrostatic coatings should be immediate, nCP is essentially a plate-to-plate process, so air bubbles can easily be trapped. However, the silicone stamps are permeable to gas, which was probably the reason that only after a few minutes a complete conformal contact was guaranteed. Epoxide binding required significantly longer time periods to ensure stable protein transfer. It may be that the covalent bonding process takes much longer compared to electrostatic bonding. In addition, in contrast to the epoxide rings, the metal polymer ion coating does not

hydrolyze, so that the coating remains functional after at least two weeks. It is thus possible with the Biosensor coating to produce substrates with nanopatterns from blocking proteins and to add the anchor proteins shortly before the application, which offers the lowest probability of denaturing the anchors.

In contact printing, protein transfer does not depend on the coherence of a light source or other remote effects that could limit the size of the structured region. The size constraint for a structured area is, in principle, determined solely by the size of the master. The master made with PTM had a diameter of 6 inches, yet the pattern quality was generally high throughout the print area. As already mentioned, in a manual printing process there is a practical limitation by the dexterity of the experimenter since the likelihood of trapping air bubbles between stamp and substrate increases with the stamp size.

In addition, it has been shown that an X-PDMS stamp can be reused at least fifty times, with only a slight decrease in quality. However, ultrasonic baths can permanently damage the stamp, but also remove any residual protein from the surface, which could otherwise lead to cross-contamination.

The nanopatterning of membrane proteins could also be verified with TIRFM and dSTORM for W300/600 and W300/1000 patterns. However, dSTORM requires that the active fluorophores of each image could be resolved and localized which naturally gets more complicated with higher numbers of fluorophores. Images showed an inhomogeneous brightness distribution probably due to intrinsic limitations of the method such as the strong bleaching.

The success rates showed that high-modulus X-PDMS stamps with wells and Biosensor coating were the best choice for the nanoscale.

11. Nanocontact printing with a period of 140 nm

11.1. Master design and preparation of composite stamps

According to the results in previous chapters, printing from Wells was a promising way to achieve features under 100 nm. Since the limit of mastering possibilities with PTM had already been reached in-house, an external Master had to be acquired. Few techniques are available to create silicon masters with 50 – 80 nm wide pillars and a period of less than 200 nm. Electron beam lithography can achieve such patterns, but is quite costly, especially for large areas. On the other hand, the given lateral constraints are too small for most interference lithography techniques. However, Eulitha, Switzerland, invented and patented a technique called Phable for the cost-effective production of periodic nanostructures [141]. A 4-inch master could be acquired by Eulitha with 52 ± 3 nm wide pillars (measured on top of the pillars) with a period of 140 ± 2 nm and a depth of 100 nm (Figure 11.1 A). Since the stamp's feature sizes are defined not by the top diameter but by the wider bottom of the pillars, the pits of X-PDMS stamps had an average size of 78 ± 5 and a period of 140 ± 2 . The stamp was thus defined as W80/140.

This master was imprinted with MED-6019 and X-PDMS (cured for maximum modulus). In the protocol of X-PDMS, 3g for both X-PDMS and intermediate layer are suggested for a 6 inch wafer. For a 4 inch wafer, this would result in only 1,4g to cover the area, however, spincoating the reduced amount of the viscous pre-polymer resulted in incomplete coating. Thus, although the area of the Eulitha master was around half the size of the nickel master from PTM, the amount of X-PDMS reagents was kept the same. With this, both MED-6019 and X-PDMS stamps were both successfully fabricated with the protocol in chapter 10.2. The topology of the patterns were checked on a large scale with SEM for defects like pairing. Minor, local defects and dust particles were detectable but overall the stamps of MED-6019 and X-PDMS were of high quality (fig. 11.1B-D).

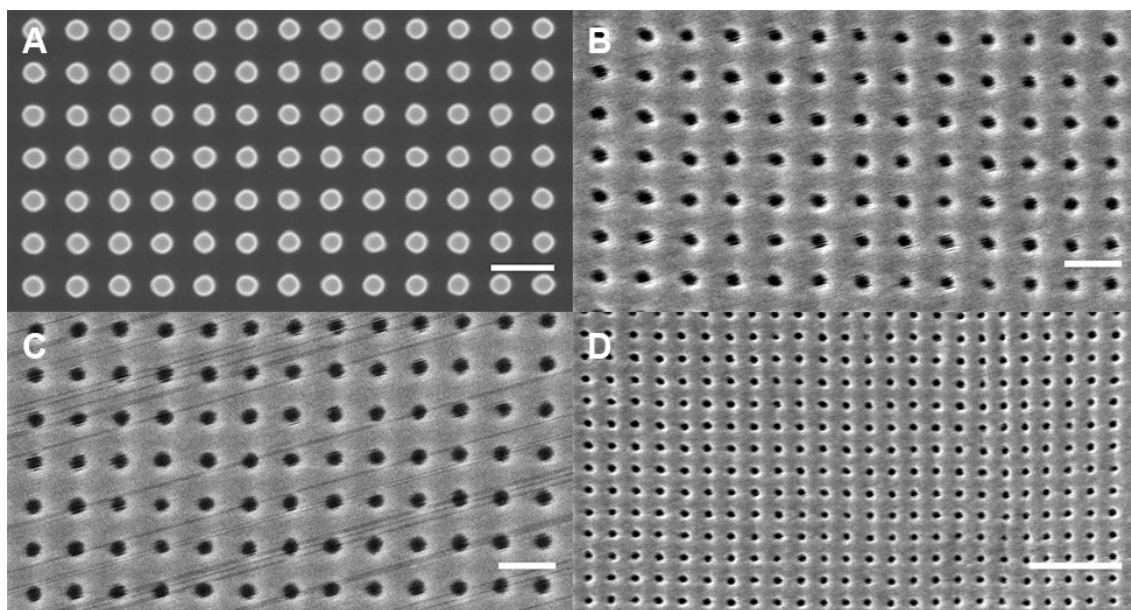


Figure 11.1.: (A) SEM image of silicon master with pillars for the W80/140 silicone stamps. Both (B) X-PDMS and (C) MED-6019 could be successfully imprinted with this master. (D) Although SEM is a destructive method, one half of the stamp was checked to ensure the quality of the stamps. The cushion distortion visible in the overview of the X-PDMS stamp in (D) appeared due to the high energy of our SEM. Image of master (A) with kind permission of Eulitha, Switzerland. Scale bars (A-C) 200 nm, (D) 500 nm.

11.2. Nanocontact printing of FNT with 80 nm wide wells

Following the print protocol developed in Chapter 10, FNT ($100 \frac{\mu\text{g}}{\text{mL}}$) was printed on Biosensor coatings using the new wells stamps. However, the substrate showed no well pattern, but a fully covered area with protein rings at the edge of the expected wells (Figure 11.2). Defective prints could be used to determine the height of the protein carpet at 4 nm, which is approximately equal to the level of FNT for the applied concentration. The rings themselves had a height of about 8 nm, so they correspond to a double layer FNT. The radius of the covered pits is 35 nm in the inside, from tip to tip it is 75 nm, which is close to the hole size of the stamp.

The results of the protein carpet were reminiscent of the experiments of nCP with stamps with too low a modulus of elasticity or too high pressure (see chapter 10.5). RICM measurements were not possible because the feature period was below the diffraction limit. Based on previous RICM experiments (Figure 10.6), it was expected that there could be a pressure windows that did not deform the stamp features. This can hardly be achieved with manual nCP, so the device introduced in Part III, which was developed for nanoimprint lithography, was used. It is a specially crafted NIL-to-disk-to-disk tool, which is discussed in detail in Chapter 14.2. To modify it for nCP, the stamp was placed on two slides so that it could hang over the ground like a bridge. A stack of soft PDMS (5 mm square, 2 mm thickness) was placed on top of the stamp in the middle. The bending of the foil pressed on the stack and brought the feature side of the stamp into contact with the substrate. The automatic release of the print causes a lifting due to the stiffer glass backplane. The pressure was varied from (10 – 50) kPa in steps of (10) kPa and between (40 – 50) kPa with steps of approximately (2) kPa. All variants, however, resulted in a protein carpet. So no successful nCP could be achieved.

Other potential parameters have been varied, such as printing on epoxycoated slides (24 h), but the result remained sobering. A reduction in the concentration to $10 \frac{\mu\text{g}}{\text{mL}}$, however, caused that no rings were present, but only the continuous protein layer. By further reducing to $1 \frac{\mu\text{g}}{\text{mL}}$, irregular wells became noticeable. However, as already shown in Chapter 10.6, the print quality was insufficient for concentrations far below $100 \frac{\mu\text{g}}{\text{mL}}$. Nevertheless, this was an indication that the protein itself could be the cause of these defects. In a compact conformation, the molecular dimensions of fibronectin are 9×16 nm [138], while the stretched molecule can reach lengths of up to 160 nm [60]. It is therefore possible that fibronectin partially covers the 80 nm wells, resulting in a loss of resolution. To verify this theory and work around the problem, a smaller, spherical protein was printed instead.

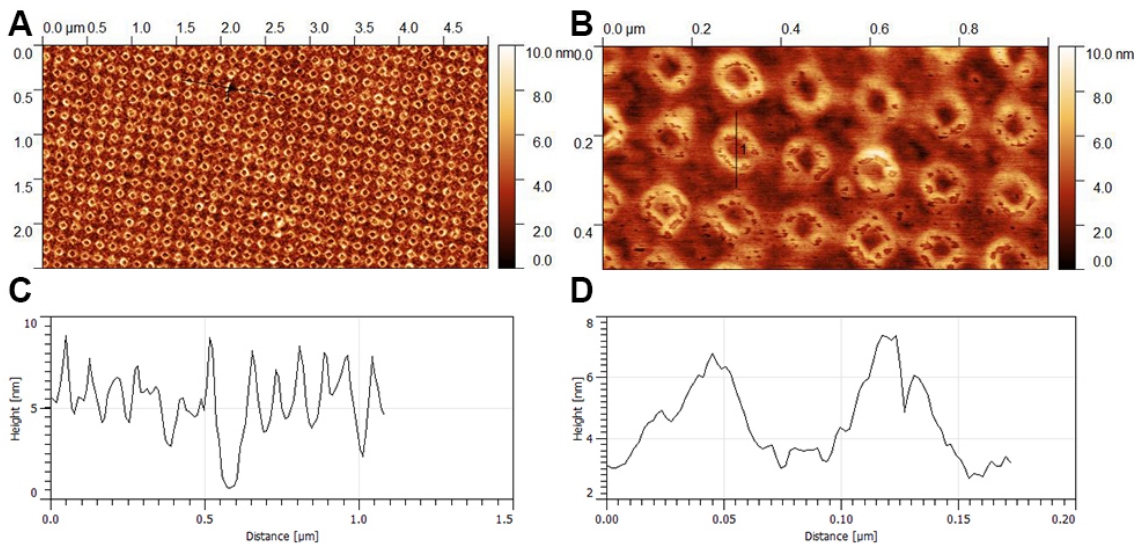


Figure 11.2.: AFM images of FNT rings on a carpet of FNT. (A) Overview and (B) detail with their line profiles (C,D). The inner diameter of the rings is around 35 nm, from peak-to-peak it is 75 nm. The well diameter on the applied stamps is around 80 nm.

11.3. Nanocontact printing of BSA with 80 nm wide wells

Fibronectin was chosen in the beginning as the blocking protein because the adhesion of the cell membrane is crucial for application experiments based on TIRFM. Different spatial distances, such as those caused by bending the membrane, would lead to data that could be misinterpreted. However, because FNT was not printable for W80/140, a smaller protein was tested. BSA is a spherical protein with a mass of about 15 % of a FNT.

Nanocontact pressures were measured with BSA ($500 \frac{\mu\text{g}}{\text{mL}}$) on Biosensor coated slides. This time, wells could be clearly seen (Figure 11.3). For comparison, experiments with W300, P80 and P300 were additionally performed (Table 11.1, Figure 11.4). The prints of W80/140 had a success rate of 67 % and a decent contrast 0.61 ± 0.14 , averaged over ten samples measured. Two samples were below 0.40, otherwise the quality would be comparable to W300/600.

The BSA height for the applied concentration was approximately 3 nm, which is only slightly smaller than the Stokes radius of 3.5 nm, and can again be determined by the definition of the hydrodynamic radius as well as by conformational changes [139]. Again, the prints were dense monolayers.

To consider the influence of the Young's modulus, 10 prints were also made with the

11. Nanocontact printing with a period of 140 nm

MED-6019 stamp, but the results showed a protein carpet with no recognizable wells ($C < 0.16$).

The next step was to check whether reuse of the stamps would decrease the imprint quality for these nanopatterns. Even after 50 prints of BSA with one stamp, however, the contrast of the W80/140 prints did only slightly deteriorate ($C = 0.58 \pm 0.07$).

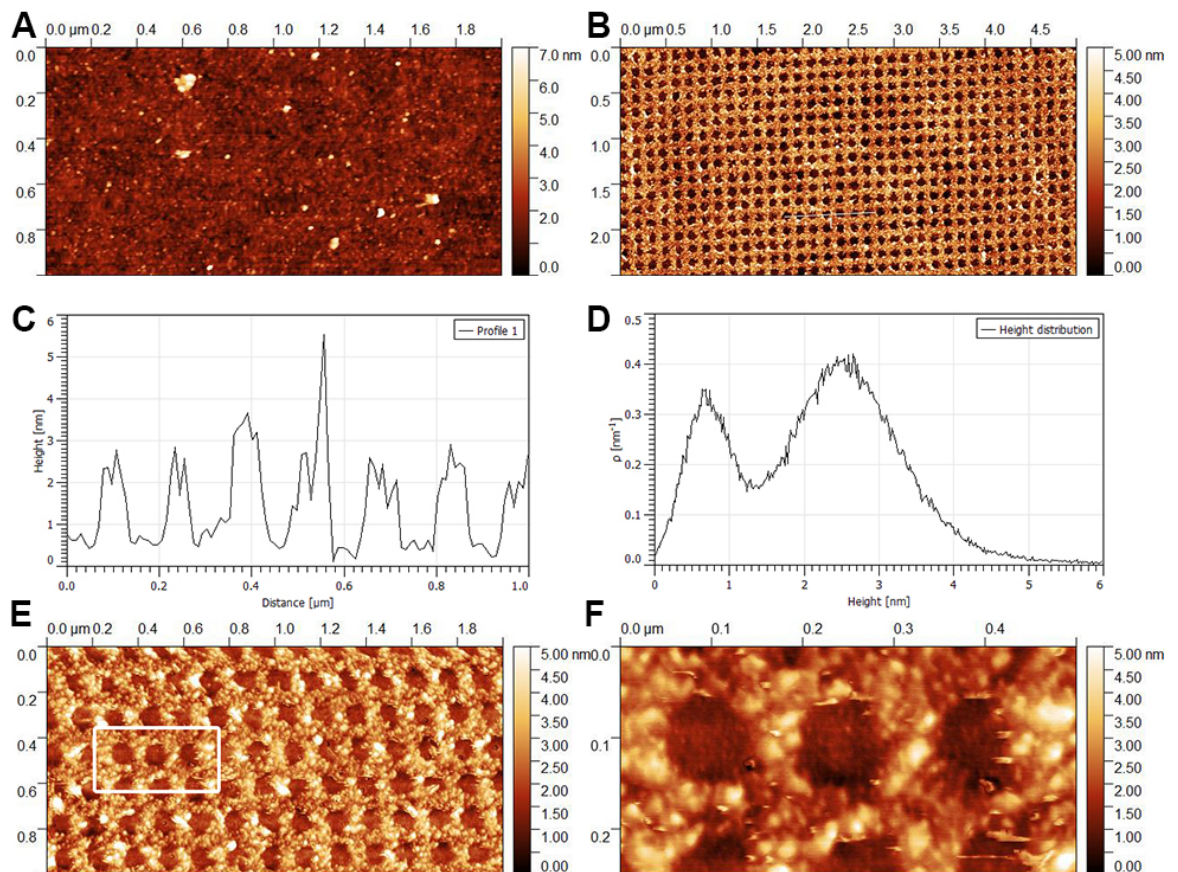


Figure 11.3.: AFM tapping mode topology images of W80/140 prints with BSA $500 \frac{\mu\text{g}}{\text{mL}}$ on Biosensor coating. (A) For the MED-6019 stamps, no protein nanopattern could be achieved. (B) With X-PDMS and BSA, the prints succeeded with a rate of 67%. (C) The line profile and the (D) height distribution of (B) illustrate the quality of the pattern. (E, F) After the samples were stored in the fridge at 4°C for 17 days, no diffusion of the proteins was detectable.

Table 11.1.: Quality assessment of protein nanopatterns. n indicates the number of imprint replicates. Mean contrast values \pm standard deviations are given.

| Stamp layout | Protein | C | n | Comments |
|--------------|---------|-----------------|----|---|
| W80/140 | BSA | 0.61 ± 0.14 | 10 | 2 samples with $C < 0.40$ |
| W300/600 | BSA | 0.78 ± 0.08 | 12 | |
| W300/600 | BSA | 0.79 ± 0.02 | 3 | 3 different ROIs within one 6inch imprint |
| W80/140 | BSA | 0.58 ± 0.07 | 3 | after 50 prints |
| W80/140 | BSA | 0.53 ± 0.03 | 3 | after 17 days at 4°C |
| W80/140 | FNT | 0.26 ± 0.11 | 9 | 0 samples with $C > 0.50$ |
| W300/600 | FNT | 0.67 ± 0.05 | 14 | |
| P80/600 | BSA | 0.13 ± 0.28 | 6 | 1 sample with $C > 0.75$ |
| P300/600 | BSA | 0.72 ± 0.02 | 7 | |
| P80/600 | FNT | 0.24 ± 0.34 | 9 | 2 samples with $C > 0.75$ |
| P300/600 | FNT | 0.78 ± 0.02 | 6 | |

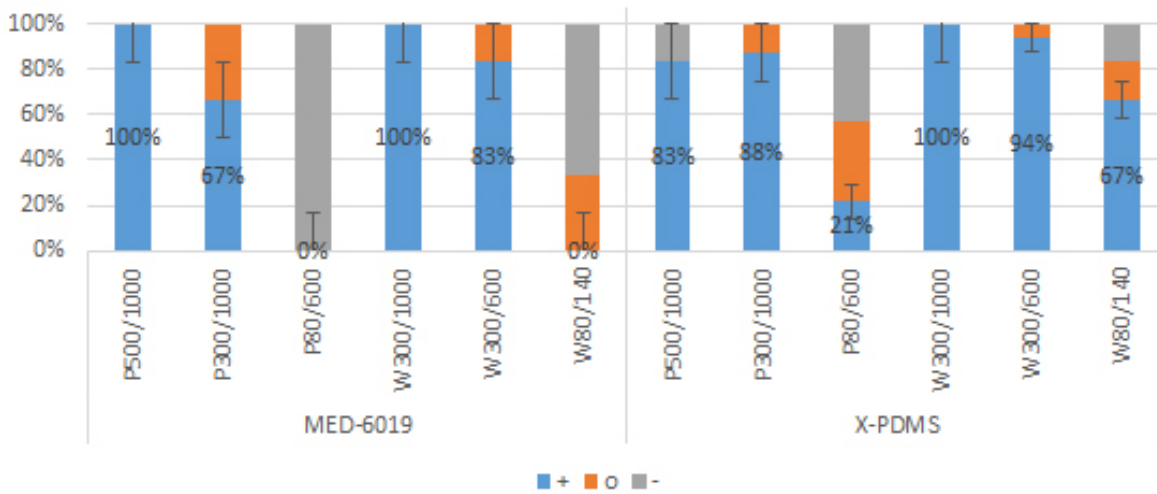


Figure 11.4.: Comparing the success rate of nCP with different feature sizes referring to table 10.3. All samples were performed on Biosensor coating with FNT except the W80/140 for which BSA was applied. At least six prints were performed for each feature side. The definition of the characterization can be found in chapter 10.3.

11.4. Shelf-life of nanopatterned BSA

Another important parameter is the storability of the printed patterns. Mostly, several days or weeks laid between nCP and further tests and the proteins could denatured or diffuse over time. It has already been shown that biosensor coating is stable over several weeks. However, avidity binding may have the option of allowing the molecules to rotate and may also be accompanied by diffusion, which over time should reduce the contrast of the pattern. After 17 days of storage at 4 °C, only a small decrease in pattern contrast ($C = 0.53 \pm 0.03$) was observed (Figure 11.3E,F), no major diffusion of the protein into the free spaces could be detected. Therefore, SAV can be added directly before the experiments to ensure a high functionality of the anchoring protein.

11.5. Imaging of antibody nanopatterns with STED

For STED microscopy, W80/140 and W300/600 BSA patterns were prepared and incubated with goat anti-rabbit IgG antibody conjugated with STAR RED (Abberior, Germany), diluted 1:50 in PBS to a final concentration of $20 \frac{\mu\text{g}}{\text{mL}}$. This fluorophore is recommended for STED, has excitation peaks at 635 nm and 650 nm and a depletion at 750 – 780 nm.

Although a W300/600 pattern was still resolvable with the confocal setup, the STED image showed more details regarding the positioning of the fluorophores. And as with STORM, a heterogeneous brightness was measured resulting in a contrast of $C = 0.77 \pm 0.03$. For W80/140 no patterns were visible with confocal microscopy but STED microscopy resolved the nanofeatures (Figure 11.5). For this pattern, the heterogeneity distributed over several disks, decreasing the contrast to $C = 0.55 \pm 0.04$. Both contrast calculations were averaged over three imprint replicates.

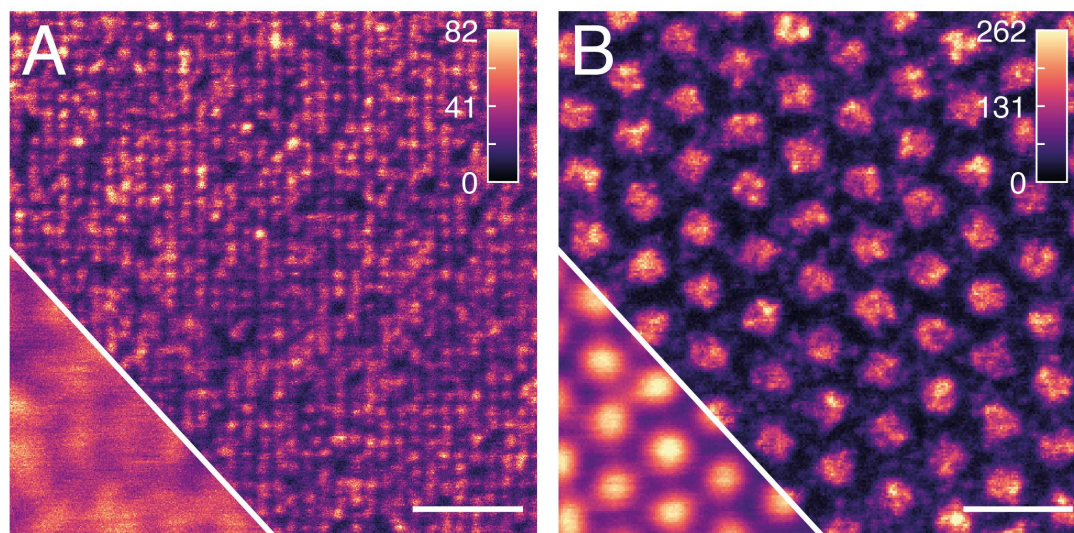


Figure 11.5.: Comparing confocal (**left lower corner**) and STED images of nanopatterns. **(A)** W80/140 patterns are visible with confocal microscopy but STED microscopy resolves the nanofeatures. **(B)** The W300/600 pattern was still resolvable with the confocal setup but the STED image showed far more details regarding the positioning of the fluorophores. Scale bar 1 μm

11.6. Discussion

For living cell applications on nanostructured surfaces, it is often beneficial to promote cell adhesion in the areas adjacent to functionalized disks. In microcontact printing, fibronectin has been widely used for this task, however, printing of FNT using the W80/140 stamp resulted in low-contrast patterns ($C = 0.21$) and often ring-like features. By comparison, the print quality achieved with the W300/600 stamp layout was of much better quality. It is suspected that the poor performance of fibronectin with the W80/140 stamps is most likely due to the size and properties of the fibronectin molecules. Large molecules such as fibronectin can alternatively be printed with pillars, but the success rate would drop significantly.

AFM images of the W80/140 printed BSA pattern resulted in successful prints with an average height of the printed protein of about 3 nm, which corresponds to a monolayer of BSA. These prints were reproducible at a median contrast of 0.61, which was lower than stamps with the W300 layout (0.78). There are several possible explanations for this: First, of the 10 imprints analyzed for the W80 layout, 2 had contrast values below 0.4. Such outliers were not observed in the W300 layout and may be a consequence of the manual printing process. Second, AFM image artifacts can affect contrast levels. For example, edge effects caused by the pulling of proteins into the "OFF" regions are more pronounced as the feature size decreases, resulting in an overestimation of the height in

11. Nanocontact printing with a period of 140 nm

"OFF" regions, resulting in an overall reduced contrast.

The samples could be stored for two weeks without pattern deformation, indicating that the avidity bond of the Biosensor coating is strong enough to prevent diffusion into the unprinted areas during this timescale. This was essential because the samples had to be transported from the production site to the high-resolution microscopes and usually several days had passed between the nanoprinting and the application.

In comparison to STORM, STED requires a more complex setup, but due to its principle of stimulation depletion, large amounts of fluorophores do not adversely affect the results but improve it. STED images of the patterns W80/140 and W300/600 could be recorded successfully with STED. In the W80/140 patterns, some spots appear to be poorly occupied with fluorophores, while some spots appear overly bright. The contrast values obtained for the W80/140 and W300/600 antibody samples were 0.52 and 0.77, respectively. Several factors can reduce the detected spot brightness and thus contrast in STED microscopy: low level of labeling of the antibodies, fluorophores lost by bleaching by either the excitation laser or the high intensity STED laser, fluorophores with a photon detection efficiency of less than 70 %. Considering the size of an antibody (10 nm x 15 nm), a maximum of about 20-30 antibodies can be accommodated in a well with a diameter of 80 nm. Due to the stochastic distribution of antibodies on the surface, it is possible that the number of fluorophores and thus detected photons differs considerably between individual antibody disks generated with the W80/140 stamps. With feature sizes of 300 nm, this leads to brightness heterogeneities within individual antibody disks, whereas in 80 nm features heterogeneities between the disks dominate.

12. Conclusion

It was possible to successfully produce substrates with nanopatterns of various sizes, the smallest samples produced had a period of 140 nm. The patterns were very homogeneous and stable for at least two weeks. The production of a fresh substrate took just 30 min, was very easy to reproduce and required no special equipment. This could be achieved by using high-modulus silicones as a stamp material and a polymer metal ion layer coating to support protein adhesion.

The combination of Young's modulus of the stamp and its geometry has a very big influence on the success rate. For 300 nm diameter wells, the modulus should be at least 8 MPa to reach > 80 % rate. For pillar structures, in addition to the diameter, the distance also plays an important role. A pressure with pillars with a diameter of 80 nm and a distance of 600 nm was only possible with stamps whose modulus was 80 MPa and even then only 1 of 4 succeeded. Successful prints with wells with 80 nm diameter could also be achieved only with these stamps, the success rate for 20 samples was $(80 \pm 5)\%$.

Also the choice of the protein is crucial. While wells with a diameter of 300 nm could still be printed with fibronectin, this protein occupied the wells with a diameter of 80 nm and thus prevented the successful printing. With bovine serum albumin, this difficulty did not exist, it was printable with all sizes in high density. However, cells usually do not adhere to BSA, which can cause problems with long distances between anchor disks.

Using living cells and TIRFM, the patterns could be seen up to a size of 300 nm and 600 nm period. The nanopatterns were stable over time even with the attached cells indicating that the adhesion of the proteins to the substrate was sufficiently strong. With STED, finally, the functionality of the smallest patterns with a period of 140 nm could be detected. With this technique, there is now an option to investigate the interaction behavior of membrane proteins up to a resolution of around 280 nm. Because a single well has a diameter of just 80 nm, it might be possible to capture only a few membrane proteins and study their interaction over a large area, not in the ensemble, but individually.

12. Conclusion

From all findings the following Best Practice Protocol was compiled:

Stamp preparation X-PDMS stamps can be reused many times especially if applied in series.

1. Cure X-PDMS layer for maximal Young's modulus. A curing at 70 °C for 10 days is recommended if features sub 100 nm are required.
2. Add a soft PDMS backplane of 2 – 3 mm. This is essential as compliant layer and may vary if the printing is not performed manually. Cure slowly at low temperature (≤ 70 °C) to prevent bending of the stamp.
3. Carefully lift off the stamp. Wash with acetone, ethanol, and DIW to remove remaining monomers and store dust-free.

Substrate preparation The success of nanocontact printing depends greatly on the preparation of the substrate.

1. Clean substrates. Rinse or bath in highly-pure organic solvent (ethanol, acetone) and then in DIW.
2. Mark the region of interest on the backside and cover it with Biosensor coating on the front. Protect the substrate from dust.
3. After 45 min, pipette the wet coating for reusing. Wash the substrate with DIW and dry in a nitrogen stream.
4. Dry and cool it can be stored for several weeks without losing functionality.

Nanocontact printing Great care should be taken for a clean environment, good light, and steady hands. The protein coating can be performed in parallel to the substrate coating.

1. Apply the protein solution. The concentration defines the height of the adsorbed proteins. For wells with a diameter above 300 nm, FNT ($100 - 1000 \frac{\mu\text{g}}{\text{mL}}$) is appropriate. Below, BSA ($10 - 1000 \frac{\mu\text{g}}{\text{mL}}$) is recommended as blocker protein.
2. After 15 min, wash the stamp with 1 ml DIW. Do not use PBS to prevent salt crystals on the surface. Dry with a nitrogen stream, blowing the remaining DIW carefully away from the region of interest.
3. Press the stamp by hand and with care on the marked area of the substrate. Be sure to avoid trapping air bubbles as good as possible. This can be achieved for

example by starting with the central area and then releasing slowly the slightly bended stamp.

4. Let the stamp rest for 15 min.
5. Remove the stamp and wash it with acetone, ethanol, and DIW.
6. Glue an incubation chamber on the printed area to ensure a protected and stable micro-environment for the proteins.

A substrate prepared like this may be stored dry and cool in a Unilever slide and sealed with parafilm for at least two weeks without deformation or diffusion on the nanoscale. However, it is important that the samples are adapted to room temperature before opening the seal.

Nanopatterning of membrane proteins The next steps depend strongly on the application and the used microscopy technique. With appropriate glass slides and the Biosensor coating, the samples are suitable for TIRFM, STORM, and STED.

1. Add SAV in solution $100 \frac{\mu\text{g}}{\text{mL}}$ to the incubation chamber. It should never dry to prevent salt crystallization or partial denaturation of the proteins.
2. Wash the chamber several times with PBS and add biotinylated antibodies. Do not let the solution dry.
3. Again, after 15 min, wash the chamber several times with PBS.
4. Finally cells can be added. After typically one hour, it is ensured that the cells adhered to the substrate and the target membrane proteins are captured at the regions of interest.



Die approbierte gedruckte Originalversion dieser Dissertation ist an der TU Wien Bibliothek verfügbar.
The approved original version of this doctoral thesis is available in print at TU Wien Bibliothek.

Part III.

Alternative approaches to nanopatterning of proteins

13. Nanocontact printing with hard POSS stamps

13.1. Introduction

As already described PDMS is the material of choice for μ CP [10]. The silicone with a Young's modulus of a few MPa ensures a conformal contact of the stamp and the substrate. In addition, silicone is well suited to adsorb proteins but also to transfer them to substrates with high surface energy [135]. In the nanometer range, however, PDMS has disadvantages such as the described sagging and pairing, which for the most part relates to the softness of the polymer. However, in hard stamps, the molecules do often not adhere to the surface but accumulate in the recessed areas of the stamp's nanostructures [142]. Polyhedral oligomeric silsesquioxane (POSS) materials can cure to a polymer whose functional groups can be modified to mitigate the disadvantages of other hard materials. The material has a Young's modulus in the range of GPa and should be stable enough for the nanometer range. In order to achieve a uniform and dense wetting of the stamp, an attempt was made to functionalize the stamp by carboxyl groups. The electrostatic interaction should ensure that proteins adhere well to the stamp. In order to facilitate the transfer, the adhesion to the substrate must be stronger than this interaction with the stamp. Therefore, epoxycoated slides were chosen as substrate. The covalent bond with an epoxide ring should be stronger than the electromagnetic interaction with the stamp surface. With this combination lines of avidin up to a width of 50 nm were already published [143].

13.2. Materials and Methods

AFM, TIRFM, and cell experiments were performed as described in part II.

Carboxylic acid-functionalized polyhedral oligomeric silsesquioxanes Briefly, Octasilane POSS was used as the starting material and epoxide groups and carboxyl groups were added using Speier catalysts (Figure 13.1A). The statistical ratio of the two at the 8 arms of the POSS could be adjusted among other things by the reaction time. The syn-

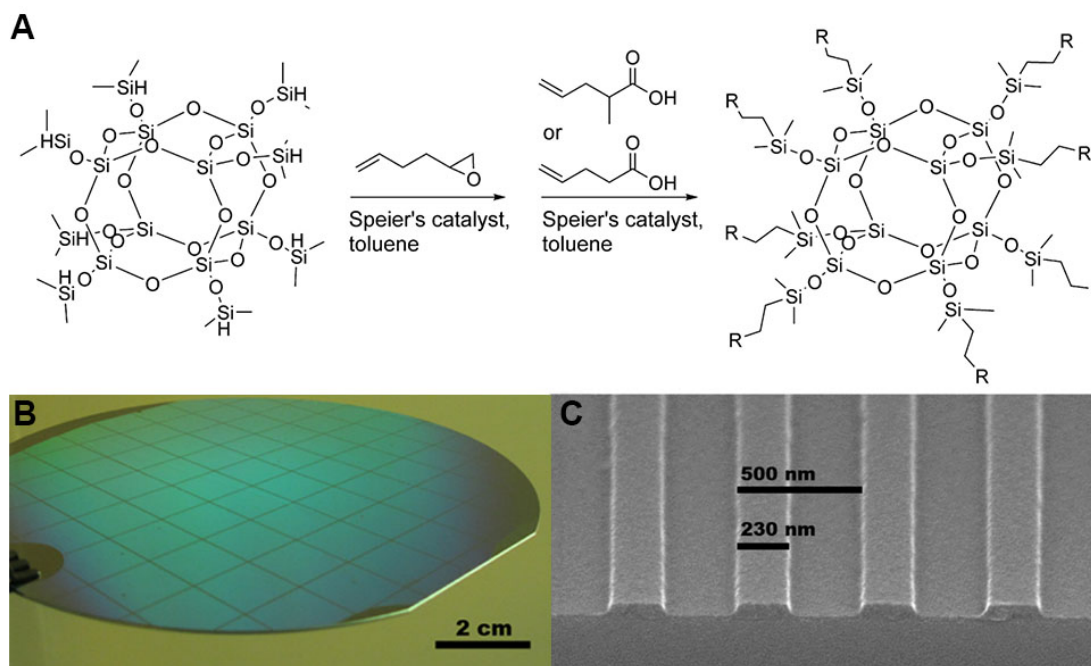


Figure 13.1.: (A) Synthesis of functionalized POSS. The rest R consists either of an epoxid- or a carboxylgroup. (B) A 4 inch wafer was successfully imprinted with the resist. (C) SEM images of the wafer. From [143].

thesis was tested by ATR-IR measurements. The resulting carboxylic acid-functionalized epoxy-POSS was finally supplemented by a photoinitiator, so that the resist could be cured by UV-NIL. Five variants of the resist were prepared with different ratios between epoxy and carboxyl groups. A line-and-space structure with a period of 500 nm was successfully imprinted on 4 inch wafers (Figure 13.1C). The synthesis was carried out in collaboration with Julia Kastner (Profactor), details of the synthesis can be found in [143].

Stamp preparation From the wafers with the functionalized POSS layer pieces were cut off between $5 \times 5 \text{ mm}^2$ and $10 \times 10 \text{ mm}^2$ using diamond cutters. The material itself is very hard, its Young's modulus is in the GPa range. Therefore, a compliant layer of soft PDMS was applied to the back and applied to an microscope slide (1 mm) for handling in the EVG. This stack was used as a stamp.

Nanocontact printing The stamps were covered with a streptavidin solution in PBS ($50 - 100 \frac{\mu\text{g}}{\text{mL}}$) for 1 – 15 min, washed with DIW and dried in a stream of nitrogen. For nanocontact printing, a EVG 620 mask aligner (EV Group, Austria) in manual micro CP mode was applied. With a 7 inch maskholder size and 6 inch substrate size, a separation distance of 30 μm , a mask thickness of 1.52 mm and a substrate thickness of 1.32 mm.

13. Nanocontact printing with hard POSS stamps

A 1 Zone-Manual chuck with the proximity NIL 1.1 were taken. The pressure of the contact force during process was 800 mbar, during WEC it was 500 mbar. The process duration was varied between 1 and 120 minutes.

13.3. Experiments

Even with constant parameters, the print results varied significantly between the individual tests. Occasionally, areas were homogeneous and dense, but most of the time the transfer was incomplete and even had gaps within a protein line (Figure 13.2A). The best results were obtained when the protein adsorption was increased to 15 min and the pressure duration was set to over one hour (Figure 13.2B-D), however, only in 12 out of 50 attempts such homogeneous lines could be detected. The FWHM of the protein top side was typically greater than 3 nm, the height of the streptavidin lines varied between 1.3 and 3.3 nm. In experiments without high pressure (e.g., manual printing), no lines could be detected regardless of the printing duration.

However, even if a region of uniform patterning could be identified by AFM, TIRFM images with fluorescent, biotinylated antibodies still showed strong inhomogeneities (Figure 13.2E-F). Finally, good areas were first identified with AFM and HeLa cells were then applied to these substrates. The labeled membrane protein CD4 could be monitored, it aligned to the nanopattern of the proteins on the substrate (Figure 13.2G).

13.4. Discussion

A dense, homogeneous protein pattern could not be produced reproducibly with these materials. Isolated areas were able to reach the quality as published in [143] with the AFM, but inhomogeneities also showed up as soon as their functionality was examined with TIRFM. No functionality measurements of the printed protein patterns were performed in the publication. It was noticeable that many areas only had a thickness of 1.5 nm and thus just half of the expected height of a streptavidin molecule. It could be that the homotetramer streptavidin denatured such that not all four monomers were transferred or were no longer functional due to contact with the stamp. This could explain why the functionality was not uniform despite promising AFM recordings.

The synthesis also required the use of toxic chemicals and corresponding devices such as IR-spectroscopy, which were mandatory to confirm the success of the synthesis. Also, the conformal high pressure cannot be achieved without a high-priced contact printing device, all manual experiments showed no protein transfer. For these reasons, and because the results were not reproducible, this method was not suitable for the membrane protein interaction assay.

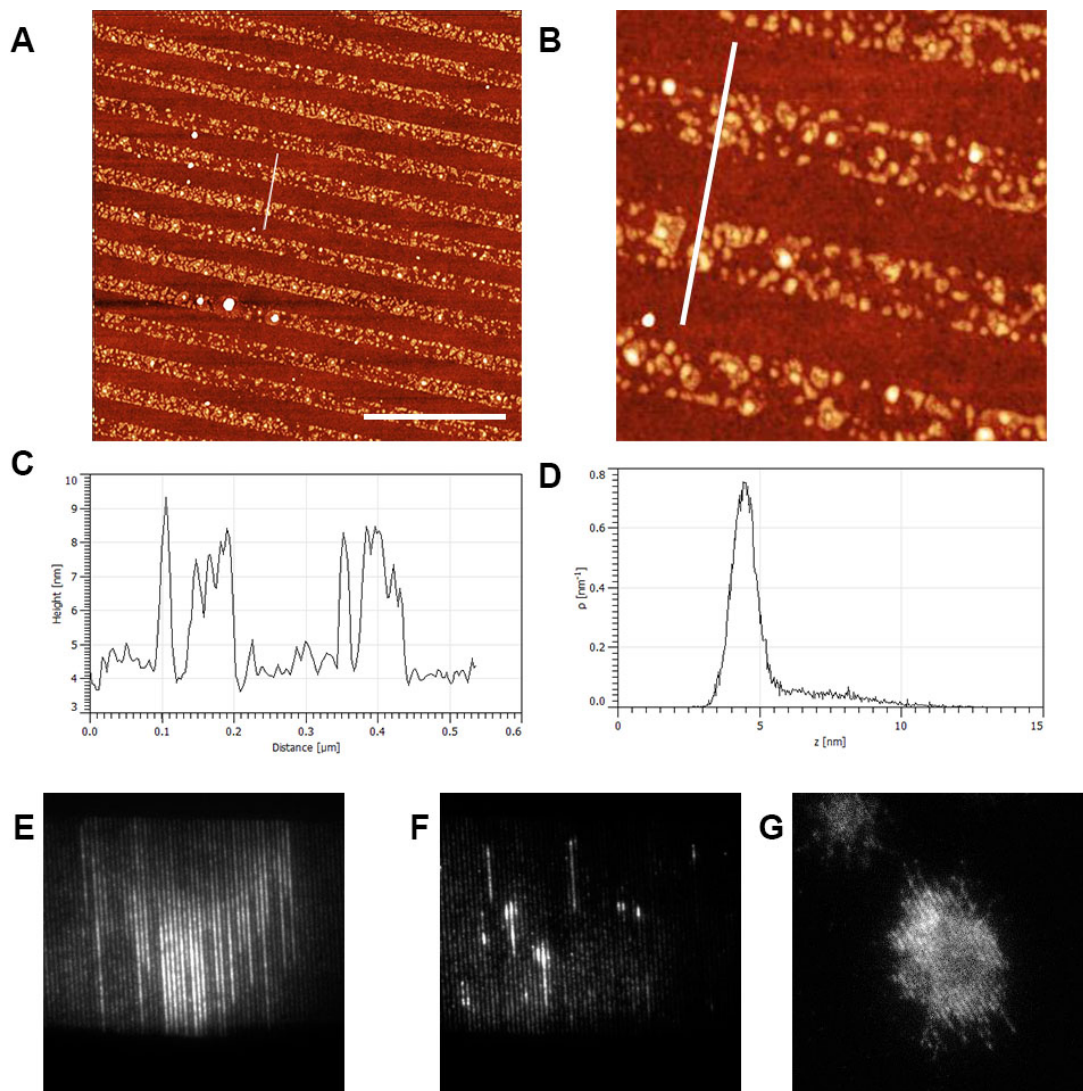


Figure 13.2.: (A) Protein patterns printed with POSS stamps resulted in most cases in an incomplete protein transfer, (B) which is especially evident in the magnification. (C) The height of the protein lines (profile of A, B) shows that it is an incomplete monolayer of streptavidin. (D) Two curves should be visible in the histogram, but the layer thickness of the protein layer is so inhomogeneous that only the substrate height can be clearly seen. (E,F) TIRFM images of biotinylated fluorophores showed further inhomogeneities in the structures. (G) Nevertheless, it was possible to align fluorescent membrane proteins in a living cell on the nanopatterns.

14. Nanopatterning of proteins with a water soluble resist

14.1. Introduction

Contact printing is a simple and established technique for micropatterning of proteins in laboratories. Despite its huge advantages, its limitations led to the inventions of alternatives. For example, contact printing is hardly suitable for mass manufacturing of nanopatterns which would enable versatile and comparable applications e.g. for membrane protein screening. In addition, multiprotein patterns are a major challenge for micro- or nanocontact printing but important for many assays.

In 2004 Hoff et al. published a method to nanopattern proteins with Nanoimprint lithography (NIL) [17]. NIL is a method presented 1995 by Steven Y. Chou to produce lateral sub 25 nm patterns in polymers. In the past 20 years, a broad variety of NIL techniques were developed, including methods to mass fabricate nanostructures like substrate conformal imprint lithography (SCIL) or roll-to-roll (R2R) NIL. Hoff et al. presented a relatively complex procedure to pattern aminosilane which then covalently immobilized biotin molecules on silicon substrate. The homotetramer streptavidin (SAV) bound with one of its binding sites to biotin with high affinity. The remaining functional groups of SAV captured finally the biotinylated target protein.

An alternative is NIL of gold-thiol. Capturing proteins with functionalized gold-thiol is an established technique, even for centimeter-scaled areas [144]. Gaubert and Frey functionalized gold-thiol patterns with fibronectin for seeding human umbilical vein endothelial cells.

NIL was also applied in the innovative technology of protein immobilization on titanium nanostructures by Moxey et al. [145]. Exploiting the photocatalytic self-cleaning characteristics of titanium, they fabricated reusable templates for protein nano- and micropatterns, reaching down to 30 nm wide features. Their method enables repeated adsorption of different proteins on Ti₂O nanostructures and their removal using simply UV-exposure. This method could be of interest for laboratories that require nanopatterns of protein but lack the required high-cost infrastructure. However, the development of the nanopatterned substrates is quite sophisticated.

Overall, NIL for protein patterning is not a new idea, however, we aim for process which in theory allows multiprotein patterning within simple washing steps and is suitable for super-resolution microscopy avoiding metal coatings. In addition, it is less hazardous since the applied polymer is water-soluble and shows low toxicity to cells.

In detail the proposed process consists of six steps (fig. 14.1):

1. Residual layer free imprinting of a water-soluble polymer
2. Modifying the polymer to adjust water-resistance
3. Covering the polymer pattern with a streptavidin solution
4. Washing with DIW, removing residual proteins and the polymer
5. Backfilling with a blocker-solution
6. Washing with DIW, removing residual blocker molecules

It is based on a residual free pattern of a water-soluble polymer. Either this is achieved directly with appropriate lithography or by an etching step. The polymer has to endure 5 – 15 min of contact to water without exposing the substrate. Thus, a modification step may be required to adjust the water-resistance. Then the first protein, for example streptavidin, covers the polymer pattern in solution. The proteins adhere to the exposed substrate surface and most probably also at the polymer. The remaining proteins in the solution are washed away in DIW together with the water-soluble polymer. It is essential that the polymer has to be dissolved residue-free so the second protein, e.g. fibronectin, can adhere to the remaining substrate surface, backfilling the pattern. Remaining polymer residuals would greatly influence the application since UV-curable resists are typically autofluorescent. The final substrate would show a pattern of two proteins defined by the NIL process. If the imprinted polymer had not only one height but several steps, multiprotein patterns would be feasible.

Step 5 and 6 are similar to most protein patterning approaches and already studied in part II. Step 3 and 4, the patterning of the first protein are the core of the presented idea but rely completely on the success of the first two steps. If a residual layer remains after imprinting the polymer, the proteins cannot adhere at the substrate. And if the polymer dissolves too fast or partly not at all, the protein coating would probably be not sufficient.

14.2. Materials and Methods

Mastering, stamp development, AFM, and SEM were identical to chapter 9 on page 36.

14. Nanopatterning of proteins with a water soluble resist

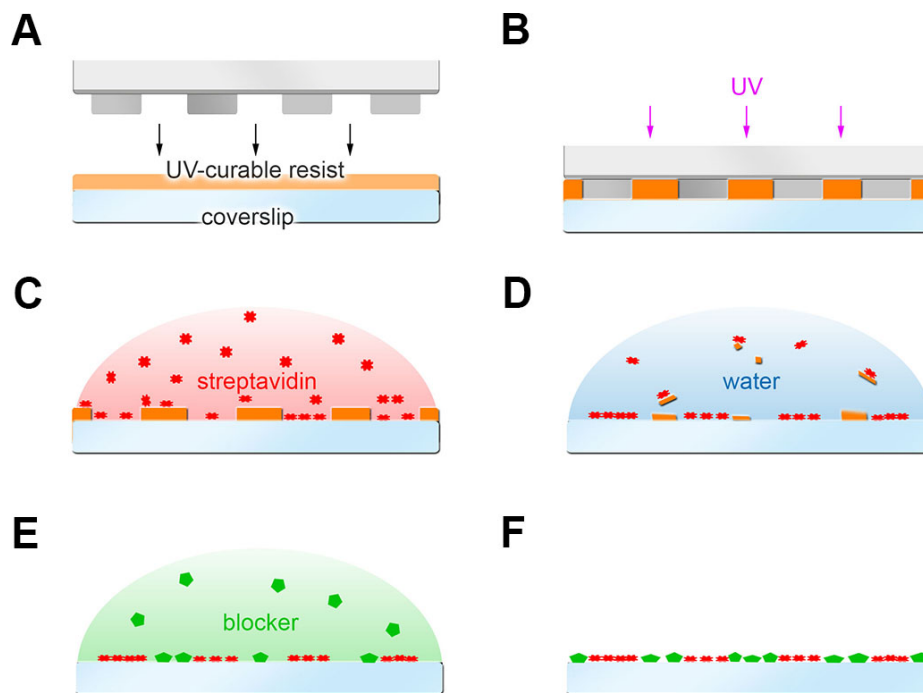


Figure 14.1.: Sketch of the novel process to nanopattern proteins with nanoimprint lithography of a water-soluble resist. (A) A high-modulus silicon stamp gets pressed into the UV-curable resist. (B) The resist gets polymerized without a residual layer. (C) Streptavidin in solution adsorbs on the glass and the polymer. (D) A washing step removes the remaining water-soluble polymer. (E) Blocker proteins fill the gaps comparable to the nCP process. (F) The final two-dimensional pattern of two proteins.

Substrate preparation Glass coverslips (#1.5, 24 × 60 mm; Menzel™, Fisher Scientific, USA) suitable for TIRFM with a thickness of 150 μm were washed with acetone and DIW and dried in a stream of nitrogen. No adhesion promoter was applied.

Nanoimprint lithography Performed on a in-house fabricated plate-to-plate tool consisting of a metal container with a built-in UV-lamp (Dedolux 03S from DELO) and a movable plate to hold the substrate (fig. 14.2). The lamp emitted in a spectrum between 325 – 600 nm and its average intensity reached 70 mW/cm² after five minutes of illumination. The resist was acquired by Joanneum Research GmbH as UV-NIL-ACMO with an absorption maximum at $\lambda = 370$ nm. A stack of glass, resist, and stamp was placed on the plate and hold in place by vacuum. The lid of the plate has to be closed tightly since a flexible foil is clamped between sample and lid. Air pressure up to around 50 kPa was pressed between foil and lid to conformal press the foil down on the sample. Due to the heat generated by the lamp the illumination container was constantly flowed by an cooling air stream. After curing, the plate was moved out again, the air pressure switched off and the lid opened. The stamp was peeled off with care from the polymerized NAM (PNAM). Switching off the vacuum, the glass with the imprint could be removed.

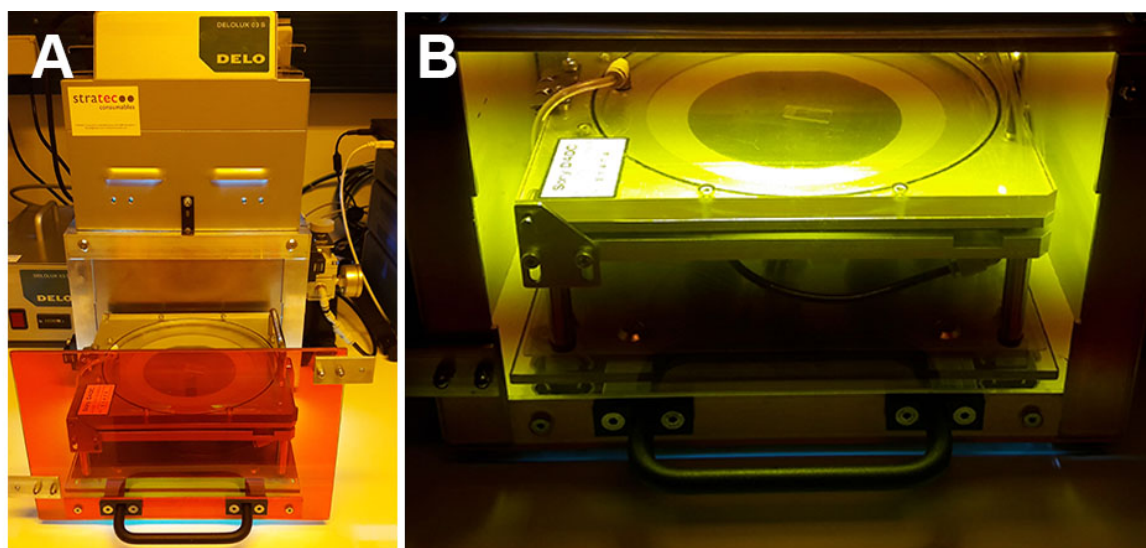


Figure 14.2.: (A) In-house fabricated plate-to-plate tool for NIL. (B) During NIL with sample inside.

Washing For the washing experiments, SecureSeal™ Hybridization Chambers by GRACE Bio-labs were glued over the imprinted polymer structures. These chambers were filled with deionized water via a micro-pipette to incubate the polymer for a desired time span. Afterwards the water got pipetted, the chamber carefully removed with a scalpel, and the substrate gently dried in a stream of filtered air.

Etching Etching of PNAM was performed with a diener electronics (Germany) ATTO, a radio frequency plasma system with 13.56 MHz. The chamber was vacuumed to 0.2 mbar and flushed with oxygen to around 0.7 mbar. This was repeated three times to ensure a reproducible, white oxygen plasma. The flow rate was adjusted to a stable pressure of 0.3 mbar. Samples were treated with a power of 50 W for 0.5 – 10 min.

14.3. Nanoimprint lithography of NAM

Imprint processes can be broken down to four steps: coat the substrate with the resist, press on the stamp to fill the cavities with the resist, cure / polymerize, and lift off. In all cases, the filling of the cavities is crucial for the success and depends mainly on three factors [146, 147]:

- external pressure by the imprint system
- capillary effects
- sorption of any gaseous phase in the cavities

For UV-NIL, the external pressure is typically very low ($<0,2$ MPa), with our setup the maximum is already reached at 50 kPa. Therefore, the other two options had to be improved while all experiments were performed at maximal pressure.

Water-soluble polymers which are suitable for nanoimprint lithography are rare. The same applies for resists which are suitable for a residual free imprint. In 2009 a method was published to produce submicron organic thin film transistors at room temperature with UV-NIL [148]. For this, a novel resist called UV-ACMO was developed which enabled residual-free NIL and its polymer was soluble in DIW. UV-ACMO is described as a mixture of a photoinitiator, N-acryloyl morpholine (NAM), and chloroform in the ratio 1:20:400. The high amount of chloroform was applied to reduce the viscosity which is critical for residual-layer free imprints. With coated hard silicon stamp they reached residual layer free structures without etching down to the nanoscale.

Polymerized NAM (PNAM) is not unknown in the biology. It found its application in block co-polymers and showed limited toxicity. Gorman et al. applied the homopolymer like a hydrogel barrier for temporal and spatial control over cell adhesion [149]. After 24 h in aqueous solution the polymer lost 75 % of its weight and cells regrew into the area of the washed polymer.

Most experiments and the evaluation was solely performed with pillars of PNAM for three reasons: First, for stamps with well cavities the influence of the capillary effect is greater, possibly reducing the need for high pressure. Second, measurements with AFM are more exact for nanopillars than for deep structures due to the lateral and spatial extent of the cantilever tip. And third, pillars would enable the patterning of

Table 14.1.: An overview of the applied nanostamps, all with a depth of 100 nm. The abbreviation will be used to identify the patterns in this part.

| Form | Abbreviation | Layout | FWHM [nm] | Period [nm] |
|-------|--------------|--------|--------------|---------------|
| wells | W200/600 | hex | 205 ± 15 | 585 ± 5 |
| wells | P200/600 | hex | 195 ± 15 | 586 ± 4 |
| wells | W300/1100 | hex | 215 ± 15 | 1155 ± 10 |
| wells | W500/1100 | hex | 510 ± 20 | 1160 ± 10 |
| wells | W500/1700 | hex | 515 ± 20 | 1700 ± 10 |
| lines | L500/2000 | linear | 500 ± 20 | 1980 ± 10 |

the blocker proteins which are typically less essential if denaturation appears due to the contact with the polymer. Especially in the nanoscale, each denaturated anchoring protein would potentially decrease the linked membrane proteins or fluorophores and thus reduce the effectiveness of the application.

Well and pillar nanopatterns of PNAM were both imprinted with the multipattern X-PDMS stamps developed for part II but due to these reasons a new nickel master with pillar features on a large area was developed to increase the usable area of the stamp.

Development of masters and stamps The master for the nanofeatures was developed with PTM as described in detail in chapter 10.1. However, a new design was developed since the focus in this part was not in different geometries but larger areas with the same pattern. Since the geometries of the same pattern increases by the PTM process with the distance from the center, a concentric design was chosen (fig. 14.3A). Again, a week at room temperature ensured the oxidation of the nickel surface before it served as master for the production of X-PDMS composite stamps (fig. 14.3B). To change the surface properties, some stamps were treated by chemical vapor deposition process with 1H, 1H, 2H, 2H-Perfluorooctyl-trichlorosilane (PFOCTS). For this modification, the surface of the silicone was activated for 15 s with O_2 plasma and then placed in a desiccator with 5 μ L of the silanes on a covers slip. The PFOCTS molecules evaporated under low pressure and bond to the presented $-OH$ groups on the activated silicone surface yielding a monolayer of the fluorocarbon groups [150]. After one hour, the stamp was rinsed with deionized water and isopropyl alcohol and dried with nitrogen gas. Due to the silanes groups of PFOCTS this modification was covalent and a modified stamp could be used numerous times.

While for nanocontact printing the feature diameter on the top side of the stamp was essential, for NIL the full width at half maximum (FWHM) is more informative due to the conic shape of the cavities. The parameters for the applied stamps are listed in table 14.1.

Microfeatures were fabricated for comparison but the focus was clearly on nanostruc-

14. Nanopatterning of proteins with a water soluble resist

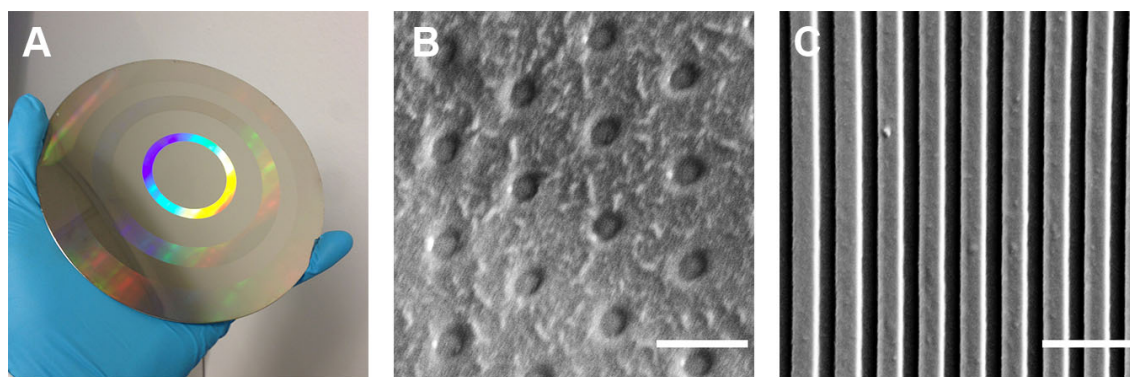


Figure 14.3.: Master and stamps for NIL (A) A 6 inch nickel master with nanowells W300/1100, W500/1100, and W500/1700 (concentric rings) was developed with PTM and electroplated with nickel. (B) SEM-image of X-PDMS composite stamp fabricated with this master. (C) Also masters and stamps were fabricated for micrometer features L500/2000. Scale bars are (B) 1 μm , (C) 3 μm .

tures. The masters with microfeatures were created with photolithography and the positive resist AZ9260 diluted in PGMEA. No surface treatment was performed before it was molded with PDMS (fig. 14.3C).

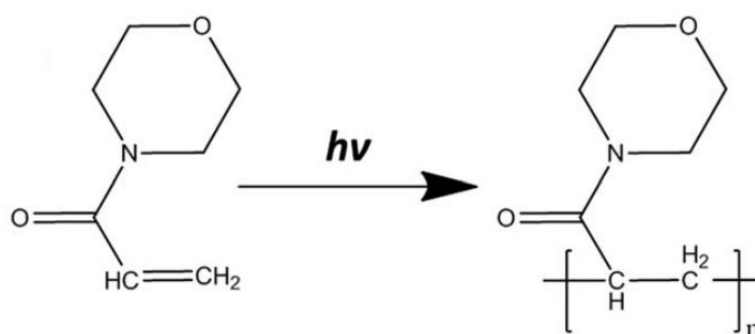


Figure 14.4.: Schematic diagram of NAM photo-polymerization to PNAM [149].

NIL of UV-curable N-acryloyl morpholine N-acryloyl morpholine (NAM) $C_7H_{11}NO_2$ is a disubstituted acrylamide derivative which is soluble in a wide range of solvents, aqueous solutions as well as organic ones [151]. It was used for a wide variety of gel-based applications. In its polymerized form (PNAM) (fig. 14.4) it was applied as an temporal spatial cell barrier since it performs as a physical hydrogel in aqueous solvents, doubling its dry weight over a 2 h period before undergoing dissolution, following a second order exponential decay profile [149]. A mixture of one percent w/v solutions of 2,2-dimethoxy-2-phenylacetophenone (DMPA) in NAM was used in this experiment and cured PNAM seemed to be non-toxic to cells. However, since nanofunctions were sought

and pure NAM is highly viscous, a UV-curable NAM with an absorption maximum of $\lambda = 370$ nm was acquired at Joanneum Research GmbH, Austria. Auner et. al called this material UV-NIL-ACMO since it is based on ACMO of Rahn GmbH which is their trivial name for acryloyl morpholine monomers. Joanneum applied it for the development of submicron organic thin film transistors [148]. According to this publication, UV-NIL-ACMO is fabricated by a mixture of GENOCURE*LTM, acryloyl morpholine, and chloroform at a mass ratio of 1:20:400. Due to the low viscosity of this pre-polymer and the high polarity difference between a silicon stamp and UV-NIL-ACMO, residual layer free imprints were achieved.

NAM monomers have a steam point at 60°C [152], chloroform has a boiling point at 61°C , both are highly toxic for cells. Since the homopolymer of NAM has a glass transition temperature of $T_g = 140^\circ\text{C}$ [152], it was expected that these materials could be removed by elevated temperature. Samples of pillars (W500/1000) were prepared and the shrinkage after post-exposure bakes was measured. A temperature of 100°C was applied to prevent deformation but also samples were tested with 140°C and 170°C . After 20 min neither the height nor the FWHM of PNAM pillars changed for both 100°C and 140°C . At 170°C , melting of PNAM could be observed. With this experiments it could not be clarified if monomers or chloroform were present in PNAM. However, since no changes greater than the error bar could be measured (except for the melted PNAM) it is not expected that major amount of toxic molecules were present in the final polymer. In addition, they probably could be removed by exposing the polymer to a temperature around 100°C , far below the critical T_g .

Gaseous phase sorption in the cavities of the silicone stamps The main pressure hindering the filling the stamp features is the remaining gas trapped in the cavities. If the polymer stamp is highly gas-permeable like a PDMS stamp [153], the gas diffuses into the polymer and its volume is replaced by the resist. This process is dependent on time and temperature and relies mainly on the stamp material and the vapor molecules.

Another important property regarding imprinting is the solubility of the resist in the stamp material. Solubility for materials in polymers is often defined by its degree of swelling S . An experimental approach to this value is to place a dry, solid piece of the polymer with the length D_0 into the solvent for 24h then measure the new dimension D . The swelling is defined as

$$S = D/D_0 \quad (14.1)$$

Water does not swell PDMS at all ($S = 1,00$), acetone slightly ($S = 1,06$) but chloroform to a huge amount ($S = 1,39$) [154]. In the applied resist, the NAM monomers are highly diluted in chloroform. The swelling is not known for X-PDMS to this detail, however, since it is a derivate of PDMS with higher cross-linking, similar properties can

14. Nanopatterning of proteins with a water soluble resist

be expected. In addition, the X-PDMS layer is thin compared to the backplane of PDMS which functions in this case not only as a compliant layer for the mechanical stress but also for the absorption of molecules.

It was tested if imprints with the resist were achievable with X-PDMS stamps and varied the duration while the stamp is in contact with pre-polymer before curing. The material could influence chloroform absorption and gaseous phase decrease. The polymer was qualified and quantified by AFM. However, no differences were detectable for imprints with a contact time of 5 min, 10 min or for 45 min. For these experiments, the dimensions of the wells or pillars did not change within the error bars even for the smallest features (fig. 14.5). However, with only 1 min of contact time before exposure, the imprints mostly failed. Therefore, for further experiments the contact time was set to 5 min.

CVD-coating of stamps with PFOCTS The capillary filling is only possible in the case of a low-viscous resists and is defined by the contact angle of the resist on the stamp surface. Water and chloroform show a angle greater than 90° for silicones which is contraproductive for the capillary effect. Thus experiments were performed with PFOCTS coated stamps to achieve residual-layer free imprints.

The average pillar height for uncoated W200/600 stamps was 95 ± 5 nm, the FWHM was 210 ± 10 nm. For the PFOCTS treated stamps, the height shrank for around 25 nm to 70 ± 5 nm, however, the FWHM increased to 240 ± 20 nm. This can be explained by the conic shape of the cavities in the silicone stamps and is a result of the mastering with PTM. Since the pillars are not as high as imprinted without PFOCTS coating, the cavities were only partly filled before curing, resulting in an apparently more compressed version of the pillars. Measuring the full width of imprints without coating at the height of the half maximum of imprints with coated stamps, it is 245 ± 15 nm, which strongly supports this theory. The same applies for W500/1100 stamps but in limited proportion. With coating the height was 87 ± 5 nm, with PFOCTS it shrank merely to 80 ± 5 nm. If the PFOCTS coating provides a barrier for gases and supresses the absorption of air and chloroform could not be verified but is suspected.

Regarding its residual layer, the phase image of the W200/600-pillars indicated that the material of the pillars and at the bottom are similar. We performed a scratch test to expose the glass substrate as reference but the residual layer could not be removed by scalpel. Later experiments with plasma verified that a polymer residual layer was still present.

Nevertheless, with PFOCTS coated microfeatures stamps, residual layer free imprints were achieved despite the low pressure we could apply with our NIL-tool. The height of the microfeatures was very heterogenic on a larger scale and typically less than 40 % of the height of the cavities (fig. 14.6). Again, lower gas permeability may be the reason for the height difference. The larger volume of the micrometer sized cavities could take more resist before the gaseous pressure reaches its threshold. We expect this to be the

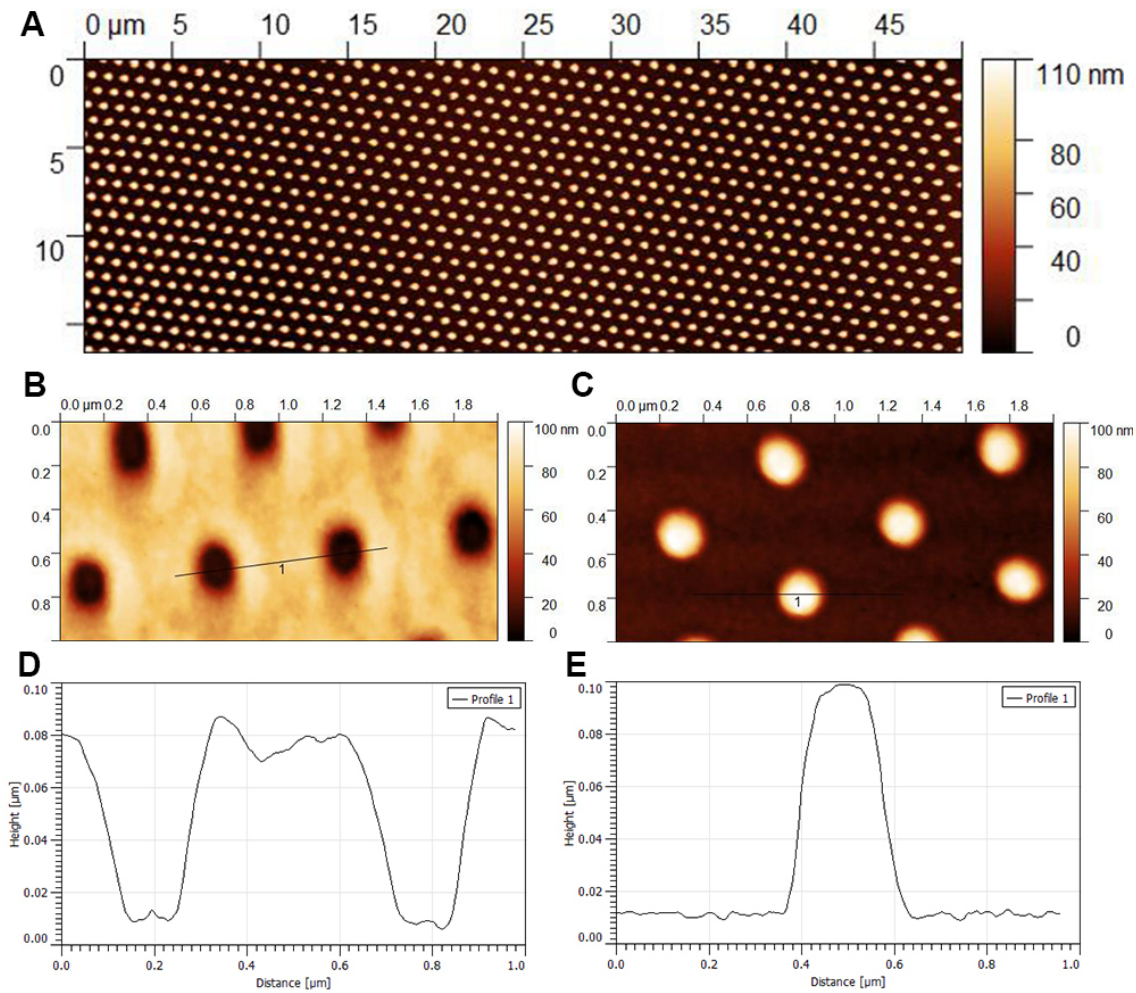


Figure 14.5.: Smallest imprinted features. (A) The printing was homogeneous over several mm. Here is a 50 μm overview shown since no nanopillars would be recognizable on a mm large overview. Both wells W200/600 (B) and pillars p200/600 (C) could be successfully imprinted, their line profiles are shown in (D,E), respectively.

14. Nanopatterning of proteins with a water soluble resist

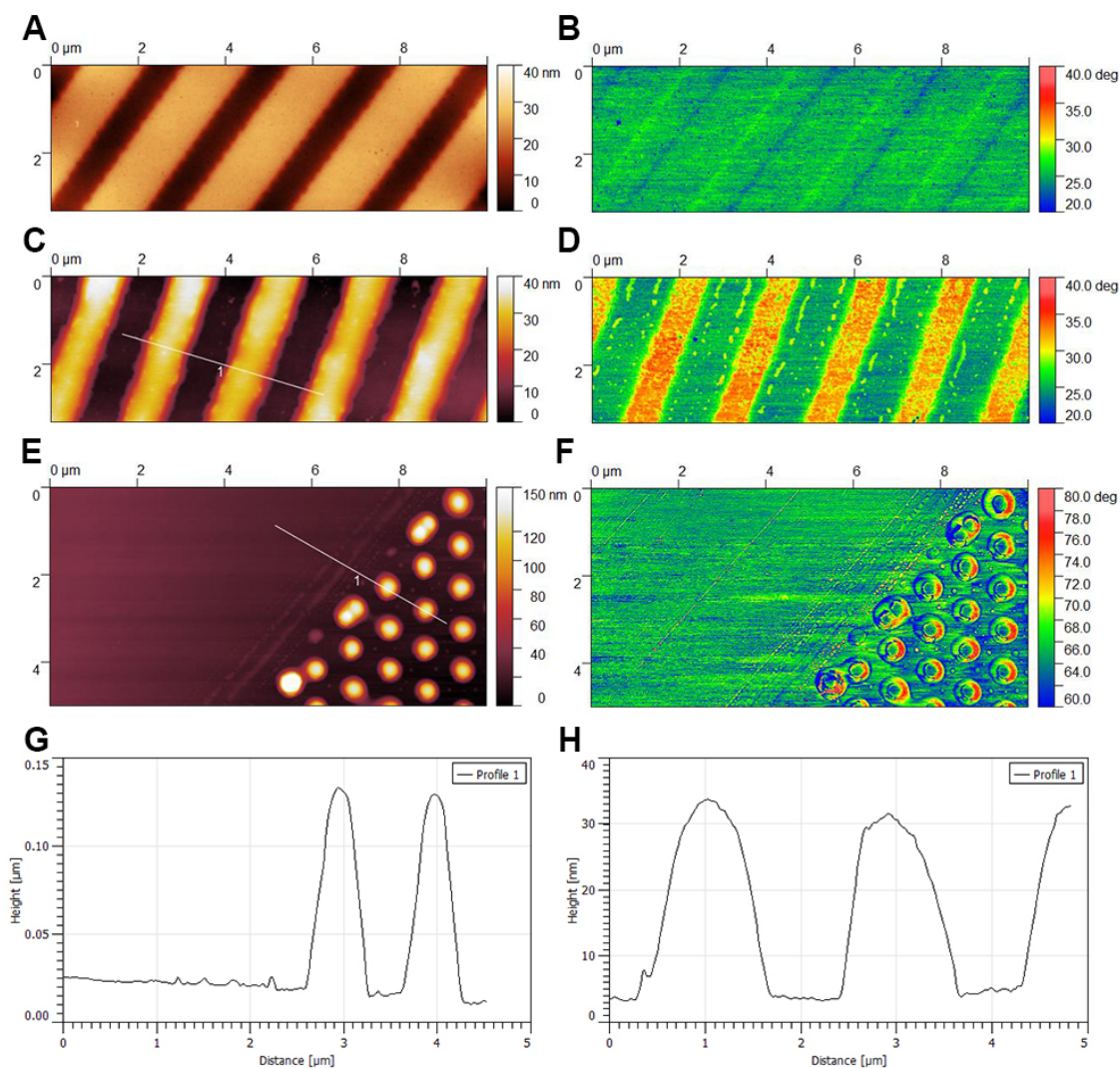


Figure 14.6.: AFM measurements (tapping mode) of imprinted PNAM. **(A,B)** Micro-lines imprinted by uncoated stamps showed the same phase both for top and bottom regions, indicating the same material and thus a residual layer. **(C,D)** For micro-lines imprinted with PFOCTS-coated stamps, the phase image indicates a residual layer free imprint, although only low pressure could be applied by the NIL tool. **(E,F)** For the nanopillars, no residual layer free imprint was achieved for all variations in coating and geometry. **(G,H)** are the line profiles of (E,C), respectively.

reason why the resist under the microscopic stamp features was repressed and residual layer free imprints were achieved.

Plasma etching of the residual layer The typical thickness of the residual layer with stamp protrusion heights of 100 – 200 nm is around 10 – 20 nm [155]. Etching is the common procedure to remove this residual layer. Often highly anisotropic etching is applied to keep the lateral dimensions intact. We used a plasma chamber with oxygen to expose the polymer to isotropic etching which would also decrease the width of the pillars and thus further lead to the nanoscale, enabling several patterns with the same period but different width with just one stamp.

According to the last experiments, PFOCTS treated stamps showed at least for the micro sized features residual layer free imprints. We performed the etching experiments both with PFOCTS modified stamps and untreated ones. Again, we focused on nanopillars since their height can be measured more accurately. Samples were checked with AFM and then O_2 plasma etched for various durations (0, 5 – 10 min) and measured again.

PNAM-pillars W200/600 reduced in 30 s oxygen plasma treatment their height by around 35 nm from 70 ± 5 nm to 35 ± 10 nm, the full width at half maximum (FWHM) decreased from 240 ± 20 nm to 180 ± 35 nm, which is a loss of around 25%. Pillars W500/1100 showed a weaker effect by the plasma, they reduced from 85 ± 5 nm to 75 ± 15 nm after 0, 5 min and were stable in this height for at least 10 min.

The huge error of the final heights is a result of the produced surface roughness and the geometrical irregularities in the plasma treated pillars (fig. 14.7). The residual layer showed cracks and hindered a more detailed quantification regarding the etching since it was unclear to which ratio the residual layer shrank compared to the exposed pillars. The reference bottom layer was taken on the top of the residual layer, ignoring the cracks.

We expect that isotropic etching appeared both at the pillars and the residual layer which kept the relative height constant. The absolute height with the glass surface as reference should decrease but could not be measured. The fading of the FWHM supports this theory.

14.4. Modifying water solubility of polymerized NAM

The water-solubility of the polymer is essential for the presented method. However, the polymer also needed to be stable for the duration of the protein adsorption to the polymer-free areas which we expect to take around 5 – 15 min. Since first tests in DIW showed the immediate washing of the nanopillars, we evaluated physical options to modify the water-solubility. An overview of the experiments can be found in table

14. Nanopatterning of proteins with a water soluble resist

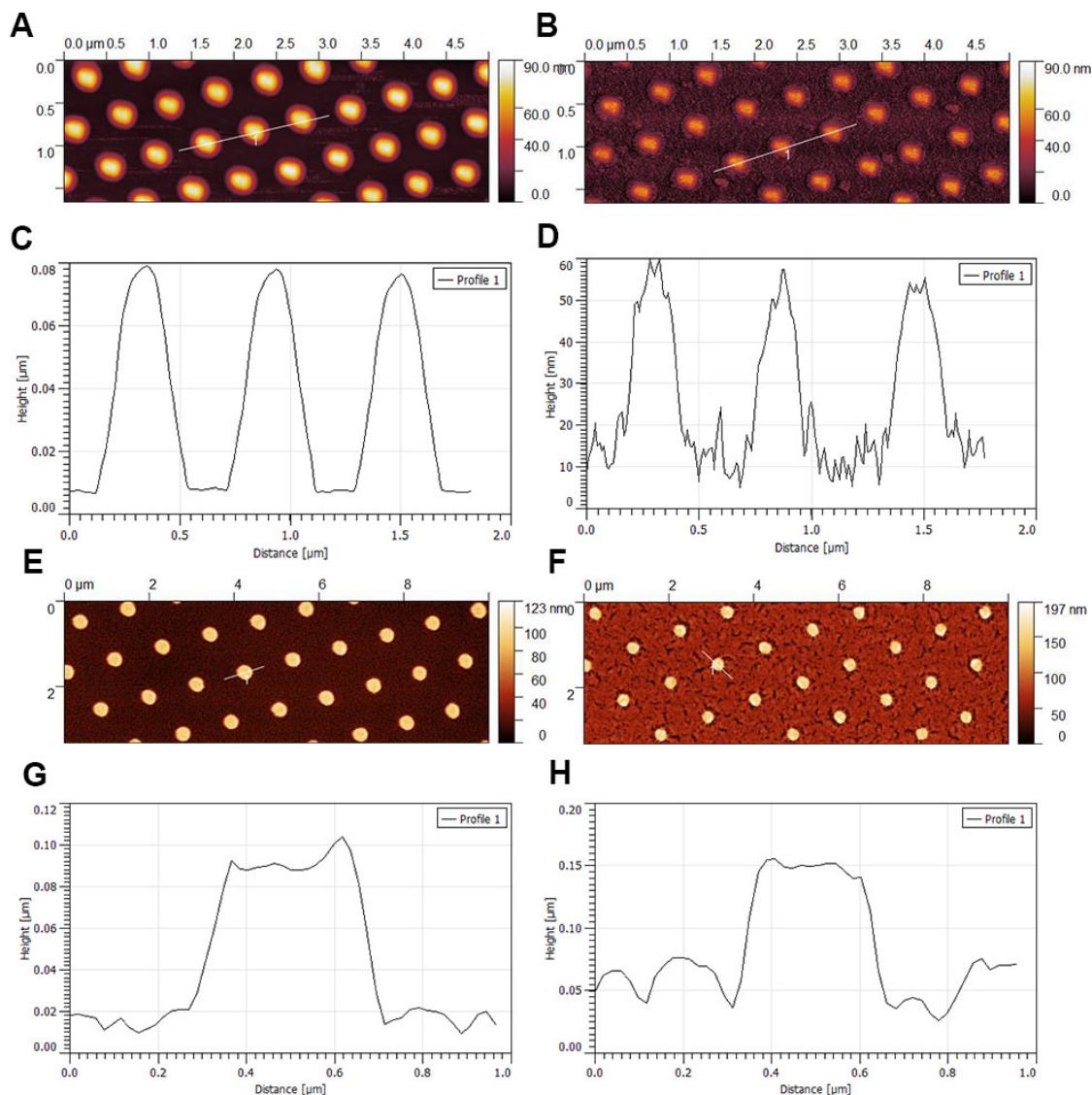


Figure 14.7.: (A) Pillars imprinted with PFOCTS coated stamps W200/600 show a reduced height of 70 ± 5 nm compared to untreated stamps which result in pillars of 95 ± 5 nm. (B) After 30 s in oxygen plasma, the polymer roughened significantly and pillars height decreased to 35 ± 10 nm. (E,F) The same applies for pillars of W500/1100 stamps but to a lesser degree. (C,D,G,H) show the line profiles of (A,B,E,F), respectively. In all plasma treated samples, the residual layer roughened.

14.2 on page 100.

Pre-exposure bake In photolithography, a resist gets spincoated on the wafer and baked before the exposure. This pre-exposure-bake or soft bake is important to decrease the amount of solvent which is necessary to achieve a homogeneous and thin layer. For our NIL experiments, the high amount of chloroform as solvent was essential for the low viscosity of the resist and thus for filling up the nanocavities. On the other hand, chloroform could hinder a dense polymerization of PNAM reducing its water-resistance in consequence. Therefore, we performed a pre-exposure bake after applying the W500/1100 stamp on the resist but before the lithography. The cavities should be filled with resist but absorb slowly the chloroform and the ratio of NAM-monomers to solvent in the cavities should increase.

The temperature for the bakes was set above the boiling point $T_b = 61\text{ °C}$ of chloroform but below the boiling point of NAM monomers 150 °C [152]. The pre-polymer was baked at 80 and 90 °C for 5, 10, and 20 min. The height of the pillars was measured to see the influence of swelling (fig. 14.8).

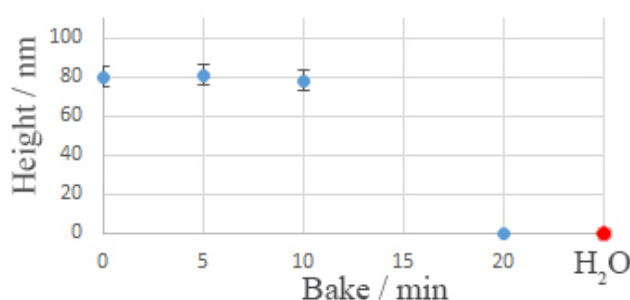


Figure 14.8.: Pre-exposure bakes at 90 °C for different baking times. Up to 10 min they had no influence on the height but after 20 min no imprint could be achieved. All pillars could be dissolved in less than 1 min.

For 5 and 10 min at both temperatures, the pre-bake did not influence the height. However, after 20 min for both 80 and 90 °C, no visible patterns were achievable anymore. Unfortunately, for all pre-exposure bakes, no change in water-solubility could be detected. All patterns were washed away in less than 1 min in DIW. Therefore, we did not determine the reason for the imprinting failures after 20 min. We suspect that swelling was not responsible since the height of the successful imprints did not depend on temperature or baking time up to several minutes.

Post-exposure bake Post-exposure bakes are essential for photolithography. The exposure itself initiates the polymerization, e.g. by creating radicals in the resist, but for many resists the main part of the polymerization is typically performed during the

14. Nanopatterning of proteins with a water soluble resist

post-exposure bake. Therefore it also referred as hard bake in literature. However, a bake after the nanoimprint step is relatively uncommon. Resists for NIL are usually developed to polymerize the complete available material since the patterns are already predefined by the topology of the stamp. Nevertheless, an elevated temperature may still support further cross-linking and thus increase the water-stability of the polymer.

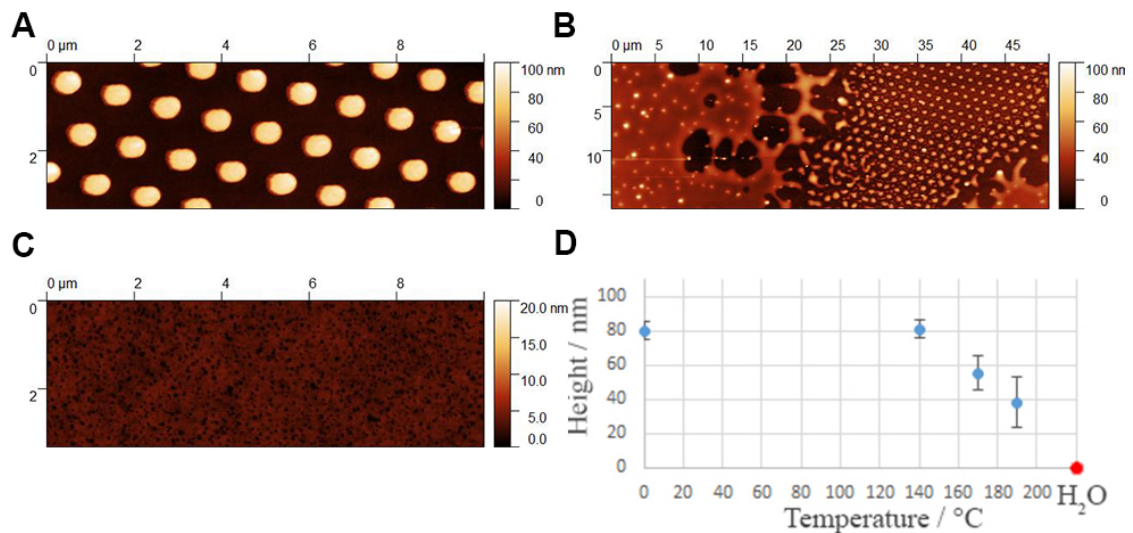


Figure 14.9.: (A) Post-exposure bake at $T_g = 140$ °C for 20 min did not measurably influence the pillars while (B) for 190 °C melting appeared on a large scale. (C) All baked samples looked similar after 1 min in DIW, no pillars were preserved. (D) Shrinkage of the pillars appeared for all samples above T_g .

Again we fabricated pillars of W500/1100 and measured height and FWHM. The post-bake temperatures were varied between 100 and 190 °C, the glass transition temperature of the homopolymer PNAM is at $T_g = 140$ °C [152]. After 100 and 140 °C for 20 min on a covered hotplatem the pillars looked similar to the reference within the error bars. The 170 °C treated pillars looked irregular, showing inhomogeneous meltings or evaporations. The height shrank significantly from 80 ± 5 nm to 55 ± 10 nm but the FWHM grew to 410 ± 15 nm. Finally, after the highest applied temperature of 190 °C, the pillars showed clear melting signs and shrank both in height and FWHM (fig. 14.9).

Unfortunately, the tested post-exposure bakes did not influence the water-solubility of the nano features. After 1 min in contact with DIW, no pillars were visible for any post-bake treatment (fig. 14.9). Since even the pillars dissolved which were treated at or above the glass transition temperature, we assume that for the applied resist and NIL process no further cross-linking could be enforced by a post-exposure bake.

Plasma treatment Although the residual layer was still present after the etching in chapter 14.3, we also tested the water solubility for these plasma treated samples. The

idea was, that the longest plasma treatment could have etched the residual layer to a thickness of only several nanometers and thus dissolve faster than the pillars. Samples of W500/1100 were prepared, plasma treated for 10 min and incubated with DIW for 1 min. After drying, the residual layer was still intact but also the pillars withstood the washing procedure for the first time. We increased the washing duration to the required 10 min and the form became very heterogeneous with an height in a range of 15-30 nm but with a very rough residual layer (fig. 14.10). After 30 min the pillars were removed but residues covered the surface with a wide up to several hundred nanometers and a maximal height of around 10 nm. It could not be determined if they were caused by the pillars or the residual layer.

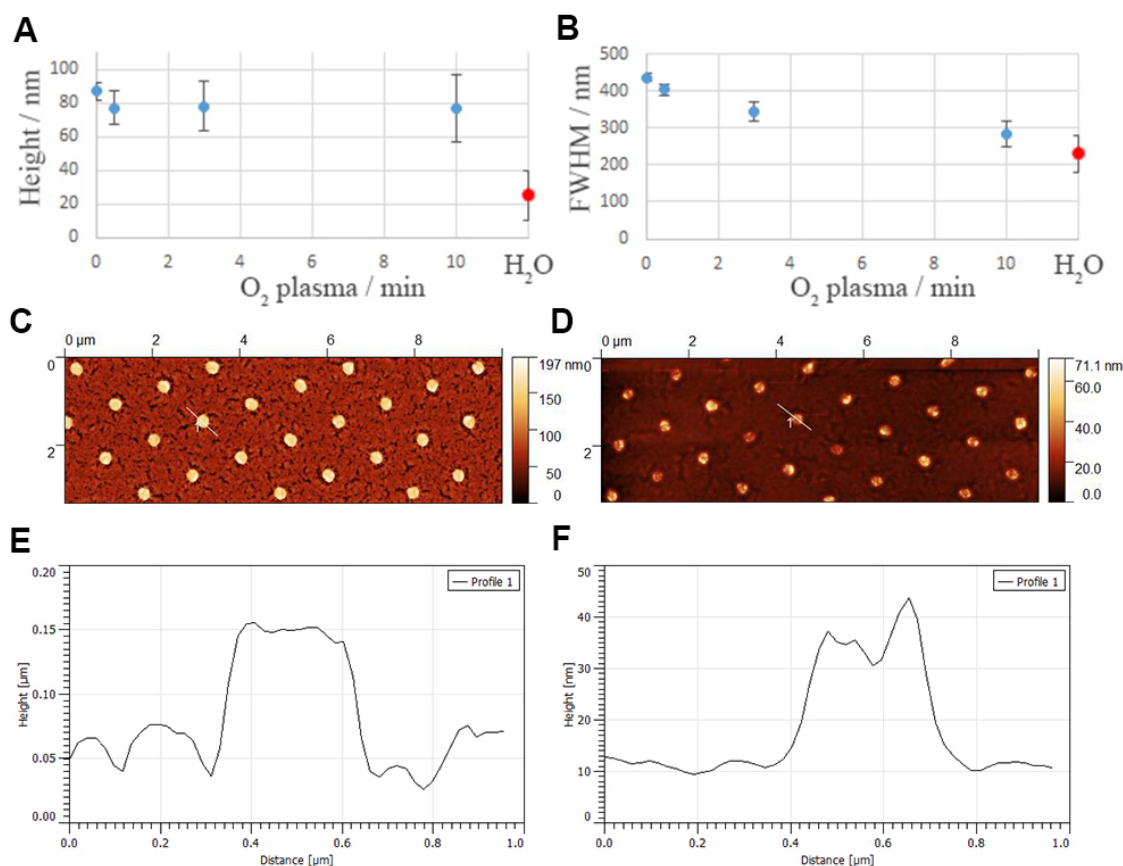


Figure 14.10.: PNAM pillars W500/1100 with residual layer were treated with oxygen plasma. (A) The oxygen plasma reduced the height in the first 30 s but this effect stagnated for at least 10 min. (B) Opposite to this stagnation, the FWHM reduces for longer plasma treatments. The red dots at "H₂O" represent the measured values after the washing procedure with samples which were treated for 10 min. (C) The surface roughness increased visibly with a 10 min treatment but the (D) the pillars withstood water incubation for 10 min. (E,F) show the line profiles of (C,D), respectively.

We repeated the experiments with samples put into the plasma chamber but only ex-

14. Nanopatterning of proteins with a water soluble resist

Table 14.2.: Overview of the presented experiments with the nanopillars. The listed pre-exposure bakes were performed at 90 °C, post-exposure bakes for 20 min. Water resistance stands for the qualitative evaluation of the nanopillars to withstand 1 min in DIW. The height and the full width at half maximum (FWHM) was measured with AFM. * measured at the non-melted areas.

| stamp | PFOCTS | Pre-bake /min | Post-bake /°C | Plasma /min | Height /nm | FWHM /nm | Water res. |
|-----------|--------|------------------|------------------|----------------|---------------|-------------|---------------|
| W500/1100 | w/o | - | - | - | 87 ± 5 | 433 ± 10 | - |
| W500/1100 | w/ | - | - | - | 80 ± 5 | 437 ± 10 | - |
| W500/1100 | w/o | - | - | 0.5 | 77 ± 15 | 405 ± 15 | + |
| W500/1100 | w/o | - | - | 3 | 79 ± 20 | 345 ± 25 | + |
| W500/1100 | w/o | - | - | 10 | 77 ± 25 | 285 ± 35 | + |
| W500/1100 | w/ | 5 | - | - | 81 ± 5 | 435 ± 10 | - |
| W500/1100 | w/ | 10 | - | - | 78 ± 5 | 435 ± 10 | - |
| W500/1100 | w/ | 20 | - | - | - | - | - |
| W500/1100 | w/ | - | 100 | - | 79 ± 5 | 435 ± 10 | - |
| W500/1100 | w/ | - | 140 | - | 81 ± 5 | 430 ± 10 | - |
| W500/1100 | w/ | - | 170 | - | 55 ± 10* | 410 ± 15* | - |
| W500/1100 | w/ | - | 190 | - | 38 ± 5* | 390 ± 30* | - |
| W200/1000 | w/o | - | - | - | 95 ± 3 | 210 ± 10 | - |
| W200/600 | w/o | - | - | - | 96 ± 3 | 210 ± 10 | - |
| W200/600 | w/ | - | - | - | 70 ± 2 | 240 ± 20 | - |
| W200/600 | w/ | - | - | 0.5 | 35 ± 10 | 180 ± 35 | + |
| W200/600 | w/ | - | - | 6 | 30 ± 15 | 140 ± 40 | + |

posed to vacuum without ignition of the gas. The mentioned increased water-resistance was not achieved for these samples. Therefore, we expect that the highly reactive -OH-groups and radicals which were induced by the plasma are responsible for the increased water-resistance. When these reactive groups diffuse or rotate into the bulk, cross-linking may appear, producing a highly-dense barrier with a depth of one nanometer or even less. If this hypothesis should be correct, carefully adjusting the plasma parameters could produce an adequate dense barrier to prevent quick water solution but keep the water-solubility of the PNAM-bulk material. Since the pillars were detectable after 10 min but removed after 30 min, the achievable timescales look promising. However, it still has to be verified if this effect is also present if the pillars are not supported by a residual layer.

14.5. Discussion

Residual layer free polymer It was possible to produce reproducible PNAM nanostructures with X-PDMS stamps and up to 200 nm wide pillars and wells. By AFM recordings, however, could be shown that a residual layer was still present. This layer may not be present for the further process steps, but could neither be avoided by coating the stamp with PFOCTS nor be removed by oxygen plasma.

For nanoimprints, pressure, contact angle and gaseous sorption are crucial for a good imprint. However, the nanostructures were already 80 to 90 % filled and yet the residual layer was present. On the other hand, PFOCTS-coated PDMS stamps with micrometer features allowed for a layer-free residual pressure, even at only 50 kPa, the maximum available pressure of the NIL system. The filling of microfeature cavities, however, depends more on the gas pressure, which was low in this case, since the cavities were only partially filled. To increase the pressure, Auner et al. used rigid silicon stamps instead of silicone stamps and a R2R setup [148, 156]. R2R has only one line of contact compared to area-area in P2P-NIL. Since the pressure p depends directly on the ratio of force to area $p = F/A$, the same force that would be used for both techniques would result in a much higher pressure at R2R. In addition, a much higher pressure was typically applied to rigid stamp (modulus of elasticity $E \approx \text{GPa}$) than to silicone stamps ($E \approx \text{MPa}$), as it is more critical to achieve conformal contact. It is therefore reasonable to suppose that the low pressure of the NIL device used could be one of the main reasons for the remaining layer of nanostructures.

Water-resistance of PNAM It has been found that a pre-exposure bake has no effect on the water solubility of PNAM. But as soon as it was baked for at least 20 min at 80 °C or 90 °C, it was no longer possible to produce nanopatterns. Due to the importance of the low viscosity for filling cavities at the nanoscale, we assume that the amount of the solvent chloroform (boiling point at 61 °C) is reduced to a subcritical level. Damage to the photoinitiator is not expected since parts without features were still cured.

Post-exposure baking also showed no effect on the water solubility of PNAM. The stability of the dimensions of the pillars even at the glass transition temperature of PNAM indicated that the polymerization was complete and no NAM monomers (boiling point 60 °C) were available for further crosslinking. In addition, it is assumed that only very few chloroform molecules were present in the fully cured polymer. Further tests on cells must, however, confirm this hypothesis.

Only the samples exposed to O_2 plasma showed water resistance. This was unexpected since the plasma treatment was only planned for isotropic etching of the residual layer. Although the dimensions changed, the plasma-treated pillars withstood 10 min of DIW. This duration would be sufficient for the adsorption of proteins at typical concentrations in the range of 100 – 1000 $\frac{\mu\text{g}}{\text{mL}}$. However, as not only the pillars but also the residual

14. Nanopatterning of proteins with a water soluble resist

layer remained stable during water contact, the ability of O_2 plasma to reduce the water solubility of PNAM can be meaningfully further analyzed only with residue-free structures. However, increasing the cross-linking of the polymer surface could provide a promising opportunity to increase the water resistance of the polymer in a controlled manner without altering its high water solubility below the surface.



Die approbierte gedruckte Originalversion dieser Dissertation ist an der TU Wien Bibliothek verfügbar.
The approved original version of this doctoral thesis is available in print at TU Wien Bibliothek.



Die approbierte gedruckte Originalversion dieser Dissertation ist an der TU Wien Bibliothek verfügbar.
The approved original version of this doctoral thesis is available in print at TU Wien Bibliothek.

Part IV.

Appendix

List of Figures

| | | |
|--------|--|----|
| 4.1. | The membrane protein interaction assay. | 7 |
| 5.1. | Sketch of PTM process. | 9 |
| 5.2. | Defect of NIL with hard stamps. | 11 |
| 5.3. | Comparing NIL principles. | 12 |
| 5.4. | PDMS and X-PDMS. | 15 |
| 6.1. | Model cell membrane. | 18 |
| 6.2. | Ribbon diagrams of SAV, FNT, and BSA. | 19 |
| 6.3. | Protein adhesion promoter. | 21 |
| 7.1. | The AFM principle. | 23 |
| 7.2. | Lennard-Jones potential | 24 |
| 7.3. | Jablonski diagram and Airy disks | 26 |
| 7.4. | Principle of TIRFM. | 27 |
| 7.5. | Principle of dSTORM. | 30 |
| 7.6. | Sketch of STED. | 31 |
| 8.1. | Sketch of nanocontact printing with X-PDMS stamps. | 35 |
| 10.1. | Overview of the design for the PTM-master. | 41 |
| 10.2. | SEM and AFM images of the X-PDMS stamp. | 46 |
| 10.3. | Characterization of printed proteins | 48 |
| 10.4. | Washing of glass substrate. | 49 |
| 10.5. | Comparing nCP on different coatings. | 50 |
| 10.6. | RICM images of a short-term cured X-PDMS stamp. | 54 |
| 10.7. | AFM images of smallest features with PTM masters. | 54 |
| 10.8. | Protein height depends on concentration. | 57 |
| 10.9. | Plots of concentration experiments. | 58 |
| 10.10. | Stamp defects by ultra-sonic bath. | 59 |
| 10.11. | AFM images of incubated SAV in FNT patterns. | 60 |
| 10.12. | TIRFM image of a Hela-cd4-mclover cell. | 62 |
| 10.13. | STORM of FNT W300/600. | 63 |
| 11.1. | X-PDMS stamp of Eulitha master. | 67 |
| 11.2. | AFM images of FNT nanorings. | 69 |
| 11.3. | AFM images of W80/140 prints of BSA. | 70 |

| | | |
|--------|--|----|
| 11.4. | Statistics of succes rate for minimal feature sizes. | 71 |
| 11.5. | STED of W300/600 and W80/140. | 73 |
| 13.1. | Synthesis of POSS | 81 |
| 13.2. | Protein patterns with POSS stamps. | 83 |
| 14.1. | Sketch of novel protein patterning process with NIL. | 86 |
| 14.2. | In-house fabricated plate-to-plate tool for NIL. | 87 |
| 14.3. | Master and stamps for NIL. | 90 |
| 14.4. | NAM polymerization PNAM. | 90 |
| 14.5. | Smallest imprinted PNAM features. | 93 |
| 14.6. | Samples of imprints w/ and w/o residual layer. | 94 |
| 14.7. | Plasma treated nanopillars of PNAM. | 96 |
| 14.8. | Plots of the pre-baking time. | 97 |
| 14.9. | Post-exposure bake melting and washing results. | 98 |
| 14.10. | Plasma treated nanopillars showed an increased water-resistance. | 99 |

Bibliography

- [1] Markus Sällman Almén, Karl J. V. Nordström, Robert Fredriksson, and Helgi B. Schiöth. Mapping the human membrane proteome: A majority of the human membrane proteins can be classified according to function and evolutionary origin. *BMC biology*, 7:50, 2009. ISSN 1741-7007. doi: 10.1186/1741-7007-7-50.
- [2] John P. Overington, Bissan Al-Lazikani, and Andrew L. Hopkins. How many drug targets are there? *Nature reviews. Drug discovery*, 5(12):993–996, 2006. ISSN 1474-1776. doi: 10.1038/nrd2199.
- [3] Miriam Barrios-Rodiles, Kevin R. Brown, Barish Ozdamar, Rohit Bose, Zhong Liu, Robert S. Donovan, Fukiko Shinjo, Yongmei Liu, Joanna Dembowy, Ian W. Taylor, Valbona Luga, Natasa Przulj, Mark Robinson, Harukazu Suzuki, Yoshihide Hayashizaki, Igor Jurisica, and Jeffrey L. Wrana. High-throughput mapping of a dynamic signaling network in mammalian cells. *Science (New York, N.Y.)*, 307(5715):1621–1625, 2005. ISSN 1095-9203. doi: 10.1126/science.1105776.
- [4] G. Rigaut, A. Shevchenko, B. Rutz, M. Wilm, M. Mann, and B. Séraphin. A generic protein purification method for protein complex characterization and proteome exploration. *Nature biotechnology*, 17(10):1030–1032, 1999. ISSN 1087-0156. doi: 10.1038/13732.
- [5] Tom K. Kerppola. Design and implementation of bimolecular fluorescence complementation (bifc) assays for the visualization of protein interactions in living cells. *Nature protocols*, 1(3):1278–1286, 2006. ISSN 1750-2799. doi: 10.1038/nprot.2006.201.
- [6] K. H. Young. Yeast two-hybrid: So many interactions, (in) so little time. *Biology of reproduction*, 58(2):302–311, 1998. ISSN 0006-3363.
- [7] Damien Maurel, Laëtitia Comps-Agrar, Carsten Brock, Marie-Laure Rives, Emmanuel Bourrier, Mohammed Akli Ayoub, Hervé Bazin, Norbert Tinel, Thierry Durroux, Laurent Prézeau, Eric Trinquet, and Jean-Philippe Pin. Cell-surface protein-protein interaction analysis with time-resolved fret and snap-tag technologies: Application to gpcr oligomerization. *Nature methods*, 5(6):561–567, 2008. ISSN 1548-7091. doi: 10.1038/nmeth.1213.
- [8] Kenichi G. N. Suzuki, Takahiro K. Fujiwara, Fumiyuki Sanematsu, Ryota Iino, Michael Edidin, and Akihiro Kusumi. Gpi-anchored receptor clusters transiently

- recruit lyn and g alpha for temporary cluster immobilization and lyn activation: Single-molecule tracking study 1. *The Journal of cell biology*, 177(4):717–730, 2007. ISSN 0021-9525. doi: 10.1083/jcb.200609174.
- [9] Francis J. Alenghat and David E. Golan. Membrane protein dynamics and functional implications in mammalian cells. *Current topics in membranes*, 72:89–120, 2013. ISSN 1063-5823. doi: 10.1016/B978-0-12-417027-8.00003-9.
- [10] Tobias Kaufmann and Bart Jan Ravoo. Stamps, inks and substrates: Polymers in microcontact printing. *Polymer Chemistry*, 1(4):371, 2010. ISSN 1759-9954. doi: 10.1039/b9py00281b.
- [11] James L. Wilbur, amit kumar, Enoch Kim, and George M. Whitesides. Microfabrication by microcontact printing of self-assembled monolayers. *Advanced Materials*, 6(7-8):600–604, 1994. ISSN 0935-9648. doi: 10.1002/adma.19940060719.
- [12] Younan Xia and George M. Whitesides. Extending microcontact printing as a microlithographic technique. *Langmuir : the ACS journal of surfaces and colloids*, 13(7):2059–2067, 1997. ISSN 0743-7463. doi: 10.1021/la960936e.
- [13] A. S. Blawas and W. M. Reichert. Protein patterning. *Biomaterials*, 19(7-9):595–609, 1998. ISSN 01429612.
- [14] Gang-Yu Liu and Nabil A. Amro. Positioning protein molecules on surfaces: A nanoengineering approach to supramolecular chemistry. *Proceedings of the National Academy of Sciences of the United States of America*, 99(8):5165–5170, 2002. ISSN 0027-8424. doi: 10.1073/pnas.072695699.
- [15] D. L. Wilson, R. Martin, S. Hong, M. Cronin-Golomb, C. A. Mirkin, and D. L. Kaplan. Surface organization and nanopatterning of collagen by dip-pen nanolithography. *Proceedings of the National Academy of Sciences of the United States of America*, 98(24):13660–13664, 2001. ISSN 0027-8424. doi: 10.1073/pnas.241323198.
- [16] C. K. Harnett, K. M. Satyalakshmi, and H. G. Craighead. Low-energy electron-beam patterning of amine-functionalized self-assembled monolayers. *Applied Physics Letters*, 76(17):2466–2468, 2000. ISSN 00036951. doi: 10.1063/1.126378.
- [17] J. Damon Hoff, Li-Jing Cheng, Edgar Meyhöfer, L. Jay Guo, and Alan J. Hunt. Nanoscale protein patterning by imprint lithography. *Nano Letters*, 4(5):853–857, 2004. ISSN 1530-6984. doi: 10.1021/nl049758x.
- [18] Marcus A. Verschuuren. Patent: Silicone rubber material for soft lithography. ep 2 599 835 b1, 2009.
- [19] Marc A. Verschuuren, Mischa Megens, Yongfeng Ni, Hans Van Sprang, and Albert Polman. Large area nanoimprint by substrate conformal imprint lithography (SCIL). *Advanced Optical Technologies*, 6(3-4):243–264, 2017. ISSN 21928584. doi: 10.1515/aot-2017-0022.

Bibliography

- [20] Michaela Schwarzenbacher, Martin Kaltenbrunner, Mario Brameshuber, Clemens Hesch, Wolfgang Paster, Julian Weghuber, Bettina Heise, Alois Sonnleitner, Hannes Stockinger, and Gerhard J. Schütz. Micropatterning for quantitative analysis of protein-protein interactions in living cells. *Nature methods*, 5(12):1053–1060, 2008. ISSN 1548-7091. doi: 10.1038/nmeth.1268.
- [21] Eva Sevcsik, Mario Brameshuber, Martin Fölser, Julian Weghuber, Alf Honigmann, and Gerhard J. Schütz. Gpi-anchored proteins do not reside in ordered domains in the live cell plasma membrane. *Nature communications*, 6:6969, 2015. ISSN 2041-1723. doi: 10.1038/ncomms7969.
- [22] Eva Sevcsik and Gerhard J. Schütz. With or without rafts? alternative views on cell membranes. *BioEssays : news and reviews in molecular, cellular and developmental biology*, 38(2):129–139, 2016. ISSN 1521-1878. doi: 10.1002/bies.201500150.
- [23] Mario Brameshuber, Eva Sevcsik, Benedikt K. Rossboth, Christina Manner, Hans-Peter Deigner, Begüm Peksel, Mária Péter, Zsolt Török, Albin Hermetter, and Gerhard J. Schütz. Oxidized phospholipids inhibit the formation of cholesterol-dependent plasma membrane nanoplatforms. *Biophysical journal*, 110(1):205–213, 2016. ISSN 0006-3495. doi: 10.1016/j.bpj.2015.11.018.
- [24] Gerhard J. Schütz, Julian Weghuber, Peter Lanzerstorfer, and Eva Sevcsik. Protein micropatterning assay: Quantitative analysis of protein-protein interactions. *Methods in molecular biology (Clifton, N.J.)*, 1550:261–270, 2017. ISSN 1064-3745.
- [25] Helmut Schift. Nanoimprint lithography: An old story in modern times? a review. *Journal of Vacuum Science & Technology B: Microelectronics and Nanometer Structures*, 26(2):458, 2008. ISSN 0734211X. doi: 10.1116/1.2890972.
- [26] M. Mühlberger, M. Rohn, J. Danzberger, E. Sonntag, A. Rank, L. Schumm, R. Kirchner, C. Forsich, S. Gorb, B. Einwögerer, E. Trappl, D. Heim, H. Schift, and I. Bergmair. Uv-nil fabricated bio-inspired inlays for injection molding to influence the friction behavior of ceramic surfaces. *Microelectronic Engineering*, 141:140–144, 2015. ISSN 01679317. doi: 10.1016/j.mee.2015.02.051.
- [27] Akira Kouchiyama, Katsuhisa Aratani, Yoshihiro Takemoto, Takashi Nakao, Shinichi Kai, Kiyoshi Osato, and Kenzo Nakagawa. High-resolution blue-laser mastering using an inorganic photoresist. *Japanese Journal of Applied Physics*, 42(2S):769, 2003. ISSN 1347-4065. URL <http://stacks.iop.org/1347-4065/42/i=2S/a=769>.
- [28] Kiyoshi Osato. Phase transition mastering for blu-ray rom disc. In *Optical Data Storage*, page MD1. Optical Society of America, 2003. doi: 10.1364/ODS.2003.MD1.

- [29] Donald Barnhart. Bit-mapped holograms using phase transition mastering (ptm) and blu-ray disks. *Journal of Physics: Conference Series*, 415:012039, 2013. ISSN 1742-6596. doi: 10.1088/1742-6596/415/1/012039.
- [30] Chun-Cheng Chang, Jung-Po Chen, Kuo-Chi Chiu, Chieh-Wen Chen, and Wei-Hsiang Wang. Phase transition mastering technology for the stamper of blu-ray recordable disc. *Japanese Journal of Applied Physics*, 50(9S1):09MD01, 2011. ISSN 1347-4065. doi: 10.1143/JJAP.50.09MD01. URL <http://iopscience.iop.org/article/10.1143/JJAP.50.09MD01/pdf>.
- [31] Stephen Y. Chou, Peter R. Krauss, and Preston J. Renstrom. Imprint of sub-25 nm vias and trenches in polymers. *Applied Physics Letters*, 67(21):3114, 1995. ISSN 00036951. doi: 10.1063/1.114851.
- [32] Jan Haisma. Mold-assisted nanolithography: A process for reliable pattern replication. *Journal of Vacuum Science & Technology B: Microelectronics and Nanometer Structures*, 14(6):4124, 1996. ISSN 0734211X. doi: 10.1116/1.588604.
- [33] P. Ruchhoeft, M. Colburn, B. Choi, H. Nounu, S. Johnson, T. Bailey, S. Damle, M. Stewart, J. Ekerdt, S. V. Sreenivasan, J. C. Wolfe, and C. G. Willson. Patterning curved surfaces: Template generation by ion beam proximity lithography and relief transfer by step and flash imprint lithography. *Journal of Vacuum Science & Technology B: Microelectronics and Nanometer Structures*, 17(6):2965, 1999. ISSN 0734211X. doi: 10.1116/1.590935.
- [34] Michael D. Austin, Haixiong Ge, Wei Wu, Mingtao Li, Zhaoning Yu, D. Wasserman, S. A. Lyon, and Stephen Y. Chou. Fabrication of 5nm linewidth and 14nm pitch features by nanoimprint lithography. *Applied Physics Letters*, 84(26):5299–5301, 2004. ISSN 00036951. doi: 10.1063/1.1766071.
- [35] Tobias Balla, S. Mark Spearing, and Andrew Monk. An assessment of the process capabilities of nanoimprint lithography. *Journal of Physics D: Applied Physics*, 41(17):174001, 2008. ISSN 0022-3727. doi: 10.1088/0022-3727/41/17/174001.
- [36] Nazrin Kooy, Khairudin Mohamed, Lee Tze Pin, and Ooi Su Guan. A review of roll-to-roll nanoimprint lithography. *Nanoscale research letters*, 9(1):320, 2014. ISSN 1556-276X. doi: 10.1186/1556-276X-9-320.
- [37] Younan Xia and George M. Whitesides. Soft lithography. *Angewandte Chemie International Edition*, 37(5):550–575, 1998. ISSN 14337851.
- [38] Marc Verschuuren. Substrate conformal imprint lithography for nanophotonics. *Ph.D. Thesis Utrecht University*, 2009.
- [39] I. D. Johnston, D. K. McCluskey, C. K. L. Tan, and M. C. Tracey. Mechanical characterization of bulk sylgard 184 for microfluidics and microengineering. *Journal of Micromechanics and Microengineering*, 24(3):035017, 2014. ISSN 0960-1317. doi: 10.1088/0960-1317/24/3/035017.

Bibliography

- [40] Horst Kuchling. *Taschenbuch der Physik*. Carl Hanser, 2011. ISBN 978-3-446-42457-9.
- [41] Wolfgang Weißbach. *Werkstoffkunde: Strukturen, Eigenschaften, Prüfung*. Springer-Verlag, 2012. ISBN 3-8348-8318-2.
- [42] Andrea Cattoni, E. Cambril, D. Decanini, G. Faini, and A. M. Haghiri-Gosnet. Soft uv-nil at 20nm scale using flexible bi-layer stamp casted on hsq master mold. *Microelectronic Engineering*, 87(5-8):1015–1018, 2010. ISSN 01679317. doi: 10.1016/j.mee.2009.11.106.
- [43] Celal Con, Jian Zhang, Zeinab Jahed, Ting Y. Tsui, Mustafa Yavuz, and Bo Cui. Thermal nanoimprint lithography using fluoropolymer mold. *Microelectronic Engineering*, 98:246–249, 2012. ISSN 01679317. doi: 10.1016/j.mee.2012.07.007.
- [44] David L. Nelson and Michael M. Cox. *Lehninger principles of biochemistry*. W.H. Freeman, New York, N.Y. and Basingstoke, 5th ed. edition, 2008. ISBN 1429208929.
- [45] S. J. Singer and G. L. Nicolson. The fluid mosaic model of the structure of cell membranes. *Science (New York, N.Y.)*, 175(4023):720–731, 1972. ISSN 1095-9203.
- [46] Garth L. Nicolson. The fluid-mosaic model of membrane structure: Still relevant to understanding the structure, function and dynamics of biological membranes after more than 40 years. *Biochimica et biophysica acta*, 1838(6):1451–1466, 2014. ISSN 0006-3002. doi: 10.1016/j.bbamem.2013.10.019.
- [47] P. G. Saffman and M. Delbrück. Brownian motion in biological membranes. *Proceedings of the National Academy of Sciences of the United States of America*, 72(8):3111–3113, 1975. ISSN 0027-8424. URL <http://www.pnas.org/content/72/8/3111>.
- [48] Kerstin Weiß, Andreas Neef, Qui Van, Stefanie Kramer, Ingo Gregor, and Jörg Enderlein. Quantifying the diffusion of membrane proteins and peptides in black lipid membranes with 2-focus fluorescence correlation spectroscopy. *Biophysical journal*, 105(2):455–462, 2013. ISSN 0006-3495. doi: 10.1016/j.bpj.2013.06.004.
- [49] Ali Najji, Alex J. Levine, and P. A. Pincus. Corrections to the saffman-delbruck mobility for membrane bound proteins. *Biophysical journal*, 93(11):L49–51, 2007. ISSN 0006-3495. doi: 10.1529/biophysj.107.119222.
- [50] Jeremy Mark Berg, John L. Tymoczko, Gregory Joseph Gatto, and Lubert Stryer. *Biochemistry*. W. H. Freeman and Company and Palgrave Macmillan, New York, 7th, international ed., 3rd print edition, op. 2012. ISBN 1429276355.
- [51] N. M. Green. Avidin. *Advances in protein chemistry*, 29:85–133, 1975. ISSN 0065-3233.

- [52] C. R. Sabanayagam, C. L. Smith, and C. R. Cantor. Oligonucleotide immobilization on micropatterned streptavidin surfaces. *Nucleic acids research*, 28(8):E33, 2000. ISSN 1362-4962.
- [53] Karen L. Christman, Michael V. Requa, Vanessa D. Enriquez-Rios, Sabrina C. Ward, Kenneth A. Bradley, Kimberly L. Turner, and Heather D. Maynard. Sub-micron streptavidin patterns for protein assembly. *Langmuir : the ACS journal of surfaces and colloids*, 22(17):7444–7450, 2006. ISSN 0743-7463. doi: 10.1021/la0608213.
- [54] T. Sano and C. R. Cantor. Cooperative biotin binding by streptavidin. electrophoretic behavior and subunit association of streptavidin in the presence of 6 m urea. *The Journal of biological chemistry*, 265(6):3369–3373, 1990. ISSN 0021-9258.
- [55] Rockland Immunochemicals Inc. Streptavidin properties and characterization; last visited: 02.03.2018: Protocol. 2018. URL <https://rockland-inc.com/>.
- [56] Jody L. Swift and David T. Cramb. Nanoparticles as fluorescence labels: Is size all that matters? *Biophysical journal*, 95(2):865–876, 2008. ISSN 0006-3495. doi: 10.1529/biophysj.107.127688.
- [57] K. M. Yamada and I. Pastan. The relationship between cell surface protein and glucose and alpha-aminoisobutyrate transport in transformed chick and mouse cells. *Journal of cellular physiology*, 89(4):827–829, 1976. ISSN 0021-9541. doi: 10.1002/jcp.1040890450.
- [58] Debra J. Romberger. Fibronectin. *The International Journal of Biochemistry & Cell Biology*, 29(7):939–943, 1997. ISSN 13572725. doi: 10.1016/S1357-2725(96)00172-0.
- [59] F. Grinnell and M. K. Feld. Fibronectin adsorption on hydrophilic and hydrophobic surfaces detected by antibody binding and analyzed during cell adhesion in serum-containing medium. *The Journal of biological chemistry*, 257(9):4888–4893, 1982. ISSN 0021-9258.
- [60] H. P. Erikson, N. Carrell, and J. McDonagh. Fibronectin molecule visualized in electron microscopy: A long, thin, flexible strand. *Journal of Cell Biology*, 91(3 I):673–678, 1981. ISSN 00219525. doi: 10.1083/jcb.91.3.673.
- [61] Valentin Nelea, Yukiko Nakano, and Mari T. Kaartinen. Size distribution and molecular associations of plasma fibronectin and fibronectin crosslinked by transglutaminase 2. *The protein journal*, 27(4):223–233, 2008. ISSN 1572-3887. doi: 10.1007/s10930-008-9128-1.
- [62] Inge Axelsson. Characterization of proteins and other macromolecules by agarose gel chromatography. *Journal of Chromatography A*, 152(1):21–32, 1978. ISSN 00219673. doi: 10.1016/S0021-9673(00)85330-3.

- [63] Streptavidin; last visited: 24.04.2018. URL <https://en.wikipedia.org/wiki/Streptavidin>.
- [64] Fibronectin; last visited: 24.04.2018. URL <https://en.wikipedia.org/wiki/Fibronectin>.
- [65] Bovine serum albumin; last visited: 24.04.2018. URL https://en.wikipedia.org/wiki/Bovine_serum_albumin.
- [66] A G Castaño, V Hortigüela, A Lagunas, C Cortina, and J Samitier. Soft Matter Protein patterning of hydrogels by direct microcontact printing : application to cardiac differentiation. 2014.
- [67] Eva Sykova and Serhiy Forostyak. Stem Cells in Regenerative Medicine. *Laser Therapy*, 22(2):87–92, 2013. ISSN 0898-5901. doi: 10.5978/islsm.13-RE-01.
- [68] David B. Allison, Xiangqin Cui, Grier P. Page, and Mahyar Sabripour. Microarray data analysis: From disarray to consolidation and consensus. *Nature reviews. Genetics*, 7(1):55–65, 2006. ISSN 1471-0056. doi: 10.1038/nrg1749.
- [69] Gavin Macbeath, Stuart L Schreiber, Gavin Macbeath, and Stuart L Schreiber. Printing Proteins as Microarrays for High-Throughput Function Determination Published by : American Association for the Advancement of Science Stable URL : <http://www.jstor.org/stable/3077849> REFERENCES Linked references are available on JSTOR for this ar. 289(5485):1760–1763, 2016.
- [70] Christer Wingren and C. A K Borrebaeck. Progress in miniaturization of protein arrays-a step closer to high-density nanoarrays. *Drug Discovery Today*, 12(19-20): 813–819, 2007. ISSN 13596446. doi: 10.1016/j.drudis.2007.08.003.
- [71] Brian B. Haab. Antibody Arrays in Cancer Research: Fig. 1. *Molecular & Cellular Proteomics*, 4(4):377–383, 2005. ISSN 1535-9476. doi: 10.1074/mcp.M500010-MCP200. URL <http://www.mcponline.org/lookup/doi/10.1074/mcp.M500010-MCP200>.
- [72] Christer Wingren and Carl AK Borrebaeck. Protein Microarray Technologies for Detection and Identification of Bacterial and Protein Analytes. In *Principles of Bacterial Detection: Biosensors, Recognition Receptors and Microsystems*, pages 715–729. Springer New York, New York, NY, 2008. doi: 10.1007/978-0-387-75113-9_26. URL http://link.springer.com/10.1007/978-0-387-75113-9_{_}26.
- [73] Adnan Mujahid, Naseer Iqbal, and Adeel Afzal. Bioimprinting strategies: From soft lithography to biomimetic sensors and beyond. *Biotechnology Advances*, 31(8):1435–1447, 2013. ISSN 07349750. doi: 10.1016/j.biotechadv.2013.06.008. URL <http://dx.doi.org/10.1016/j.biotechadv.2013.06.008>.

- [74] Cindy Dirscherl and Sebastian Springer. Protein micropatterns printed on glass: Novel tools for protein-ligand binding assays in live cells. *Engineering in Life Sciences*, 18(2):124–131, 2018. ISSN 16182863. doi: 10.1002/elsc.201700010.
- [75] Spencer A. Freeman, Jesse Goyette, Wendy Furuya, Elliot C. Woods, Carolyn R. Bertozzi, Wolfgang Bergmeier, Boris Hinz, P. Anton Van Der Merwe, Raibatak Das, and Sergio Grinstein. Integrins Form an Expanding Diffusional Barrier that Coordinates Phagocytosis. *Cell*, 164(1-2):128–140, 2016. ISSN 10974172. doi: 10.1016/j.cell.2015.11.048. URL <http://dx.doi.org/10.1016/j.cell.2015.11.048>.
- [76] G. Fülöp, M. Brameshuber, A.M. Arnold, G.J. Schütz, and E. Sevcsik. Determination of the membrane environment of CD59 in living cells. *Biomolecules*, 8(2), 2018. ISSN 2218273X. doi: 10.3390/biom8020028.
- [77] Sara Löchte, Sharon Waichman, Oliver Beutel, Changjiang You, and Jacob Piehler. Live cell micropatterning reveals the dynamics of signaling complexes at the plasma membrane. *Journal of Cell Biology*, 207(3):407–418, 2014. ISSN 15408140. doi: 10.1083/jcb.201406032.
- [78] Sandra March, Vyas Ramanan, Kartik Trehan, Shengyong Ng, Ani Galstian, Nil Gural, Margaret A. Scull, Amir Shlomai, Maria M. Mota, Heather E. Fleming, Salman R. Khetani, Charles M. Rice, and Sangeeta N. Bhatia. Micropatterned coculture of primary human hepatocytes and supportive cells for the study of hepatotropic pathogens. *Nature Protocols*, 10(12):2027–2053, 2015. ISSN 17502799. doi: 10.1038/nprot.2015.128. URL <http://dx.doi.org/10.1038/nprot.2015.128>.
- [79] K. D. Mossman, Gabriele Campi, Jay T Groves, and Michael L Dustin. Altered TCR Signaling from Geometrically Repatterned Immunological Synapses. *Science*, 310(5751):1191–1193, nov 2005. ISSN 0036-8075. doi: 10.1126/science.1119238. URL <http://www.ncbi.nlm.nih.gov/pubmed/16293763><http://www.sciencemag.org/cgi/doi/10.1126/science.1119238>.
- [80] Karen L. Christman, Michael V. Requa, Vanessa D. Enriquez-Rios, Sabrina C. Ward, Kenneth A. Bradley, Kimberly L. Turner, and Heather D. Maynard. Submicron Streptavidin Patterns for Protein Assembly. *Langmuir*, 22(17):7444–7450, aug 2006. ISSN 0743-7463. doi: 10.1021/la0608213. URL <http://www.ncbi.nlm.nih.gov/pubmed/16893251><http://pubs.acs.org/doi/abs/10.1021/la0608213>.
- [81] S. Lenci, L. Tedeschi, F. Pieri, and C. Domenici. UV lithography-based protein patterning on silicon: Towards the integration of bioactive surfaces and CMOS electronics. *Applied Surface Science*, 257(20):8413–8419, aug 2011. ISSN 01694332. doi: 10.1016/j.apsusc.2011.04.096. URL <http://linkinghub.elsevier.com/retrieve/pii/S0169433211006416>.

- [82] Dan V. Nicolau, Elena P. Ivanova, Florin Fulga, Luisa Filipponi, Andrea Viezzoli, Serban Dobroiu, Yulia V. Alekseeva, and Duy K. Pham. Protein immobilisation on micro/nanostructures fabricated by laser microablation. *Biosensors and Bioelectronics*, 26(4):1337–1345, dec 2010. ISSN 0956-5663. doi: 10.1016/J.BIOS.2010.07.044. URL <https://www.sciencedirect.com/science/article/pii/S0956566310004197?via%3Dihub>.
- [83] Ansgar Waldbaur, Holger Rapp, Kerstin Länge, and Bastian E. Rapp. Let there be chip - Towards rapid prototyping of microfluidic devices: One-step manufacturing processes. *Analytical Methods*, 3(12):2681–2716, 2011. ISSN 17599660. doi: 10.1039/c1ay05253e.
- [84] Sami Alom Ruiz and Christopher S. Chen. Microcontact printing: A tool to pattern. *Soft Matter*, 3(2):168–177, 2007. ISSN 1744683X. doi: 10.1039/b613349e.
- [85] Emmanuel Delamarche, André Bernard, Heinz Schmid, Alexander Bietsch, , Bruno Michel, and Hans Biebuyck. Microfluidic Networks for Chemical Patterning of Substrates: Design and Application to Bioassays. 1998. doi: 10.1021/JA973071F. URL <https://pubs.acs.org/doi/abs/10.1021/ja973071f>.
- [86] A. Bernard, J. P. Renault, B. Michel, H. R. Bosshard, and E. Delamarche. Microcontact printing of proteins. *Advanced Materials*, 12(14):1067–1070, 2000. ISSN 0935-9648.
- [87] Steffen J. Sahl, Stefan W. Hell, and Stefan Jakobs. Fluorescence nanoscopy in cell biology. *Nature Reviews Molecular Cell Biology*, 18(11):685, 2017. ISSN 1471-0080.
- [88] Jinan Chai, L. S. Y. Wong, Louise Ruh yu Giam, and Chad A. Mirkin. Single-molecule protein arrays enabled by scanning probe block copolymer lithography. *Proceedings of the National Academy of Sciences of the United States of America*, 108 49:19521–5, 2011.
- [89] Author Ki-bum Lee, So-jung Park, Chad A Mirkin, Jennifer C Smith, Source Science, New Series, No Mar, Ki-bum Lee, So-jung Park, Chad A Mirkin, and Jennifer C Smith. Linked references are available on JSTOR for this article : Protein Nanoarrays Generated By Dip-Pen Nanolithography. 295(5560):1702–1705, 2016.
- [90] Guo-Jun Zhang, Takashi Tanii, Yuzo Kanari, and Iwao Ohdomari. Production of nanopatterns by a combination of electron beam lithography and a self-assembled monolayer for an antibody nanoarray. *Journal of nanoscience and nanotechnology*, 7(2):410–417, 2007. ISSN 1533-4880.
- [91] Benjamin Harke, Paolo Bianchini, Fernando Brandi, and Alberto Diaspro. Photopolymerization inhibition dynamics for sub-diffraction direct laser writing lithography. *ChemPhysChem*, 13(6):1429–1434, 2012. doi: 10.1002/cphc.201200006.

- [92] Moritz Wiesbauer, Richard Wollhofen, Borislav Vasic, Kurt Schilcher, Jaroslaw Jacak, and Thomas A. Klar. Nano-anchors with single protein capacity produced with sted lithography. *Nano Letters*, 13(11):5672–5678, 2013. doi: 10.1021/nl4033523. PMID: 24111646.
- [93] Stine H. Kristensen, Gitte A. Pedersen, Ryosuke Ogaki, Vladimir Bochenkov, Lene N. Nejsum, and Duncan S. Sutherland. Complex protein nanopatterns over large areas via colloidal lithography. *Acta Biomaterialia*, 9(4):6158–6168, 2013. ISSN 17427061. doi: 10.1016/j.actbio.2013.01.011. URL <http://dx.doi.org/10.1016/j.actbio.2013.01.011>.
- [94] Theobald Lohmüller, Daniel Aydin, Marco Schwieder, Christoph Morhard, Ilia Louban, Claudia Pacholski, and Joachim P. Spatz. Nanopatterning by block copolymer micelle nanolithography and bioinspired applications. *Biointerphases*, 6(1):MR1–MR12, 2011. ISSN 1934-8630. doi: 10.1116/1.3536839. URL <http://avs.scitation.org/doi/10.1116/1.3536839>.
- [95] Karsten Thelen, Tobias Wolfram, Bettina Maier, Steffen Jähring, Ahmed Tinazli, Jacob Piehler, Joachim P. Spatz, and G. Elisabeth Pollerberg. Cell adhesion molecule dm-grasp presented as nanopatterns to neurons regulates attachment and neurite growth. *Soft Matter*, 3:1486–1491, 2007. doi: 10.1039/B707250C. URL <http://dx.doi.org/10.1039/B707250C>.
- [96] Verónica Hortigüela, Enara Larrañaga, Francesco Cutrale, Anna Seriola, María García-Díaz, Anna Lagunas, Jordi Andilla, Pablo Loza-Alvarez, Josep Samitier, Samuel Ojosnegros, and Elena Martínez. Nanopatterns of surface-bound ephrinb1 produce multivalent ligand–receptor interactions that tune ephb2 receptor clustering. *Nano Letters*, 18(1):629–637, 2018. doi: 10.1021/acs.nanolett.7b04904. PMID: 29243484.
- [97] Eduardo Antonio Della Pia, Jeppe V. Holm, Noemie Lloret, Christel Le Bon, Jean Luc Popot, Manuela Zoonens, Jesper Nygård, and Karen Laurence Martinez. A step closer to membrane protein multiplexed nanoarrays using biotin-doped polypyrrole. *ACS Nano*, 8(2):1844–1853, 2014. ISSN 19360851. doi: 10.1021/nl406252h.
- [98] H Schmid and B Michel. Siloxane polymers for high resolutions, high accuracy soft lithography. *Macromolecules*, 33:3042, 2000.
- [99] Luisa Filipponi, Peter Livingston, Ondřej Kašpar, Viola Tokárová, and Dan V. Nicolau. Protein patterning by microcontact printing using pyramidal PDMS stamps. *Biomedical Microdevices*, 18(1):1–7, 2016. ISSN 15728781. doi: 10.1007/s10544-016-0036-4.
- [100] Hong Wei Li, Beinn V.O. Muir, Guillaume Fichet, and Wilhelm T.S. Huck. Nanocontact printing: A route to sub-50-nm-scale chemical and biological patterning. *Langmuir*, 19(6):1963–1965, 2003. ISSN 07437463. doi: 10.1021/la0269098.

Bibliography

- [101] Daniel Schwaab, Peter Zentis, Silke Winter, Simone Meffert, Andreas Offenhäusser, and Dirk Mayer. Generation of protein nanogradients by microcontact printing. *Japanese Journal of Applied Physics*, 52(5 PART 2), 2013. ISSN 00214922. doi: 10.7567/JJAP.52.05DA19.
- [102] Xuechuan Shan, Y. C. Liu, and Y. C. Lam. Studies of polymer deformation and recovery in micro hot embossing. *Microsystem Technologies*, 14(7):1055–1060, 2008. ISSN 09467076. doi: 10.1007/s00542-007-0486-y.
- [103] J. P. Renault, A. Bernard, A. Bietsch, B. Michel, H. R. Bosshard, E. Delamarche, M. Kreiter, B. Hecht, and U. P. Wild. Fabricating arrays of single protein molecules on glass using microcontact printing. *The Journal of Physical Chemistry B*, 107(3):703–711, 2003. ISSN 1520-6106. doi: 10.1021/jp0263424.
- [104] Arrayit Corporation. Last visited: 20.04.2018. URL http://www.arrayit.com/Products/Microarray_Slides/Epoxy_Slides/epoxy_slides.html.
- [105] Anteo Technologies. Our technology; last visited: 20.04.2016. URL <https://www.anteotech.com/our-technology/>.
- [106] Huey Wen Ooi, Shaun J. Cooper, Chang-Yi Huang, Dean Jennins, Emma Chung, N. Joe Maeji, and Andrew K. Whittaker. Coordination complexes as molecular glue for immobilization of antibodies on cyclic olefin copolymer surfaces. *Analytical biochemistry*, 456:6–13, 2014. ISSN 1096-0309. doi: 10.1016/j.ab.2014.03.023.
- [107] C. B. Arenas, E. Sánchez-Tirado, I. Ojeda, C. A. Gómez-Suárez, A. González-Cortés, R. Villalonga, P. Yáñez-Sedeño, and J. M. Pingarrón. An electrochemical immunosensor for adiponectin using reduced graphene oxide–carboxymethylcellulose hybrid as electrode scaffold. *Sensors and Actuators B: Chemical*, 223:89–94, 2016. ISSN 09254005. doi: 10.1016/j.snb.2015.09.055.
- [108] E. Sánchez-Tirado, C. Salvo, A. González-Cortés, P. Yáñez-Sedeño, F. Langa, and J. M. Pingarrón. Electrochemical immunosensor for simultaneous determination of interleukin-1 beta and tumor necrosis factor alpha in serum and saliva using dual screen printed electrodes modified with functionalized double-walled carbon nanotubes. *Analytica chimica acta*, 959:66–73, 2017. ISSN 1873-4324. doi: 10.1016/j.aca.2016.12.034.
- [109] E. Sánchez-Tirado, G. Martínez-García, A. González-Cortés, P. Yáñez-Sedeño, and J. M. Pingarrón. Electrochemical immunosensor for sensitive determination of transforming growth factor (tgf) - beta1 in urine. *Biosensors & bioelectronics*, 88:9–14, 2017. ISSN 0956-5663. doi: 10.1016/j.bios.2016.05.093.
- [110] G. K. Binnig. Atomic force microscope and method for imaging surfaces with atomic resolution, 1988. URL <http://www.google.ch/patents/US4724318>.

- [111] Jiapu Zhang. Canonical dual theory applied to a Lennard-Jones potential minimization problem. 2011. URL <https://www.semanticscholar.org/paper/Canonical-dual-theory-applied-to-a-Lennard-Jones-Zhang/9d4274eb39d91a8d13119c9cccd52e34b6d6c5e0>.
- [112] Rong Zhu, Doris Sinwel, Peter S. Hasenhuettel, Kusumika Saha, Vivek Kumar, Peng Zhang, Christian Rankl, Marion Holy, Sonja Sucic, Oliver Kudlacek, Andreas Karner, Walter Sandtner, Thomas Stockner, Hermann J. Gruber, Michael Freissmuth, Amy Hauck Newman, Harald H. Sitte, and Peter Hinterdorfer. Nanopharmacological force sensing to reveal allosteric coupling in transporter binding sites. *Angewandte Chemie (International ed. in English)*, 55(5):1719–1722, 2016. ISSN 1433-7851. doi: 10.1002/anie.201508755.
- [113] Johannes Preiner, Andreas Horner, Andreas Karner, Nicole Ollinger, Christine Siligan, Peter Pohl, and Peter Hinterdorfer. High-speed afm images of thermal motion provide stiffness map of interfacial membrane protein moieties. *Nano letters*, 15(1):759–763, 2015. ISSN 1530-6984. doi: 10.1021/nl504478f.
- [114] Toshio Ando, Takayuki Uchihashi, and Noriyuki Kodera. High-speed afm and applications to biomolecular systems. *Annual review of biophysics*, 42:393–414, 2013. ISSN 1936-122X. doi: 10.1146/annurev-biophys-083012-130324.
- [115] Yuri Roiter and Sergiy Minko. Afm single molecule experiments at the solid-liquid interface: in situ conformation of adsorbed flexible polyelectrolyte chains. *Journal of the American Chemical Society*, 127(45):15688–15689, 2005. ISSN 0002-7863. doi: 10.1021/ja0558239.
- [116] Nicholas A. Geisse. Afm and combined optical techniques. *Materials Today*, 12(7-8):40–45, 2009. ISSN 13697021. doi: 10.1016/S1369-7021(09)70201-9.
- [117] V. J. Morris, A. R. Kirby, and A. P. Gunning. *Atomic force microscopy for biologists*. Imperial College Press, London, 2. ed. edition, 2010. ISBN 184816467X.
- [118] David P. Allison, Ninell P. Mortensen, Claretta J. Sullivan, and Mitchel J. Doktycz. Atomic force microscopy of biological samples. *Wiley interdisciplinary reviews. Nanomedicine and nanobiotechnology*, 2(6):618–634, 2010. doi: 10.1002/wnan.104.
- [119] Bruker Nano Inc. Last visited: 22.02.2018. URL <https://www.brukerafmprobes.com/p-3864-otespa-r3.aspx>.
- [120] H.C. Ishikawa-Ankerhold, R. Ankerhold, and G.P.C. Drummen. Advanced fluorescence microscopy techniques—frap, flip, flap, fret and flim. *Molecules* 2012, 17: 4047–4132, 2012.
- [121] Angular resolution; last visited: 24.04.2018. URL https://en.wikipedia.org/wiki/Angular_resolution.

Bibliography

- [122] H. H. Jaffe and Albert L. Miller. The fates of electronic excitation energy. *Journal of Chemical Education*, 43(9):469, 1966. ISSN 0021-9584. doi: 10.1021/ed043p469.
- [123] Total internal reflection; last visited: 24.04.2018. URL https://en.wikipedia.org/wiki/Total_internal_reflection.
- [124] Rayleigh. Investigations in optics, with special reference to the spectroscope. *The London, Edinburgh, and Dublin Philosophical Magazine and Journal of Science*, 8 (49):261–274, 2009. ISSN 1941-5982. doi: 10.1080/14786447908639684.
- [125] Max Born and Emil Wolf. *Principles of Optics*. 1999. ISBN 0-521-64222-1.
- [126] Mats G. L. Gustafsson, Eric Betzig, Harald F. Hess, Hari Shroff, George H. Patterson, Jennifer Lippincott-Schwartz, Michael W. Davidson. Education in microscopy and digital imaging. URL <http://zeiss-campus.magnet.fsu.edu/articles/superresolution/introduction.html>.
- [127] Sebastian van de Linde, Anna Löschberger, Teresa Klein, Meike Heidbreder, Steve Wolter, Mike Heilemann, and Markus Sauer. Direct stochastic optical reconstruction microscopy with standard fluorescent probes. *Nature protocols*, 6(7):991–1009, 2011. ISSN 1750-2799. doi: 10.1038/nprot.2011.336.
- [128] Michael J. Rust, Mark Bates, and Xiaowei Zhuang. Sub-diffraction-limit imaging by stochastic optical reconstruction microscopy (storm). *Nature methods*, 3(10):793–795, 2006. ISSN 1548-7091. doi: 10.1038/nmeth929.
- [129] Stefan W. Hell and Jan Wichmann. Breaking the diffraction resolution limit by stimulated emission: Stimulated-emission-depletion fluorescence microscopy. *Optics Letters*, 19(11):780, 1994. ISSN 0146-9592. doi: 10.1364/OL.19.000780.
- [130] M. J. Graham and M. Cohen. On the mechanism of low-temperature oxidation (23–450c) of polycrystalline nickel. *Journal of The Electrochemical Society*, 119 (7):879, 1972. ISSN 00134651. doi: 10.1149/1.2404360.
- [131] Robert Peter, Iva Šarić, and Mladen Petravić. Enhanced oxidation of nickel at room temperature by low-energy oxygen implantation. *Croatica Chemica Acta*, 90 (2), 2017. ISSN 00111643. doi: 10.5562/cca3149.
- [132] *MED-6019: Optically clear, high durometer low consistency silicone elastomer*. NuSil Technology LLC, 05 2014. Rev. A.
- [133] A. N. Gent. On the relation between indentation hardness and young’s modulus. *Rubber Chemistry and Technology*, 31(4):896–906, 1958. ISSN 0035-9475. doi: 10.5254/1.3542351.
- [134] Donald MacNearney, Bernard Mak, Grant Ongo, Timothy E. Kennedy, and David Juncker. Nanocontact Printing of Proteins on Physiologically Soft Substrates to Study Cell Haptotaxis. *Langmuir*, 32(50):13525–13533, 2016. ISSN 15205827. doi: 10.1021/acs.langmuir.6b03246.

- [135] Sébastien G. Ricoult, Amir Sanati Nezhad, Michaela Knapp-Mohammady, Timothy E. Kennedy, and David Juncker. Humidified Microcontact Printing of Proteins: Universal Patterning of Proteins on Both Low and High Energy Surfaces. *Langmuir*, 30(40):12002–12010, 2014. ISSN 15205827. doi: 10.1021/la502742r.
- [136] Eva Sevcsik, Mario Brameshuber, Martin Fölser, Julian Weghuber, Alf Honigmann, and Gerhard J. Schütz. GPI-anchored proteins do not reside in ordered domains in the live cell plasma membrane. *Nature Communications*, 6:1–10, 2015. ISSN 20411723. doi: 10.1038/ncomms7969.
- [137] Peter Lanzerstorfer, Daniela Borgmann, Gerhard Schütz, Stephan M. Winkler, Otmar Höglinger, and Julian Weghuber. Quantification and Kinetic Analysis of Grb2-EGFR Interaction on Micro-Patterned Surfaces for the Characterization of EGFR-Modulating Substances. *PLoS ONE*, 9(3):e92151, mar 2014. ISSN 1932-6203. doi: 10.1371/journal.pone.0092151. URL <https://dx.plos.org/10.1371/journal.pone.0092151>.
- [138] Victor E. Koteliansky, Marina A. Glukhova, Marina V. Benjamin, Vladimir N. Smirnov, Valdimir V. Filimonov, Olga M. Zalite, and Sergei Yu. Venyaminov. A study of the structure of fibronectin. *European Journal of Biochemistry*, 119(3):619–624, 1981. ISSN 1432-1033. doi: 10.1111/j.1432-1033.1981.tb05652.x. URL <http://onlinelibrary.wiley.com/doi/10.1111/j.1432-1033.1981.tb05652.x/pdf>.
- [139] Kay C. Dee, David A. Puleo, and Rena Bizios. *An introduction to tissue-biomaterial interactions*. John Wiley & Sons, Hoboken, 2003. ISBN 978-0-471-25394-5.
- [140] Bryce T. Bajar, Emily S. Wang, Amy J. Lam, Bongjae B. Kim, Conor L. Jacobs, Elizabeth S. Howe, Michael W. Davidson, Michael Z. Lin, and Jun Chu. Improving brightness and photostability of green and red fluorescent proteins for live cell imaging and fret reporting. *Scientific reports*, 6:20889, 2016. ISSN 2045-2322. doi: 10.1038/srep20889.
- [141] Li Wang, Francis Clube, Christian Dais, Harun H. Solak, and Jens Gobrecht. Sub-wavelength printing in the deep ultra-violet region using displacement talbot lithography. *Microelectronic Engineering*, 161:104–108, 2016. ISSN 01679317. doi: 10.1016/j.mee.2016.04.017.
- [142] Iris Bergmair, Michael Mühlberger, Elisabeth Lausecker, Kurt Hingerl, and Rainer Schöftner. Diffusion of thiols during microcontact printing with rigid stamps. *Microelectronic Engineering*, 87(5):848 – 850, 2010. ISSN 0167-9317. doi: <https://doi.org/10.1016/j.mee.2009.12.058>. URL <http://www.sciencedirect.com/science/article/pii/S0167931709009010>. The 35th International Conference on Micro- and Nano-Engineering (MNE).

- [143] Julia Kastner, Olivier Lorret, Andreas Rank, Clemens Schwarzingler, Bernd Dittert, and Michael Mühlberger. Nanocontact printing stamp material via bifunctionalization of polyhedral oligomeric silsesquioxanes. *European Polymer Journal*, 65:221–231, 2015. ISSN 00143057. doi: 10.1016/j.eurpolymj.2014.11.015.
- [144] Harold E. Gaubert and Wolfgang Frey. Highly parallel fabrication of nanopatterned surfaces with nanoscale orthogonal biofunctionalization imprint lithography. *Nanotechnology*, 18(13):135101, 2007. ISSN 0957-4484. doi: 10.1088/0957-4484/18/13/135101.
- [145] Mark Moxey, Alexander Johnson, Osama El-Zubir, Michael Cartron, Saman Safari Dinachali, C. Neil Hunter, Mohammad S. M. Saifullah, Karen S. L. Chong, and Graham J. Leggett. Fabrication of self-cleaning, reusable titania templates for nanometer and micrometer scale protein patterning. *ACS nano*, 9(6):6262–6270, 2015. ISSN 1936-0851. doi: 10.1021/acs.nano.5b01636.
- [146] Hella-Christin Scheer, A. Mayer, K. Dhima, S. Wang, and C. Steinberg. Challenges with high aspect ratio nanoimprint. *Microsystem Technologies*, 20(10-11):1891–1898, 2014. ISSN 0946-7076. doi: 10.1007/s00542-013-1968-8.
- [147] Hella-C. Scheer, M. Papenheim, K. Dhima, S. Wang, and C. Steinberg. Aspects of cavity filling with nano imprint. *Microsystem Technologies*, 21(8):1595–1605, 2015. ISSN 0946-7076. doi: 10.1007/s00542-014-2376-4.
- [148] C. Auner, U. Palfinger, H. Gold, J. Kraxner, A. Haase, T. Haber, M. Sezen, W. Grogger, G. Jakopic, J. R. Krenn, G. Leising, and B. Stadlober. Residue-free room temperature uv-nanoimprinting of submicron organic thin film transistors. *Organic Electronics*, 10(8):1466–1472, 2009. ISSN 15661199. doi: 10.1016/j.orgel.2009.08.010.
- [149] Mark Gorman, Ya Hua Chim, Andrew Hart, Mathis O. Riehle, and Andrew J. Urquhart. Poly(n-acryloylmorpholine): a simple hydrogel system for temporal and spatial control over cell adhesion. *Journal of biomedical materials research. Part A*, 102(6):1809–1815, 2014. ISSN 1549-3296. doi: 10.1002/jbm.a.34853.
- [150] Guisheng Zhuang and Jörg P. Kutter. Anti-stiction coating of pdms moulds for rapid microchannel fabrication by double replica moulding. *Journal of Micromechanics and Microengineering*, 21(10):105020, 2011. ISSN 0960-1317. doi: 10.1088/0960-1317/21/10/105020. URL <http://iopscience.iop.org/article/10.1088/0960-1317/21/10/105020/pdf>.
- [151] Franck D ’ Agosto, Marie-Therese Charreyre, Laurent Veron, Marie-France Llauro, and Christian Pichot. Kinetic study of free-radical solution copolymerization of n-acryloylmorpholine with an activated ester-type monomer, n-acryloxysuccinimide. 202:1689–1699, 2001.

- [152] James A. Dougherty, Louise I. Lynch, Leen Mahamoud. Acryloyl morpholine for uv curing. *RadTech Report*, (May/June 2007), 2007. URL <http://www.radtech.org/magazinearchives/new-index.htm>.
- [153] T. C. Merkel, V. I. Bondar, K. Nagai, B. D. Freeman, and I. Pinnau. Gas sorption, diffusion, and permeation in poly(dimethylsiloxane). *Journal of Polymer Science Part B: Polymer Physics*, 38(3):415–434, 2000. ISSN 0887-6266.
- [154] Jessamine Ng Lee, Cheolmin Park, and George M. Whitesides. Solvent compatibility of poly(dimethylsiloxane)-based microfluidic devices. *Analytical chemistry*, 75(23):6544–6554, 2003. ISSN 0003-2700. doi: 10.1021/ac0346712.
- [155] B. Bilenberg and Colin Welch. High quality patterns produced by nanoimprint lithography and inductive coupled plasma etching. 2018.
- [156] Christoph Auner, Ursula Palfinger, Herbert Gold, Johanna Kraxner, Anja Haase, Thomas Haber, Meltem Sezen, Werner Grogger, Georg Jakopic, Joachim R. Krenn, G. Leising, and Barbara Stadlober. High-performing submicron organic thin-film transistors fabricated by residue-free embossing. *Organic Electronics*, 11(4):552–557, 2010. ISSN 15661199. doi: 10.1016/j.orgel.2009.12.012.

Contributions and Publications

Marco Lindner (ML), Iris Prinz, Gerhard Schütz and Eva Sevcsik conceived and designed the experiments. ML and Adrian Prinz (AP) performed the PTM-mastering; ML and Aliz Tresztenyak performed the nanocontact printing experiments with silicones and ML analyzed the data. Gergö Fülöp, Martin Fölser and ML performed the TIRFM and RICM experiments. Gergö Fülöp and Eva Sevcsik performed the STORM experiments. All microscopy data was analyzed by ML. Wiebke Jahr and Georg Danzl designed, performed and analyzed the STED microscopy experiments. POSS was synthesized by Julia Kastner, NIL and nCP experiments with POSS were performed and analyzed by ML. NIL with uv-curable NAM was performed and analyzed by Violeta Tacheva and ML. ML wrote the thesis, while Eva Sevcsik revised the manuscript.

This thesis gave rise to the following peer-reviewed publication:

Marco Lindner, Aliz Tresztenyak, Gergö Fülöp, Wiebke Jahr, Adrian Prinz, Iris Prinz, Johann G. Danzl, Gerhard Schütz, Eva Sevcsik. (2019). A Fast and Simple Contact Printing Approach to Generate 2D Protein Nanopatterns. *Frontiers in Chemistry*. 6. 10.3389/fchem.2018.00655.

Acknowledgment

First and foremost, I would like to thank my two children who have always been patient with me when I was working on the dissertation in the evening or at the weekend. And my thanks go especially to my wife, who always supported and encouraged me again and again.

I would also like to thank my parents, who also supported me during my studies and enabled me to make Biophysics a part of my life.

Furthermore, I would like to thank Gerhard J. Schütz, Eva Sevcsik and Iris Prinz, the three initiators and supervisors of the project.

Special thanks also go to Aliz Tresztenyak, Violeta Tacheva and Adrian Prinz of Stratec for their support and ideas. To Gergö Fülöp, Andreas Arnold, Martin Fölser and the Schütz laboratory in general for their scientific input and their great support. And to Johann Georg Danzl and Wiebke Jahr for the opportunity to apply STED microscopy and to see the nanopatterns to which I devoted years of my life.

My thanks go also to Günter Lepperdinger, the head of the Spoc laboratories, where most of the work was done, to Martin Fischlechner, whose constructive criticism I could rely on, and to Marc Verschuuren for his advices on using X-PDMS.

Last but not least, my thanks go to Georg Bauer and Werner Balika, who enabled me to do basic research on the infrastructure of Stratec.



Die approbierte gedruckte Originalversion dieser Dissertation ist an der TU Wien Bibliothek verfügbar.
The approved original version of this doctoral thesis is available in print at TU Wien Bibliothek.